

# Modeling of Fine and Dynamic Structuring of Coronal Loops

Author: Massimiliano Guarrasi  
Supervisor: Prof. Fabio Reale

January 5, 2012



# Contents

<b>1</b>	<b>Introduction</b>	<b>1</b>
1.1	The Solar Corona . . . . .	2
1.2	Coronal Loops . . . . .	2
1.2.1	Morphology and evolution . . . . .	2
1.2.2	Heating Mechanism in Coronal Loops . . . . .	8
1.3	Modelling of Coronal Loops . . . . .	10
1.3.1	Basic . . . . .	11
1.3.2	Fine Structuring and multi/stranded models . . . . .	12
1.3.3	Interaction with Magnetic Field: MHD Modeling . . . . .	13
1.3.4	Outline of the thesis . . . . .	16
<b>2</b>	<b>Multistranded Loops</b>	<b>17</b>
2.1	The Model . . . . .	20
2.1.1	The Equations . . . . .	20
2.1.2	Strand initial conditions . . . . .	21
2.1.3	The strand heating . . . . .	21
2.1.4	The Code . . . . .	22
2.1.5	The Loop System . . . . .	22
2.1.6	The Loop emission . . . . .	23
2.2	Results . . . . .	25
2.2.1	The Strand Evolution . . . . .	25
2.2.2	The Loop Evolution . . . . .	25
2.2.3	Hinode/EIS Emission . . . . .	25
2.2.4	SDO/AIA emission . . . . .	34
2.3	Experimental Evidence . . . . .	41
2.3.1	Comparison with EIS data . . . . .	41
2.3.2	Comparison with SDO data . . . . .	41
2.4	Discussion . . . . .	51
<b>3</b>	<b>MHD Modeling</b>	<b>55</b>

3.1	The Model . . . . .	57
3.1.1	The Equations . . . . .	57
3.1.2	The Code . . . . .	58
3.2	Heating in Variable Section-Coronal Loops . . . . .	60
3.2.1	Initial and Boundary Conditions . . . . .	60
3.2.2	The simulation . . . . .	63
3.2.3	Results . . . . .	67
3.3	Discussion . . . . .	68
<b>4</b>	<b>Conclusions and Future Developments</b>	<b>71</b>
	<b>Bibliography . . . . .</b>	<b>76</b>



# List of Figures

1.1	Plane-parallel model of solar atmospheric temperature (solid line), and density (dotted line) vs height (Golub & Pasachoff, 1997). . . . .	3
1.2	Optical image of a solar eclipse over the Marshall Islands in July 2009. Photo: Miloslav Druckmuller. . . . .	4
1.3	Composite EUV image of the solar corona seen with SDO/AIA 211 Å, 191 Å, and 171 Å filters on November 9, 2011. Credit: NASA/SDO. . . . .	5
1.4	Soft-X image of the solar corona seen with HINODE/XRT Al/Poly filters on October 17, 2007. Credit: ISAS-JAXA/HINODE. . . . .	6
1.5	An active region observed from SDO/AIA, 171 Å filter, 9 July 2010. Credit: NASA/SDO. . . . .	7
1.6	An active region observed by TRACE (9 November 2000, 2 UT). We can distinguish between strands that make the loops. Credit: NASA/TRACE. . . . .	9
2.1	From Tripathi et al. (2009). Top panel: An active region loops seen at different temperatures. Bottom panels: Total intensity variation in the region marked by the two white lines in the corresponding top panels. . . . .	19
2.2	Profile of emission per unit of emission measure vs $\log T[K]$ for the various spectral lines. We make a distinction between lines for comparison with Tripathi et al. (2009) ( <i>solid lines</i> ), lines in AIA filter bands on board of SDO mission ( <i>dashed lines</i> ), and hot X ray lines ( <i>dotted lines</i> ). . . . .	24
2.3	Flowchart showing how an loop bundle image is obtained from the emission of each individual loop in a given spectral line. We first compute the spatial distribution of the emission along each strand, we then put the emission in the form of an image made of a pixel strip, we put all pixel strips side by side; we then reconstruct the aspect of the whole loop system, then we group the strands into loops. Finally we bend the image to obtain a loop-like shape. . . . .	26
2.4	Temperature (a), and density (b) along half of a single strand at times $t = 0, 20, 100, 400, 800, 2000$ s (thinner and thinner lines with progressing time). The heat pulse starts at time $t = 0$ and lasts 60 s. . . . .	27
2.5	Evolution of the loop average temperature from off-state to steady-state. . . . .	28

2.6	Distribution of emission measure vs Temperature at $t = 2000$ s. We show the distribution of the coronal part only, i.e. the upper 90% of the loops. . . . .	29
2.7	Loop bundle emission in different (labeled) spectral lines. In the images (left column) we show the upper 90% of the loop. The grey scale is logarithmic, and covers a factor 10 of intensity; black corresponds to the maximum of emission and white to the minimum. The plots in the right column are the emission profiles along the lines marked in the images of the left column, in the same logarithmic scale. . . . .	30
2.8	Scatter plot of the values of density and temperature, obtained from averaging on bins of 32 grid points in the whole model strand evolution (upper 90% part of the loops). The dashed line is the locus of density and temperature at the apex of hydrostatic loops, with half-length $L = 3.0 \times 10^9$ cm, according to the scaling laws of Rosner et al. (1978). . . . .	32
2.9	Emissivity per unit emission measure for 94 Å, 335 Å and 171 Å SDO/AIA channels vs $T$ . . . . .	35
2.10	Emission of a straightened multi-stranded loop obtained from hydrodynamic modeling of a strand pulse-heated to 10 MK in the 94Å (a), and 335Å (b) SDO channels. Each strip is the average of a bundle of 60 strands. To emphasize the effect we are addressing, we normalize the emission in each pixel strip <i>across</i> the loop. In this color scale, white is the maximum of emission, and black the minimum (linear scale) spanning between 0.6 and 1.4 (average 1). Images (a) and (b) show the coronal part of the loop (upper 75% of the loop length). The loop is symmetric with respect the loop apex. (c) Cuts across the images (green lines). Red and green lines are related to the SDO 94Å and the 335Å channel, respectively. . . . .	36
2.11	Scatter plot of the values of emission vs temperature obtained from hydrodynamic modeling of a strand pulse-heated to 10 MK. The values are averages over bins of 24 grid points at any time of the model strand evolution (upper 75% of the loops). Red and green points are related to the SDO 94 Å and the 335 Å channel, respectively. Bright 335 Å pixels contain mostly $\sim 3$ MK plasma. The bright 94 Å pixels contain hotter plasma ( $\sim 6 - 8$ MK). . . . .	37
2.12	Distribution histogram of the values shown in Fig.2.11. Red lines refer to the 94 Å channel and green points to the 335 Å channel. Bright pixels are more numerous in the 335 Å channel. . . . .	38
2.13	As Fig.2.11 for a strand model with less intense heat pulses which lead to a strand maximum temperature of about 4 MK. . . . .	39
2.14	Light curves ( <i>solid lines</i> 94 Å, <i>dashed lines</i> 335 Å) in five sample pixels obtained from the hydrodynamic simulation of multi-stranded pulse-heated loop. The intensities are normalized to the average emission in the pixel. The model light curves can be compared to the observed ones (Fig. 2.16 and 2.20). . . . .	42

2.15	Active region AR 11117 observed in 3 different filters (94 Å, 335 Å, 171 Å) of the SDO/AIA on 27 October 2010 around 01 UT. The filters are most sensitive to plasma emitting at the labeled temperatures. The subregion shown in Fig.1 in the main text is marked (box). Large-scale loops (LL) are marked outside of the boxes in the 335Å image. In the 171 Å we indicate moss regions and outbound loops (OL). . . . .	44
2.16	Normalized lightcurves derived in the three channels over a period of 1 hr (from 02 : 00 : 00 to 03 : 00 : 00), and integrating the signal in the active region core (in a region of 100 pix X 110 pix). . . . .	45
2.17	Inner part of the active region AR11117 observed in 3 different channels (335Å, 94Å, 171Å) of the SDO/AIA on 27 October 2010 around 02 UT. The color scales as the square root of the pixel counts. The ranges are 59–1567, 55–3157, 155–4681 DN for the three channels, respectively. The channels are most sensitive to plasma emitting at the labeled temperatures. The bottom panel shows the image obtained by subtracting the cool component scaled from the 171Å channel to the 94Å image (same color scale as second panel, real range 0–2741 DN). Fig. 2.18 shows brightness profiles along the marked vertical and horizontal lines. . . . .	47
2.18	Brightness profiles in the 94Å before (red) and after (black dotted) subtracting the cool 1 MK component, and in the 335Å (green) channels along the horizontal (a) and vertical (b) lines in Fig. 2.17. The profiles are normalized to a moving average with a 10 pixels boxcar. A typical error bar is also shown. . . . .	48
2.19	Normalized 2-D Fourier Transforms of 335Å and both 94Å images in Fig. 2.17. 94Å transforms are both systematically higher than the 335Å transform in the wavenumber range between the dashed lines. . . . .	50
2.20	Light curves (solid lines 94 Å , dashed lines 335 Å ) in five sample pixels in the region of the bright thin structures in the 94 Å channel (X 60, Y 60 in new Fig. 2.17). The intensities are normalized to the average DN rate. . . . .	52
3.1	The radiative loss $\Lambda(T)$ from E. Landi private communication. . . . .	59
3.2	Flowchart showing how we obtain our computational domain. . . . .	61
3.3	Figure (a): Plot of Temperature in logarithmic scale of our loop model. The Blue domain is the chromospherical part of the domain at the basis of the loop. The black lines are the magnetic field lines. Temperature spans from $2. \times 10^4$ K to $3. \times 10^6$ K. Figure (b): Pixels size on computational domain. Solid line is the pixels size (dy) along the loop direction (y coordinate). Dashed line is the pixels size (dx) across the loop (x coordinate). The resolution spans from $2. \times 10^6$ cm to $4. \times 10^7$ cm. . . . .	62

3.4	Figure (a): Plot of Temperature in logarithmic scale for our initial loop atmosphere. The Blue domain is the chromospherical part of the domain at the basis of the loop. Figure (b): Plot of electron density in logarithmic scale for the same atmosphere. Figure (c): Plot of the module of magnetic field for our initial loop atmosphere. . Figure (d): Plot of plasma $\beta$ factor in logarithmic scale for our initial loop atmosphere. In all figures, the black lines are the magnetic field lines.	64
3.5	Temperature (Fig. (a)), electron density (Figure (b)), and magnetic field (Figure (c)) profile for our initial loop atmosphere. The density and temperature profiles are drawn along the loop, whereas the magnetic field profile is drawn across the loop. . . . .	65
3.6	The same of Fig. 3.4 for the stable final atmosphere, obtained after $10^4$ s of evolution from the initial condition reported in Fig. 3.4 . . . . .	66
3.7	Time profile for the heating function calculated on $x = 0$ . . . . .	67
3.8	Temperature (left column), electron density (central column), and plasma $\beta$ factor (right column) profile for our loop at $t = 50$ s (pannel a, b and c), $t = 200$ s (pannel d, e and f), $t = 400$ s (pannel g, h and i), $t = 800$ s (pannel j, k and l), $t = 2500$ s (pannel m, n and o). . . . .	69
3.9	Evolution of the moss region. In panel (a) and (b) we see the map of temperature in logarithmic scale at $t = 0$ s and $t = 2500$ s. The vertical lines are the field lines that we use to identify the loop. The horizontal lines identify the moss position. Panel (c) is the evolution of the moss size with time. Panel (d) is the position of the moss with time. . . . .	70

# List of Tables

1.1	Typical coronal loop parameter (Reale, 2010). . . . .	8
2.1	Variation of emission in the lines analyzed. . . . .	33
2.2	Fractional RMS amplitude excursions . . . . .	49

# **Chapter 1**

## **Introduction**

## 1.1 The Solar Corona

The solar corona is the outer part of the solar atmosphere. It extends above the transition region for several solar radii into interplanetary space. Its temperature varies from less than 1 MK to more than 10 MK. The particle density varies from less than  $10^8 \text{ cm}^{-3}$  to  $10^{11} \text{ cm}^{-3}$ . In Fig. 1.1 we report a schematic representation of the temperature and density of the solar atmosphere as a function of height above the surface.

The appearance of the solar corona during a total solar eclipse is shown in Fig. 1.2. It is extremely faint relative to the visible disk of the sun, having a maximum brightness ratio of  $10^{-6}$ , so that it is completely invisible to the naked eye in normal condition.

When inspected through spectroscopy the corona reveals unexpected emission lines, which is due to high excitation states of iron (e.g., Golub & Pasachoff 1997).

If observed in Extreme UltraViolet (EUV) and X bands the corona is far from homogeneous, as we can see in Fig. 1.3 and 1.4. It appear as formed mainly by two kinds of structures: one formed of bundles of luminous arches (*active regions* formed by bundles of *coronal loops*), the other characterized by low emission (*coronal holes*). We focus our attention to coronal loops.

## 1.2 Coronal Loops

Coronal loops are the basic building blocks of the solar corona. In Fig. 1.5, we see an active region observed with SDO/AIA, 171 Å filter, 9 July 2010, in which we clearly see the presence of some arch-like structures.

Although coronal loops are often well defined and studied in the EUV band, the bulk of coronal loops is visible in the X-ray band (Fig. 1.4). Furthermore, the peak of the coronal emission measure of active regions is above 2 MK, which is best observed in X-rays (e.g.: Reale et al. 2009a; Peres et al. 2000). Coronal loops are composed by arch-like structure, that follows typical magnetic field topology.

Some typical coronal loop parameters are shown in Tab. 1.1. The length of coronal loops spans over many order of magnitude: from  $1 \times 10^6 \text{ m}$  for *Bright points*, to  $1 \times 10^9 \text{ m}$  for *Giant loops*, through *Active Region loops* (AR loops; length =  $1 - 10 \times 10^7 \text{ m}$ ). Temperature varies from  $10^5 \text{ K}$  (*cool loops*), to  $\sim 3 \times 10^6 \text{ K}$  (AR loops), up to a few  $10^7 \text{ K}$  (*flaring loops*). Density spans from  $10^{14} \text{ m}^{-3}$  to  $10^{17} \text{ m}^{-3}$ .

### 1.2.1 Morphology and evolution

As a good approximation, loops generally have a semicircular shape. Clearly, the loops aspect depends on which direction we see the loop: if we look at the limb of sun, probably we can easily see semicircular loops (this is the case in Fig. 1.5), as well as if we look at the center of the solar disk the loops are very inclined and don't appear semicircular.

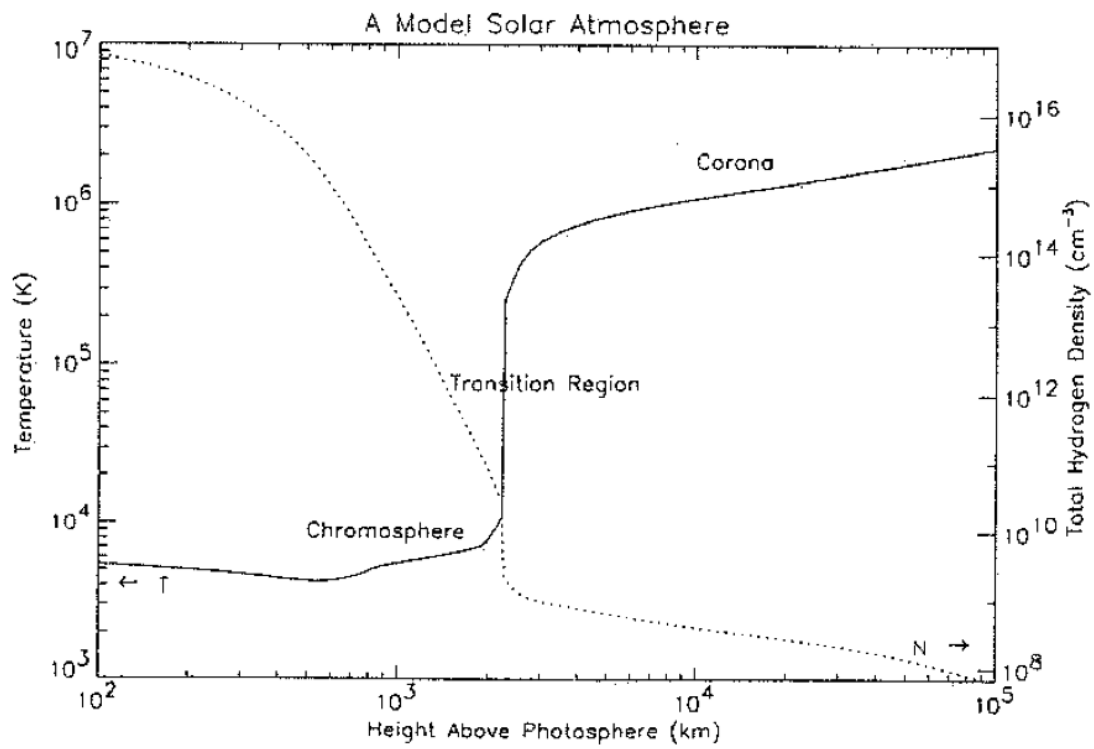


Figure 1.1 Plane-parallel model of solar atmospheric temperature (solid line), and density (dotted line) vs height (Golub & Pasachoff, 1997).



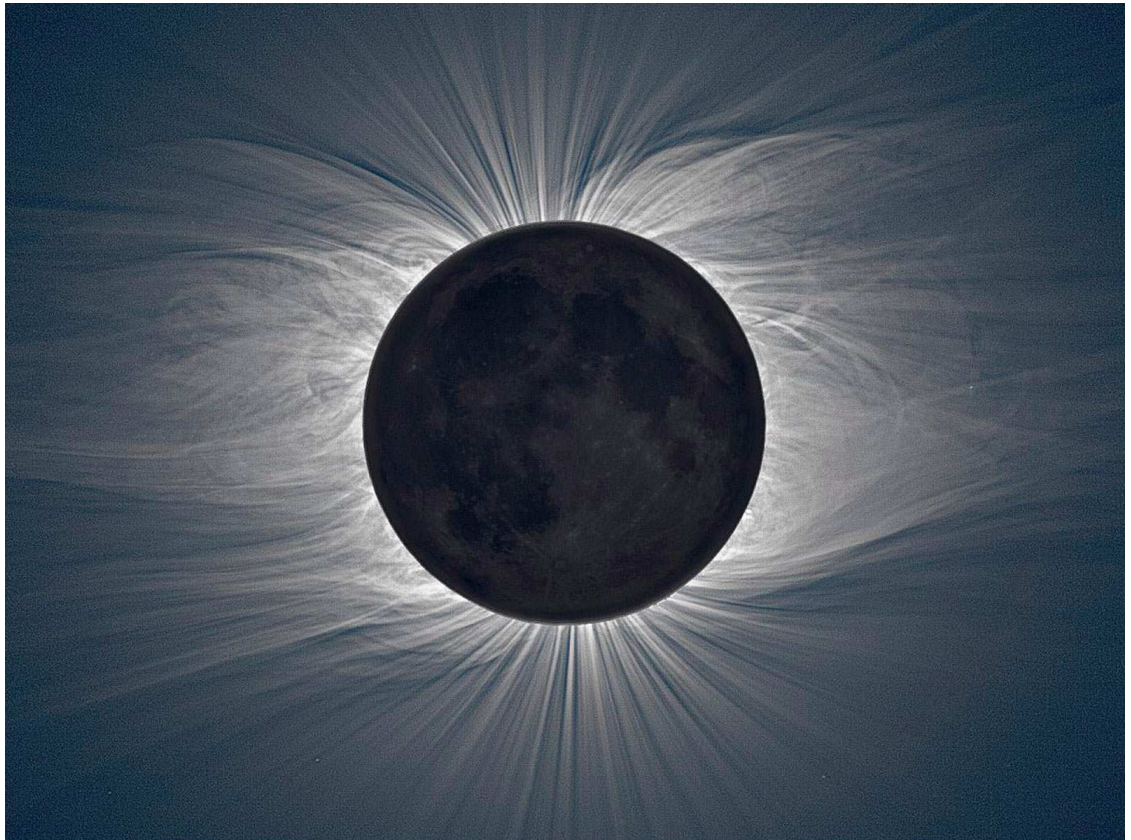


Figure 1.2 Optical image of a solar eclipse over the Marshall Islands in July 2009. Photo: Miloslav Druckmuller.

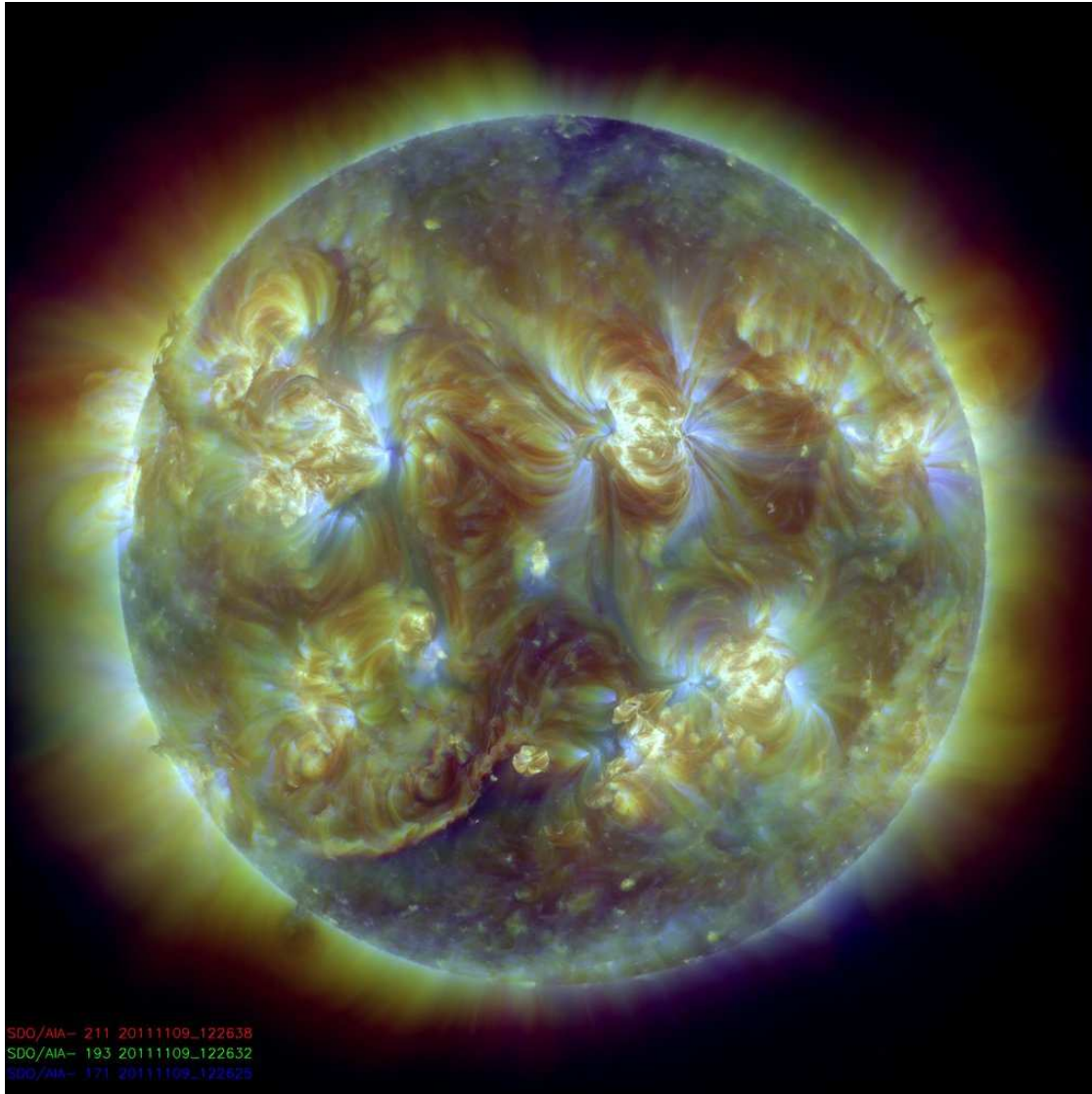


Figure 1.3 Composite EUV image of the solar corona seen with SDO/AIA 211 Å, 191 Å, and 171 Å filters on November 9, 2011. Credit: NASA/SDO.

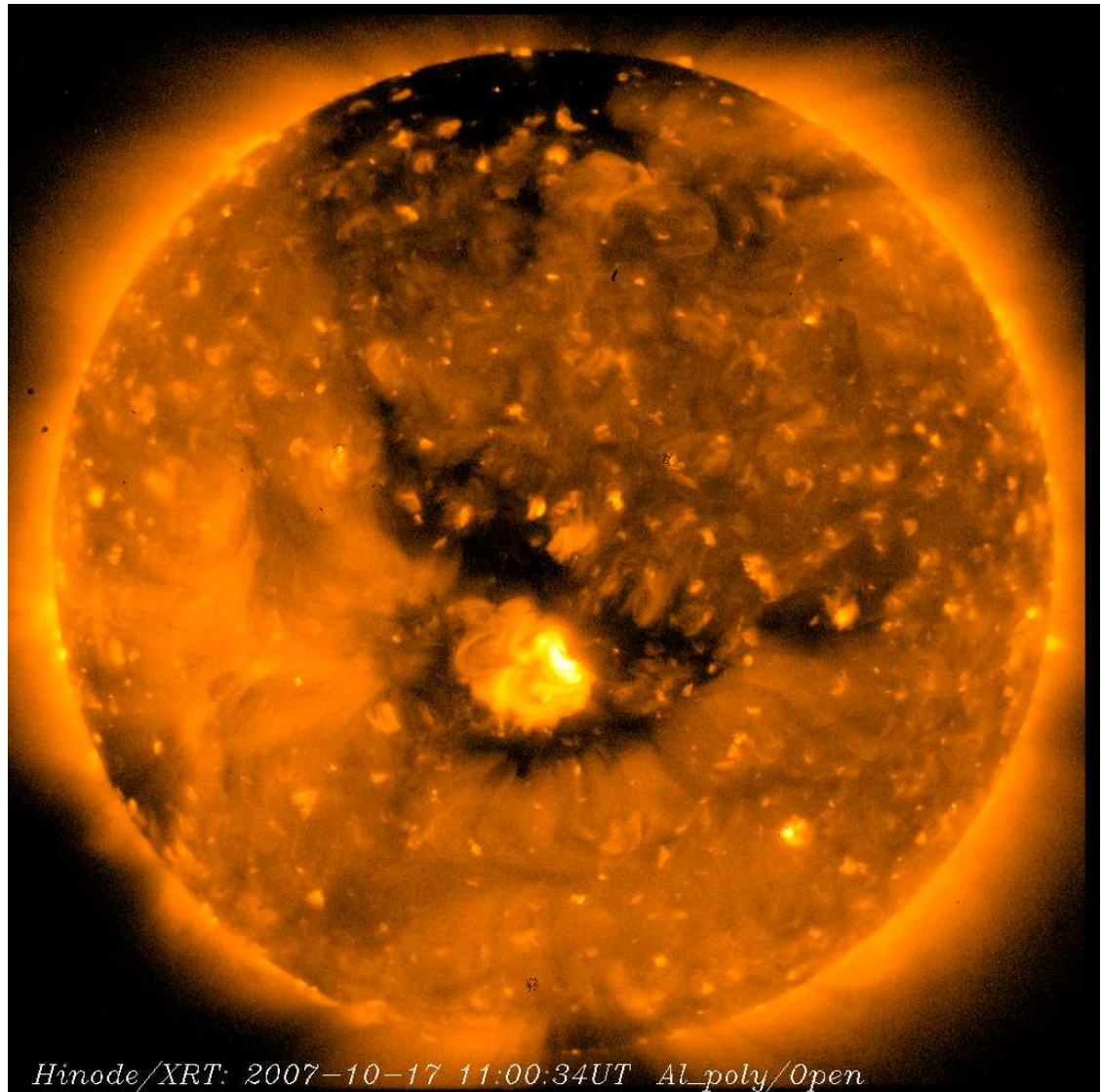


Figure 1.4 Soft-X image of the solar corona seen with HINODE/XRT Al/Poly filters on October 17, 2007. Credit: ISAS-JAXA/HINODE.



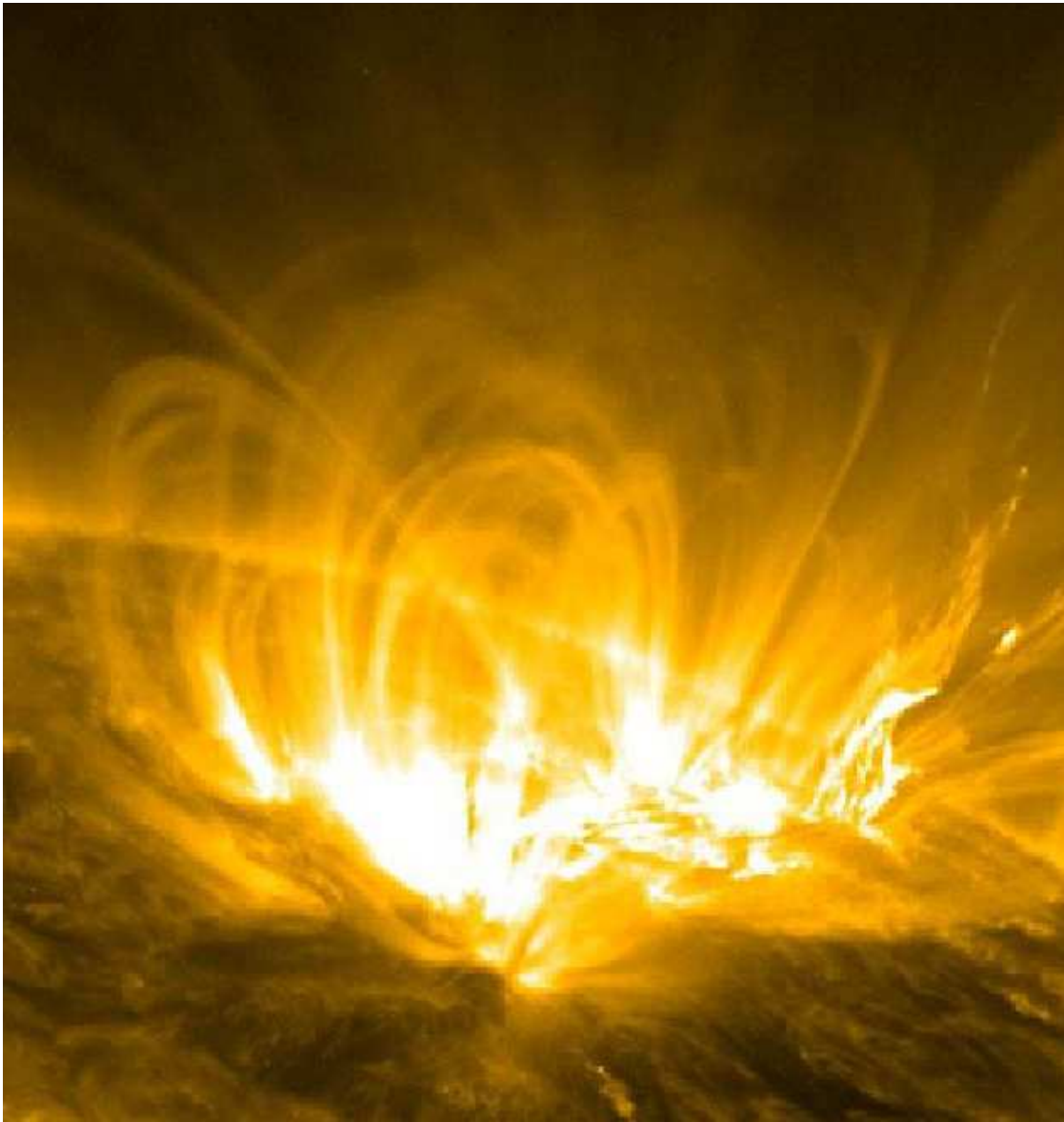


Figure 1.5 An active region observed from SDO/AIA, 171 Å filter, 9 July 2010. Credit: NASA/SDO.

Table 1.1 Typical coronal loop parameter (Reale, 2010).

	Bright points	Active region	Giant arches	Flaring loops
Length ( $10^9$ cm)	0.1 – 1	1 – 10	10 – 100	1 – 10
Temperature ( $10^6$ K)	2	3	1 – 2	> 10
Density ( $10^9$ cm <sup>-3</sup> )	5	1 – 10	0.1 – 1	> 50
Pressure (dyne cm <sup>-2</sup> )	3	1 – 10	0.1	> 100

The structure of coronal loops is due to the presence of a strong magnetic field, which confines the plasma. When the plasma inside the flux tubes is heated more than the surroundings, its density increases. Since the plasma is optically thin, the intensity of its radiation is proportional to the square of the density, and the tube becomes much brighter than the surrounding ones and looks like a bright closed arch.

Since end of 80s, thanks to the observation made by NIXT (Gomez et al., 1993b; Di Matteo et al., 1999), we have some limited evidence for fine structuring on coronal loops. With the high spatial resolution achieved by TRAnsition region and Coronal Explorer (TRACE, Handy et al. 1999), this evidence was supported also by visual inspection. For example, in Fig. 1.6 we see an active region observed by TRACE in November, 9, 2000, 2 UT. This image clearly shows that coronal loops are substructured. Nevertheless, the task to investigate this substructuring is not easy because the thickness of the elementary components may be as small as a few km, according to some nanoflare models (Parker, 1988; Vekstein, 2009), below the resolution limit of the most powerful imaging instruments (e.g., Gomez et al. 1993b,a). One of the target of this thesis is to investigate fine structuring on coronal loops.

Another important feature of coronal loops is that their cross-section is constant along their length above the transition region (e.g. Klimchuk 2006), but there is evidence that the cross-section varies across the transition region, as documented by Gabriel (1976). This is due to the rapid variation of plasma beta factor in transition region, and we will talk widely about this in Cap. 3.

### 1.2.2 Heating Mechanism in Coronal Loops

The question of what heats the solar corona remains one of the most important problems in astrophysics. A variety of difficult issues must be addressed: highly disparate spatial scales, physical connections between the corona and lower atmosphere, complex micro-physics, variability and dynamics (Klimchuk, 2006).

Coronal loops with temperatures near 1 MK are observed to persist longer than a characteristic cooling time, suggesting steady or quasi-steady heating (e.g., Lenz et al. 1999; Aschwanden et al. 2000). Steady heating models, however, cannot reproduce the

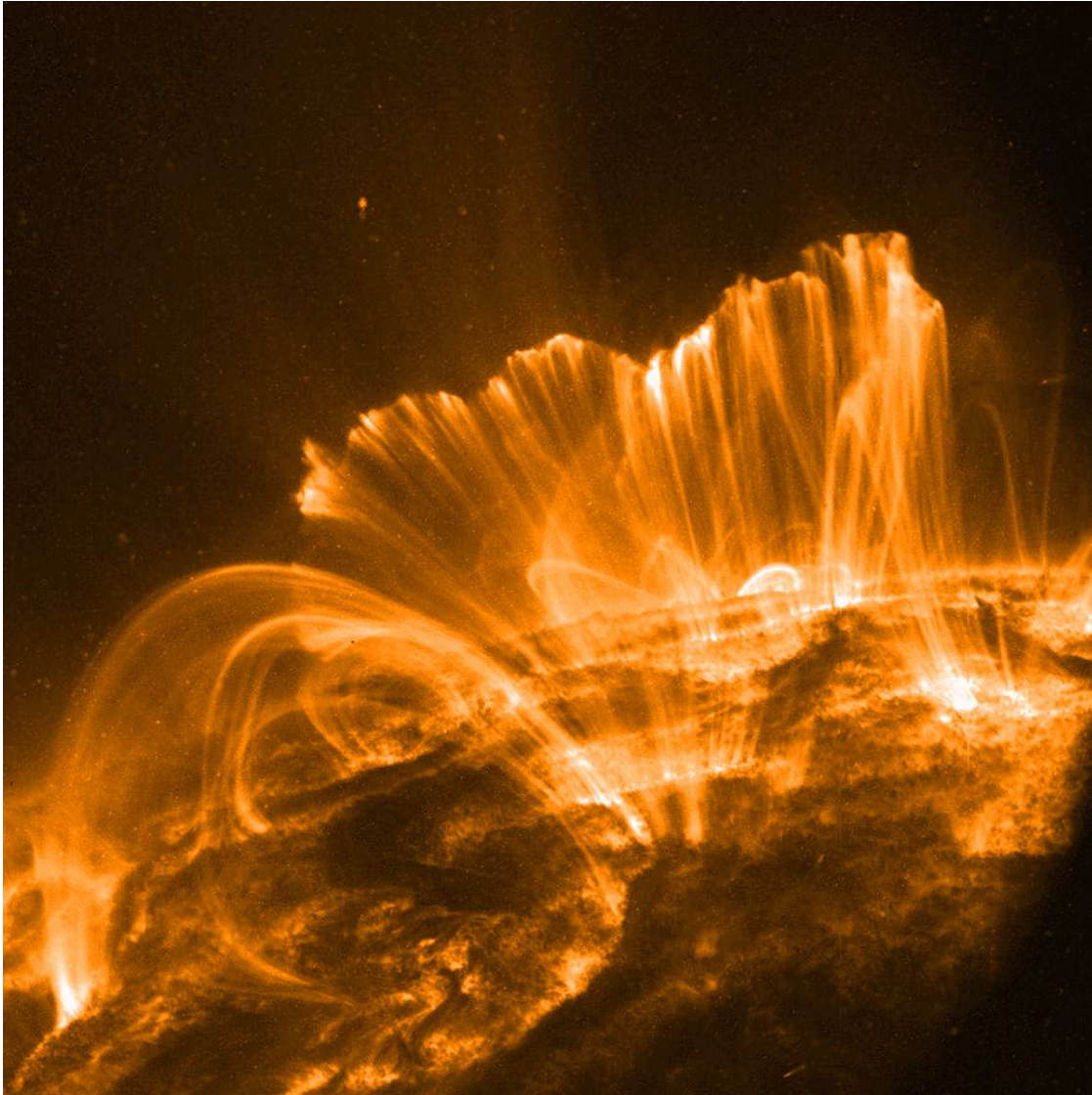


Figure 1.6 An active region observed by TRACE (9 November 2000, 2 UT). We can distinguish between strands that make the loops. Credit: NASA/TRACE.

high electron densities observed in these loops (Winebarger et al., 2003a). Multi-thread, impulsive heating models have been proposed as a possible heating scenario (e.g., Cargill & Klimchuk 1997; Warren et al. 2003; Patsourakos & Klimchuk 2008). Such models are motivated by our understanding of the energy release during magnetic reconnection in flares (e.g., Parker 1983). In these models impulsive heating leads to high densities and multiple, sub-resolution "threads" lead to long lifetimes relative to the cooling time for an individual loop.

In the 80s it was proposed that the corona is heated by rapid energy pulses, the so-called nanoflares, due to very localized reconnections of the solar magnetic field braided and twisted by the chaotic motions of the loop footpoints in the photosphere (Parker, 1988). This concept was promising and has been developed further (Cargill, 1994a; Cargill & Klimchuk, 2004). Although impulsive events were predicted to be very small and rapid, nevertheless we would expect to detect their signatures in coronal observations, such as emission of very hot plasma ( $\sim 10$  MK) outside of flares, or variability.

Although the evidence is increasing (Reale et al., 2009b,a; McTiernan, 2009; Schmelz et al., 2009; Sylwester et al., 2010), probably it still needs further support to be conclusive and there is room for possible important roles of alternative mechanisms, i.e. the more gradual dissipation of MHD Alfvén waves (Hollweg, 1984; Nakariakov et al., 1999; Ofman & Wang, 2008), or even the direct involvement of the underlying chromosphere (De Pontieu et al., 2011).

Indeed, there are good reasons why extensive nanoflaring activity has been elusive so far (Klimchuk, 2006; Reale, 2010). The most important one is that nanoflares are predicted to be small both in time and space: one nanoflare is expected to ignite not an entire coronal loop at a time, but a very small part of it. Since in the magnetic field channels momentum and energy are transported only along the field lines, we expect long and thin channels to be heated by single pulses. Such strands are so thin as to be spatially unresolved by current telescopes, and the detection of hot plasma is difficult with the current set of instrumentation because of its small filling factor (Martens et al., 1985)

### 1.3 Modelling of Coronal Loops

The concept of numerical loop modeling is to use simulations, first of all, to get insight into the physics of coronal loops, i.e., the reaction of confined plasma to external drivers, to describe plasma evolution, and to derive predictions to compare with observations. One major target of modeling is, of course, to discriminate between concurrent hypotheses, for instance, regarding the heating mechanisms and to constrain the related parameters.

Usually, this kind of models require to be provided with initial loop conditions and boundary conditions. Since we actually ignore the specific heating mechanisms of coronal loops, almost all models require to define an input heating function, specifying its time-dependence, for instance it can be steady, slowly or impulsively changing, and its position

in space. The output typically consists of distributions of temperature (and/or pressure), density, and velocity along the loop evolving with time. From simulation results, some modelers derive observable, i.e., the plasma emission, which can be compared directly to data collected with the telescopes. The model results are, in this case, to be folded with the instrumental response. This forward-modeling allows to obtain constraints on model parameters and, therefore, quantitative information about the questions to be solved, e.g., the heating rate and location (e.g. Reale et al. 2000).

### 1.3.1 Basic

The basics of loop modeling have been established since 70s (Priest, 1978). In typical coronal conditions, the plasma  $\beta$  factor (ratio of thermal and magnetic pressure) is  $\ll 1$ . This means that magnetic field dominates the loop evolution. In particular, the plasma confined in coronal loops can be assumed as a compressible fluid moving and transporting energy only along the magnetic field lines (Rosner et al., 1978), so the magnetic field has only the role of confining the plasma. Another typical assumption is a constant loop cross-section. In these conditions, it is possible to describe the loop evolution by means of the one dimensional hydrodynamic equations for a compressible fluid, using only the coordinate along the loop. Here I report the equation of conservation of mass (eq. 1.1), momentum (eq. 1.2), and energy (eq. 1.3) for a viscous optically thin plasma.

$$\frac{\partial n_e}{\partial t} + \frac{\partial}{\partial s} (n_e v) = 0 \quad (1.1)$$

$$\frac{\partial n_e v}{\partial t} + \frac{\partial}{\partial s} (n_e v v) = -\frac{\partial p}{\partial s} + n_e g + \frac{\partial}{\partial s} \left( \mu \frac{\partial v}{\partial s} \right) \quad (1.2)$$

$$\frac{\partial u}{\partial t} + \frac{\partial}{\partial s} [(u + p) v] = n_e g \cdot v + Q_H - n_e^2 P(T) + \mu \left( \frac{\partial v}{\partial s} \right)^2 - \frac{\partial}{\partial s} F_c \quad (1.3)$$

$$u = \frac{1}{2} n_e v^2 + \varepsilon \quad (1.4)$$

$$p = (\gamma - 1) \varepsilon \quad (1.5)$$

$$p = k_B n_{spec} n_e T \quad (1.6)$$

where  $n_e$  is the electron density,  $v$  is the velocity along the loop ( $s$  direction),  $u$  is the total energy density,  $g$  the gravity for a curved coronal loop,  $\varepsilon$  the thermal energy,  $p$  the pressure,  $T$  the temperature,  $P(T)$  are the radiative losses for an optically thin plasma (e.g. Raymond et al. 1976),  $Q_H$  the heating function,  $\gamma = 5/3$  is the ratio between the specific



heat capacities per unit of pressure and unit of volume ( $C_P/C_V$ ),  $n_{spec} = 2$  is the number of species,  $\mu$  the effective plasma viscosity, and  $F_c$  is the conductive flux, described by:

$$F_c = -kT^{\frac{5}{2}} \frac{\partial}{\partial s} T \quad (1.7)$$

where  $k = 9.22 \cdot 10^{-7} \text{ WK}^{-\frac{7}{2}}$  is the plasma conduction coefficient (Spitzer, 1965).

These equations can be solved numerically and several specific codes have been used extensively to investigate the physics of coronal loops and of X-ray flares (Peres et al. 1982; Betta et al. 1997; Nagai 1980; MacNeice 1986; Hansteen 1993). Also, these types of models require to be provided with initial loop conditions and boundary conditions. The model results are to be folded with the instrumental response.

### 1.3.2 Fine Structuring and multi/stranded models

In the last years, through the observations of TRACE SoHO and SDO, it has been discovered that coronal loops are composed by bundles of thin strands. We can consider each strand as self-standing, with an isolated and independent atmosphere, so they can be treated exactly as a single loop. This approach has been adopted both to describe loops as static (Reale & Peres, 2000) and as impulsively heated by nanoflares (Warren et al., 2002). On the same line, collections of loop models have been applied to describe entire active regions (Warren & Winebarger, 2006).

This model can be used to describe tree different scenario: we can consider multi-strand static models (e.g. Reale & Peres 2000), or multistrand steady heating models (e.g. Winebarger et al. 2011), or use a nanoflare heated multistranded model (see Cap. 2).

The nanoflare scenario is approached in multi-thread loop models, convolving the independent hydrodynamic evolution of the plasma confined in each pulse-heated strand. These are able to match many features of the evolution of warm loops observed with TRACE (Warren et al., 2002, 2003; Winebarger et al., 2003a,b). It has been shown (Warren et al., 2003) that a loop made as a set of small-scale, impulsively heated strands can generally reproduce the spatial and temporal properties of the observed loops, such as a delay between the appearance of the loop in different filters.

However, both monolithic and multistranded hydrodynamic models show an excess of emission in low temperature bands (from  $10^5$  to  $10^6 \text{ K}$ ) if compared with observations. This emission is localized at the basis of the loop in the region near and through the transition region. This region is called moss region, and it is a very well-known feature in the low temperature bands, already studied in NIXT and TRACE observations and commonly explained as the bright warm footpoints of hot high-pressure loops (Peres et al., 1994; Fletcher & de Pontieu, 1999; Martens et al., 2000).

Although multistrand models appear much more complex than single loop models and need further refinements to match all the observational constraints, they certainly represent an important issue for the future of coronal loop comprehension.

### 1.3.3 Interaction with Magnetic Field: MHD Modeling

In order to study the interaction between plasma and magnetic field it is necessary to include also the evolution of magnetic field in our model. For example, recent studies have investigated loops heating mechanism by including also the magnetic field in the modeling. In the last years several fully magnetohydrodynamic (MHD) codes have been developed thanks also to the increasing availability of High Performance Computing (HPC) systems and resources.

Although such models still cannot resolve well fine structures, such as current sheets and the transition region, they certainly represent the first important step toward fully self-consistent modeling of the magnetized corona. In this section we will illustrate the equations of magnetohydrodynamic.

#### The induction equation

Considering the Maxwell equations, we have (e.g. Priest 1987):

$$\nabla \times \mathbf{B} = \mu \mathbf{j} + \frac{1}{c^2} \frac{\partial \mathbf{E}}{\partial t} \quad (1.8)$$

$$\nabla \cdot \mathbf{B} = 0 \quad (1.9)$$

$$\nabla \times \mathbf{E} = -\frac{\partial \mathbf{B}}{\partial t} \quad (1.10)$$

$$\nabla \cdot \mathbf{E} = \frac{\rho^*}{\varepsilon} \quad (1.11)$$

where  $\mathbf{E}$  is the *electric field*,  $\mathbf{B}$  is the *magnetic field*,  $\rho^*$  is the *charge density*,  $\mathbf{j}$  is the *current density*  $\mu$  ( $\approx \mu_0 = 4\pi \times 10^{-7} \text{ Hm}^{-1}$ ), the magnetic permeability and  $\varepsilon$  ( $\approx \varepsilon_0 = 8.854 \times 10^{-12} \text{ Fm}^{-1}$ ) the permittivity, such that the speed of light in a vacuum is:

$$c = \frac{1}{\sqrt{\mu_0 \varepsilon_0}} \approx 2.998 \times 10^8 \text{ ms}^{-1} \quad (1.12)$$

It is convenient to eliminate  $\mathbf{E}$  and  $\mathbf{j}$  from eq. 1.8 and 1.10, using the *Ohm law*:

$$\mathbf{j} = \sigma (\mathbf{E} + \mathbf{v} \times \mathbf{B}) \quad (1.13)$$

to give:

$$\frac{\partial \mathbf{B}}{\partial t} = -\nabla \times \left( -\mathbf{v} \times \mathbf{B} + \frac{\mathbf{j}}{\sigma} \right) = \nabla \times (\mathbf{v} \times \mathbf{B}) - \nabla \times (\eta \nabla \times \mathbf{B}) \quad (1.14)$$

where  $\sigma$  is the *electric conductivity* (measured in *mho m<sup>-1</sup>*), and  $\eta = 1/(\mu\sigma)$  is the *magnetic diffusivity*. Using eq. 1.9, and the vector identity:

$$\nabla \times (\nabla \times \mathbf{B}) = \nabla (\nabla \cdot \mathbf{B}) - (\nabla \cdot \nabla) \mathbf{B} \quad (1.15)$$

one finds

$$\frac{\partial \mathbf{B}}{\partial t} = \nabla \times (\mathbf{v} \times \mathbf{B}) + \eta \nabla^2 \mathbf{B} \quad (1.16)$$

that is known as the *induction equation*. If  $\mathbf{v}$  is known it is possible to use this equation to determine  $\mathbf{B}$ , that must be subject to the eq. 1.9 in any case.

Now we can define the *magnetic Reynolds Number*:

$$R_m = \frac{l_0 V_0}{\eta} \quad (1.17)$$

where  $V_0$  is the typical plasma speed, and  $l_0$  is the magnitude of the convective term (the first term) in eq. 1.16.

Clearly, if  $R_m \gg 1$  eq. 1.16 we can omit the second term (*perfectly conducting limit*) otherwise, if  $R_m \ll 1$  eq. 1.16 reduces to a simple diffusion equation (*diffusive limit*):

$$\frac{\partial \mathbf{B}}{\partial t} = \nabla \times (\mathbf{v} \times \mathbf{B}) + \eta \nabla^2 \mathbf{B} \approx \begin{cases} \nabla \times (\mathbf{v} \times \mathbf{B}) & R_m \gg 1 \\ \eta \nabla^2 \mathbf{B} & R_m \ll 1 \end{cases} \quad (1.18)$$

In chap. 3 we will use eq. 1.18 in the perfectly conducting limit.

### Conservation equations

The presence of magnetic field enters also the momentum equation through the presence of *Lorenz force*, so the eq. 1.2 must be rewritten (omitting the viscous term):

$$\frac{\partial n_e \mathbf{v}}{\partial t} + \nabla \cdot (n_e \mathbf{v} \mathbf{v}) = -\nabla p + n_e \mathbf{g} + \mathbf{j} \times \mathbf{B} \quad (1.19)$$

The magnetic field enters also in the equation of conservation of energy. We can rewrite eq. 1.3 to obtain:

$$\frac{\partial u}{\partial t} + \nabla \cdot [(u + p) \mathbf{v} - \mathbf{B}(\mathbf{v} \cdot \mathbf{B})] = n_e \mathbf{g} \cdot \mathbf{v} + Q_H - n_e^2 P(T) - \nabla \cdot \mathbf{F}_c \quad (1.20)$$

or (if we consider also the resistive term):

$$\frac{\partial u}{\partial t} + \nabla \cdot [(u + p) \mathbf{v} - \mathbf{B}(\mathbf{v} \cdot \mathbf{B})] = n_e \mathbf{g} \cdot \mathbf{v} + Q_H - n_e^2 P(T) - \nabla \cdot \mathbf{F}_c - \nabla \cdot [(\eta \cdot \mathbf{J}) \times \mathbf{B}] \quad (1.21)$$

where  $\eta$  is the magnetic resistivity tensor, and  $\mathbf{F}_c$  is the conductive flux.

In the MHD case, thermal conductivity is highly anisotropic, being largely suppressed in the direction transverse to the field. Denoting with  $\hat{\mathbf{b}} = \mathbf{B}/|\mathbf{B}|$  the unit vector in the direction of magnetic field, the classical thermal conduction flux may be written as (Balbus, 1986):

$$\mathbf{F}_{\text{class}} = k_{\parallel} \hat{\mathbf{b}} (\hat{\mathbf{b}} \cdot \nabla T) + k_{\perp} [\nabla T - \hat{\mathbf{b}} (\hat{\mathbf{b}} \cdot \nabla T)] \quad (1.22)$$

where the subscripts  $\parallel$  and  $\perp$  denote, respectively, the parallel and normal components to the magnetic field,  $k_{\parallel} (= K_{\parallel} T^{5/2})$  and  $k_{\perp} (= K_{\perp} \rho^2 / |\mathbf{B}|^2 T^{1/2})$  are the thermal conduction coefficients along and across the field, and  $K_{\parallel}$  and  $K_{\perp}$  are constants. Clearly, in the pure hydrodynamic limit eq 1.22 becomes  $\mathbf{F}_{\text{class}} = k_{\parallel} \nabla T$ .

If we take into account the effect of saturated thermal conduction (Spitzer, 1965), the flux becomes independent of  $\nabla T$  for very large temperature gradients. In this limit the flux magnitude approaches to:

$$F_{\text{sat}} = \phi K_{\text{sat}} n_e c_{\text{iso}}^3 \quad (1.23)$$

where  $K_{\text{sat}}$  is a constant,  $c_{\text{iso}}$  is the sound speed in isothermal conditions, and  $\phi \ll 1$  is a free parameter.

A typical flux limiter used to smoothly switch between classical (eq. 1.22) and saturated (eq. 1.23) thermal conduction is to use the equation (Mignone et al., 2011):

$$\mathbf{F}_{\text{c}} = \frac{F_{\text{sat}}}{F_{\text{sat}} + |\mathbf{F}_{\text{class}}|} \mathbf{F}_{\text{class}} \quad (1.24)$$

where:

$$|\mathbf{F}_{\text{class}}| = \sqrt{(\hat{\mathbf{b}} \cdot \nabla T)^2 (k_{\parallel}^2 - k_{\perp}^2) + k_{\perp}^2 \nabla T^2} \quad (1.25)$$

The assumption made in deriving previous equations are:

- Plasma is treated as continuum;
- Plasma is in thermodynamic equilibrium;
- The coefficients  $\mu$  and  $\eta$  are uniform;
- Most of the plasma properties except the thermal conduction coefficient are isotropic;
- The equation are written for an inertial frame of reference;
- No one relativistic effect are included;
- The plasma is treated as a single fluid;

### 1.3.4 Outline of the thesis

This thesis is developed under the general scope of studying the fine structure of coronal loops.

The first part (Chap. 2) studies the diagnostics of loops as bundles of fine pulse-heated strands. Since each strand cannot be spatially resolved by present-day instruments, modeling is used here to look for new indirect evidence. In particular, we investigate whether multi-strand loops can explain the evidence of increasing fuzziness of coronal regions at increasing temperatures. To this purpose, it is convenient to treat each strand as strictly independent of the others and to describe the loops as collections of identical strands. The approach is then to use standard loop hydrodynamic modeling to model a single pulse-heated strand, to replicate and shuffle the model strand until a proper loop system is built, and to compare the emission predicted after this procedure with observations. Observations from Hinode/EIS and SDO/AIA are considered.

The second part (Chap. 3) addresses a different kind of evidence, and in particular investigates whether multi-structured loops can be diagnosed with observations of the lower parts of the loops, around the transition region. We address moss-like structures in active regions detected at temperatures about 1 MK, that are generally interpreted as the footpoints of hotter loops. To study the low-lying parts of the loops in high detail, the assumption of constant cross-section all along the loop cannot hold, because it is known that the loop greatly expands going up from the transition region to the corona (e.g. (Gabriel, 1976)). We cannot help including this effect in the modeling, and how it changes in time and with the plasma  $\beta$ , and this requires a proper time-dependent magnetohydrodynamic description. In this part a two-dimensional time-dependent magnetohydrodynamic loop model is described and its first application to study how the heating and dynamics of the plasma influences the expansion itself.

## **Chapter 2**

# **Modeling of Multistranded Coronal Loops**

In this chapter we study the fine structuring of coronal loops. We suppose that coronal loops are substructured in a multitude of thin strands; each strand is heated by a strong energy pulse, and the duration of the pulse is much smaller than the characteristic cooling time of the plasma. Once the heat pulse ends, the plasma cools down exponentially. The loops strands are ignited at different times, and the storm of nanoflares goes on for a long time, comparable to the loop lifetime. On timescales long compared with those characteristics of the heat pulses, a loop strand will be heated and hot only occasionally. If we image a loop, or, more in general, the active region, at a certain time, there will be a minority of strands where the heat pulse is on, and most of them will be instead cooling. We can put this in other words by saying that a few strands will be very hot, and many of them will be significantly cooler than their peak temperature. How hot, how cooler? If nanoflares are the same kind of events as proper coronal flares, only on a smaller spatial scale, it is quite likely that the plasma is heated up to temperatures of about 10 MK. However, these temperatures are maintained for very short times, during which the emission is faint because of the low plasma density: the strand becomes brighter as it is filled with dense plasma coming up from the chromosphere, and this occurs on time scales longer than the expected duration of the heat pulses. Therefore, the strands become bright when the plasma is already cooling and remain bright until the plasma has drained significantly. Thus, in this scenario, we expect to see few hot 10 MK and cold 1 MK strands, and many 3 MK strands.

In the course of the work of this PhD thesis we show that one implication of this model is to explain the fact that coronal active regions are observed to get fuzzier and fuzzier (i.e. more and more confused and uniform) in harder and harder energy bands or lines. In fact, comparison of observations in different bands and different lines has shown that the confined corona, and in particular active regions, appear to be fuzzier in hotter bands and lines, better defined in cooler ones (e.g. Brickhouse & Schmelz 2006; Tripathi et al. 2009). More specifically, according to Tripathi et al. (2009), a loop bundle is fuzzier when it is difficult to resolve the single loops and less fuzzy when the separations between loops are more clear and with a higher contrast. This effect has been well observed with imaging instruments e.g. TRACE (Brickhouse & Schmelz, 2006). A very clear example comes from imaging spectroscopy obtained with Hinode/EIS: in *Fig. 2.1* we report an image from Tripathi et al. (2009). From left to the right in the top pannels we can see the active region shown inlines sensitive to hotter and hotter plasma, from less than 1 MK to 3 MK. The bottom pannels show cuts of the intensity along the white lines. We see that the loops are better defined in the left lines and less in the right, and we say that the coronal structures on the right are fuzzier than those on the left.

In the next sections we will show our model of multistranded loop heated by impulsive events, and compare the results obtained from the model with some observational evidence.

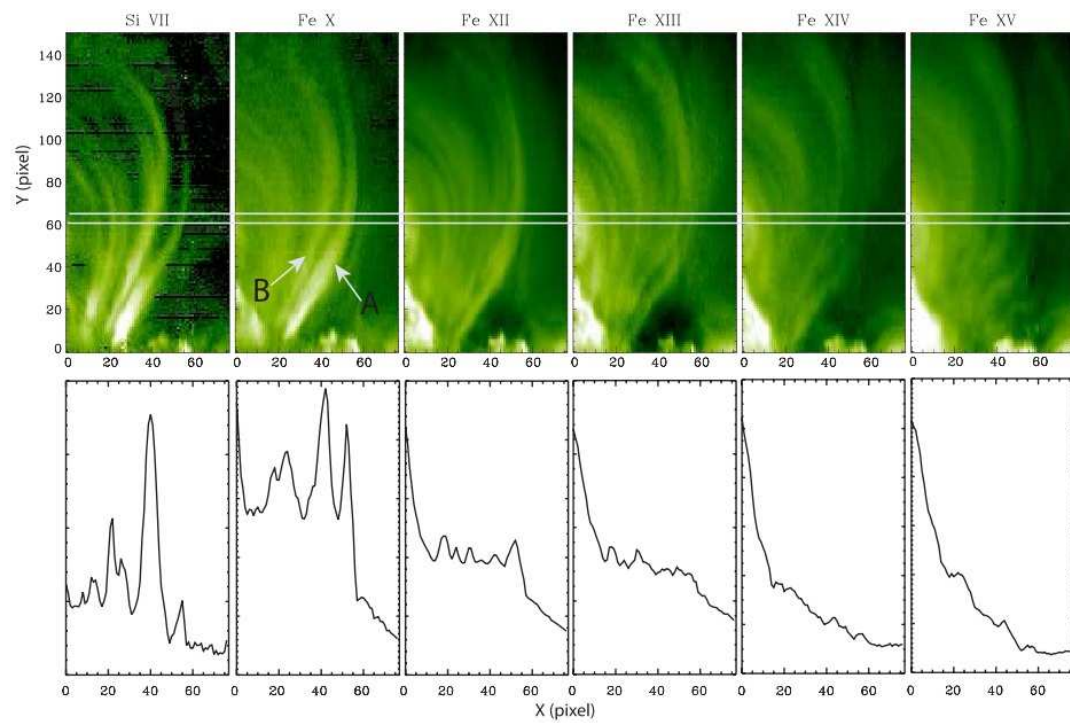


Figure 2.1 From Tripathi et al. (2009). Top panel: An active region loops seen at different temperatures. Bottom panels: Total intensity variation in the region marked by the two white lines in the corresponding top panels.



## 2.1 The Model

We address a typical loop system of an active region. The system is a bundle of similar loops, each consisting of many thin strands. Each strand is pulse-heated. Before the heating, the strand is tenuous and cold, actually invisible. The loops consist of multitudes of strands, and, in principle, we should compute the hydrodynamic evolution for each of them. Instead of doing this, we make the simplifying assumption that the loops are made of similar strands and that each strand is heated by the same identical heat pulse, and therefore undergoes the same identical evolution. The heating rate averaged over the whole loop system is that of a steady-state loop at 3 MK, i.e. a typical active region temperature. We assume a constant rate of heat pulses across the loops. Therefore, the steady state is reached after a transient in which the number of strands with an on-going heat pulse increases linearly. The loop half-length is  $L = 3 \times 10^9$  cm. We assume that the loops stand vertical on the solar surface.

### 2.1.1 The Equations

Since the plasma confined in each strand moves and transports energy only along the magnetic field lines, each strand can be described with a 1D hydrodynamic model (Nagai, 1980; Peres et al., 1982; Doschek et al., 1982; Nagai & Emslie, 1984; Fisher et al., 1985; MacNeice, 1986; Gan et al., 1991; Hansteen, 1993; Betta et al., 1997; Antiochos et al., 1999; Müller et al., 2003; Bradshaw & Mason, 2003; Bradshaw & Cargill, 2006), through the equations (Peres et al., 1982; Betta et al., 1997):

$$\frac{dn}{dt} = -n \frac{\partial v}{\partial s} \quad (2.1)$$

$$nm_H \frac{dv}{dt} = -\frac{\partial p}{\partial s} + nm_H g + \frac{\partial}{\partial s} \left( \mu \frac{\partial v}{\partial s} \right) \quad (2.2)$$

$$\frac{d\varepsilon}{dt} + w \frac{\partial v}{\partial s} = Q - n^2 \beta P(T) + \mu \left( \frac{\partial v}{\partial s} \right)^2 + \frac{\partial}{\partial s} \left( \kappa T^{5/2} \frac{\partial T}{\partial s} \right) \quad (2.3)$$

$$p = (1 + \beta) n K_B T \quad (2.4)$$

$$\varepsilon = \frac{3}{2} p + n \beta \chi \quad (2.5)$$

$$w = \frac{5}{2} p + n \beta \chi \quad (2.6)$$

where  $n$  is the hydrogen number density;  $t$  is the time,  $s$  is the field line coordinate;  $v$  is the plasma velocity;  $m_H$  is the mass of hydrogen atom;  $p$  is the pressure;  $g$  is the component

of gravity along the field line;  $\mu$  is the effective coefficient of compressional viscosity (including numerical viscosity);  $\beta = n_e/n$  is the ionization fraction where  $n_e$  is the electron density;  $T$  is the temperature;  $\kappa$  is the thermal conductivity ( $\simeq 9 \cdot 10^{-7} \text{ erg cm}^{-1} \text{ s}^{-1} \text{ K}^{-7/2}$ );  $K_B$  is the Boltzmann constant;  $\chi$  is the hydrogen ionization potential;  $P(T)$  are the radiative losses per unit emission measure (Raymond & Smith, 1977);  $Q(s, t)$  is the volumetric power input to the solar atmosphere:

$$Q(s, t) = H_{steady} + H_0 f(t) h(s) \quad (2.7)$$

$H_{steady}$  is the steady heating term which balances radiative and conductive losses for the static initial atmosphere; the second term describes the heat pulse as a separable function of space and time.

### 2.1.2 Strand initial conditions

As mentioned above, the initial atmosphere of all the strands is tenuous and cool, since we want them to be virtually invisible in any relevant spectral band. On the other hand, the initial atmosphere has anyhow to sustain a high input energy; in particular, the chromosphere has to provide a mass amount large enough to support the evaporation driven by the heat pulse. This requires that the strand pressure cannot be too low. Apart from this, the fine details of the initial strand are not important because the energy input from the heat pulse overwhelms completely the initial energy budget and the evolution is largely independent of the initial atmosphere. A good compromise solution for this technical issue has been a loop strand with a base pressure of  $0.55 \cdot 10^{-1} \text{ dyn cm}^{-2}$ , which results in an apex temperature of  $8.0 \times 10^5 \text{ K}$ . Since the emission of such a strand would be low but not be completely negligible in UV lines such as Mg VII and Si VI, for the sake of clarity we have decided anyway only for the analysis to set the emission of the initial strands to zero at any wavelength. For the chromospheric part of the strand we use model F in Vernazza et al. (1981), appropriate for active regions. The energy balance is strictly maintained at all times also in the chromosphere.

### 2.1.3 The strand heating

The heat pulse is distributed uniformly along the loop strand:

$$h(s) = \begin{cases} 1 & \text{if } 0 \leq s \leq L \\ 0 & \text{elsewhere} \end{cases} \quad (2.8)$$

The results do not change significantly if the heat pulses are deposited at the loop footpoints, instead of uniformly, one of the options explored by Reale & Orlando (2008).

The time dependence is a pulse function:

$$f(t) = \begin{cases} 1 & \text{if } t_0 \leq t \leq t_0 + 60 \text{ sec} \\ 0 & \text{any other } t \end{cases} \quad (2.9)$$

where  $t_0$  is the start time of heat pulse.

The amplitude of the pulse is  $H_0 = 0.38 \text{ erg cm}^{-3} \text{ s}^{-1}$ .

Note that the duration of heat pulse is short enough to have a multi-temperature loop system, and not so short to have large effects on the overall evolution and emission due to non-equilibrium of ionization (Reale & Orlando, 2008). Small variations in duration and amplitude of the heat pulses don't affect significantly the results of simulations. We chose the total amount of energy of the heat pulse to reach the temperature of 10 MK during the heating phase.

### 2.1.4 The Code

The equations are solved numerically by means of the Palermo-Harvard loop code (Peres et al., 1982; Betta et al., 1997). This is a well tested and highly stable code, used for both flaring (Peres et al., 1987; Betta et al., 2001) and quiescent loops (Reale et al., 2000). The Palermo-Harvard code has an adaptive grid (Betta et al., 1997), to better describe the steep gradients along the strands and during the evolution. For the ease of post-processing, the code output results were interpolated on a fixed equispaced grid for the post-processing. The grid is made of 1024 cells along the strand.

The code output consists of temperature, density and velocity distributions along the loop strand sampled with a regular cadence during the strand evolution driven by the heat pulse.

### 2.1.5 The Loop System

As mentioned above we model only one strand and replicate it so that one strand is different from the other only for the start time of the heat pulse, i.e.  $t_0$ . This choice minimizes the number of free parameters, and a single simulation was enough for our further analysis. The simulation computes the evolution of the strand for 2000 s after the start of the heat pulse, and the solutions are sampled every 1 s.

We have also assumed that all the strands are strictly out of phase, i.e. only one strand is switched on at any time. At time  $t = 0$  all strands are switched off. Then the heat pulses gradually turn them on, one after the other. We have chosen to turn them on with constant cadence to have a smooth transition from no bright strands to maximum number of bright strands (Fig. 2.5).

At a certain time, part of the strands will still be off, in a few the heat pulse will be on, the others will be cooling after the heat pulse has ended. Since all strands have the same evolution, at each time each strand will be at a different phase of the same evolution. A

whole loop at a given time is therefore simulated as a set of otherwise identically evolving strands, but each with a different heating start, all glued together. This approach is not completely new; outputs of the same loop simulation have been put together in the past to simulate multistrand nanoflaring loops (Peres et al., 1993; Warren et al., 2002, 2003; Winebarger et al., 2003a,b) but in all cases they were *averaged* to obtain the effective aspect and evolution of a loop as a whole. The novelty of our approach is that we do not model each loop as whole, but we keep the information of its spatial longitudinal and transversal distribution.

In our model one heat pulse is switched on every one second in one new strand. One loop consists of  $\approx 60$  strands and we put  $\approx 30$  loops one by the other. Every second there are 60 strands where the heat pulse is on out of a total of 2000. In the steady-state the loop heating per unit volume is therefore  $\overline{H} = H_0 \times 60/2000 \approx 0.011 \text{ erg cm}^{-3} \text{ s}^{-1}$ . According to scaling law (Rosner et al., 1978), this steady heating sustains a loop with an apex temperature of  $\approx 3.8 \text{ MK}$  corresponding to an average temperature along the loop of about  $3 \text{ MK}$  (Fig. 2.5).

When we put all strands side by side, we obtain a mesh  $1024 \times 2000$  grid cells. The transversal width of each strand is constant along the loops. Therefore it is only a multiplicative constant which determines the cross-section of the entire loop system.

### 2.1.6 The Loop emission

From model results we synthesized the loop emission in different spectral lines. We selected the spectral lines, in Tab. 2.1, with a peak emissivity in a wide range of temperatures. A subset (the first seven) are detected with Hinode/EIS (Tripathi et al. (2009)), which will provide our reference observational evidence. We also include hotter lines detectable in the UV (e.g. Fe XIX, Fe XX, Fe XXIII from AIA on board the SDO mission) and X-ray band.

The emissivity in these lines ( $P_\lambda(T)$ , Fig. 2.2) is taken from the CHIANTI database (Dere et al., 1997; Young et al., 2003), with coronal abundances of Feldman (1992) (assuming a density of  $10^9 \text{ cm}^{-3}$ ), and ionization fraction of Mazzotta et al. (1998), .

The emission from each grid cell is computed as:

$$I(T, n_e) = \int_{V_{\text{pixel}}} n_e^2 P_\lambda(T) dV \quad (2.10)$$

where  $V$  is the volume,  $V_{\text{pixel}}$  is the volume enclosed by a single pixel, and  $P_\lambda(T)$  is the plasma emissivity per unit emission measure in the spectral line  $\lambda$ .

To obtain a final image to be compared with observational data we follow the conceptual steps shown in Fig. 2.3. We first compute the emission along each strand in a given line. The strand emissions can be put in the form of a 1-D image consisting of a strip of pixels on an appropriate grey scale. We obtain 2000 pixel strips. We then put them side

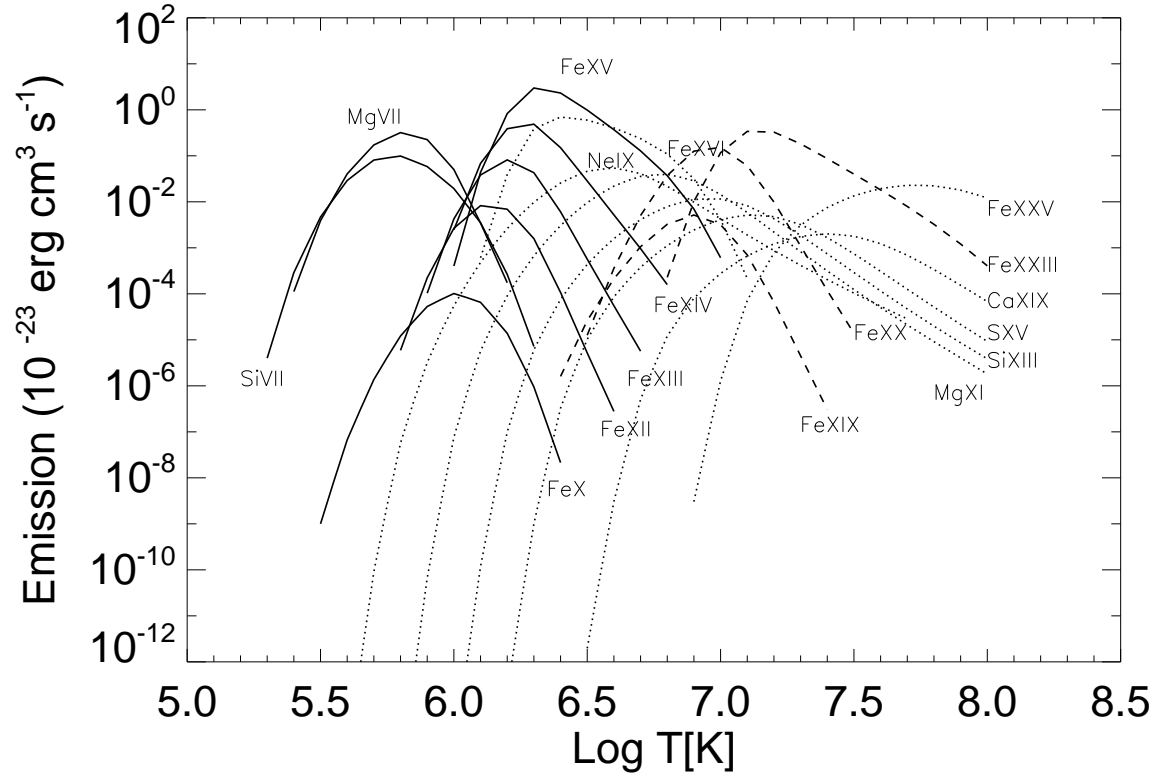


Figure 2.2 Profile of emission per unit of emission measure vs  $\log T[\text{K}]$  for the various spectral lines. We make a distinction between lines for comparison with Tripathi et al. (2009) (*solid lines*), lines in AIA filter bands on board of SDO mission (*dashed lines*), and hot X ray lines (*dotted lines*)

by side and obtain a  $1024 \times 2000$  pixel image. We have chosen to rebin our images by summing over bundles of 65 strands, so to obtain a collection of about 30 parallel loops.

## 2.2 Results

### 2.2.1 The Strand Evolution

The evolution of nanoflaring plasma confined in coronal loop is well known from previous works (Peres et al., 1993; Warren et al., 2002, 2003; Patsourakos & Klimchuk, 2005; Testa et al., 2005) and is similar to that of proper flaring loops, although on a smaller scale (e.g., Nagai (1980); Peres et al. (1982); Reale & Peres (1995)). We show the evolution of the density and temperature along a single strand in Fig. 2.4. The temperature soon settles to about 10 MK along most of the strand, due to the strong heat pulse; then it slowly decreases as expected with an e-folding time scale given by  $\tau_s \approx 500 L_9 / \sqrt{T_6} \approx 500$  s (Reale, 2007, 2010) where  $T_6$  and  $L_9$  are the maximum temperature and the length of the strand measured in units of  $10^6$  K (MK) and  $10^9$  cm respectively. At  $t = 2000$  s the strand has cooled below the temperature it had before the heat pulse. At  $t = 20$  s the density plot clearly shows a strong evaporation front coming up from the chromosphere (the density of the front jumps by more than a factor 10). At  $t = 100$  s the front has filled the whole strand with some extra accumulation in the apex region. At  $t = 400$  s the density distribution has a shape similar to the initial equilibrium one, but settled around a maximum value of  $\sim 10^{10} \text{ cm}^{-3}$ . Then the density begins to decrease and at the final time computed it is lower, by a factor  $\sim 5$  than the maximum, still much higher than the initial value.

### 2.2.2 The Loop Evolution

As described in Sec. 2.1, this evolution is replicated in all strands with different relative timing, depending on the time the heat pulse is switched on. As mentioned above, for a realistic situation, we have simulated the ignition of the whole loop system, with a gradually increasing number of simultaneously heated strands. The transient evolution will be the subject of a future work, but Fig. 2.5 shows the initial evolution of the temperature averaged over the whole loop system.

### 2.2.3 Hinode/EIS Emission

In the following we will focus our attention to the final time ( $t = 2000$  s) when the loop system enters a presumably long steady state, in which the heat pulse 'storm' (i.e. the 2000 pulses in total) repeats continuously. In a way, we are therefore implicitly assuming

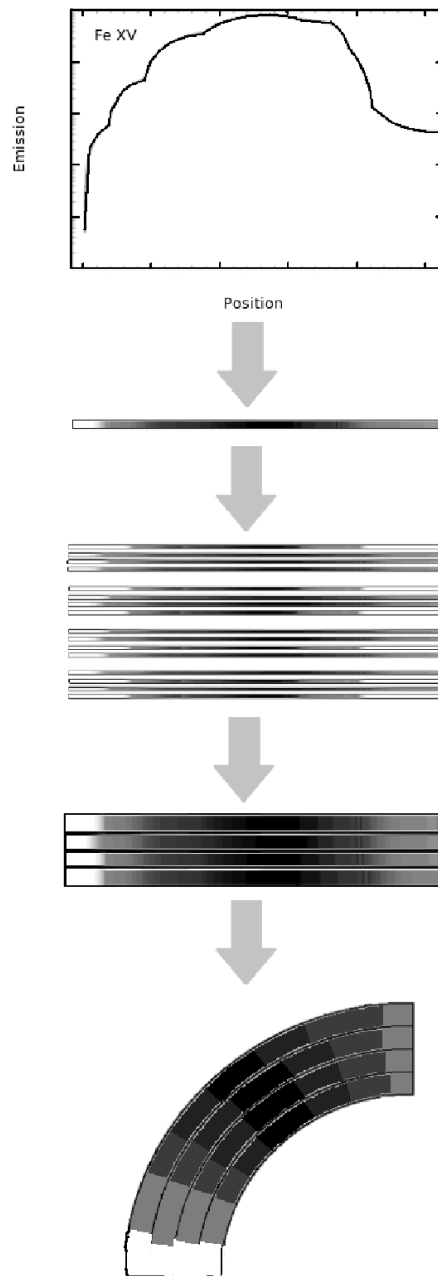
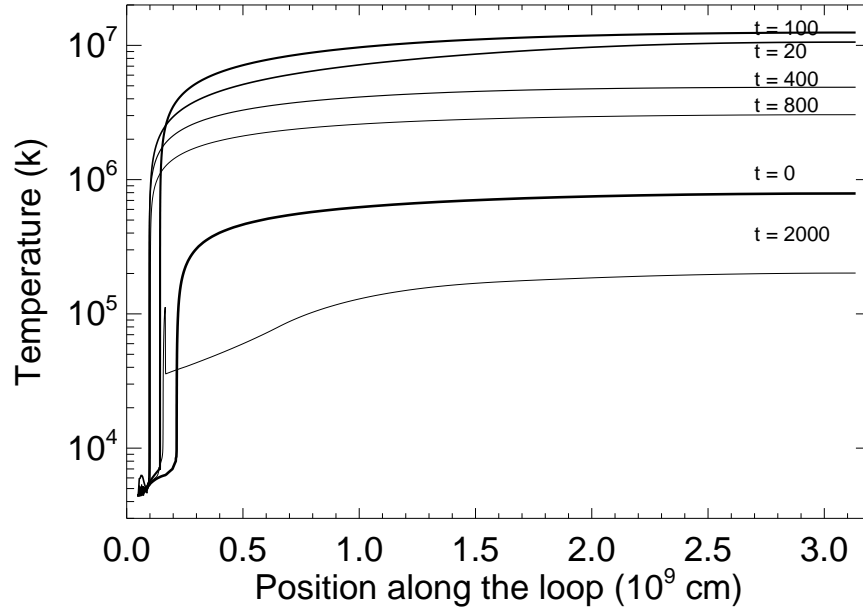
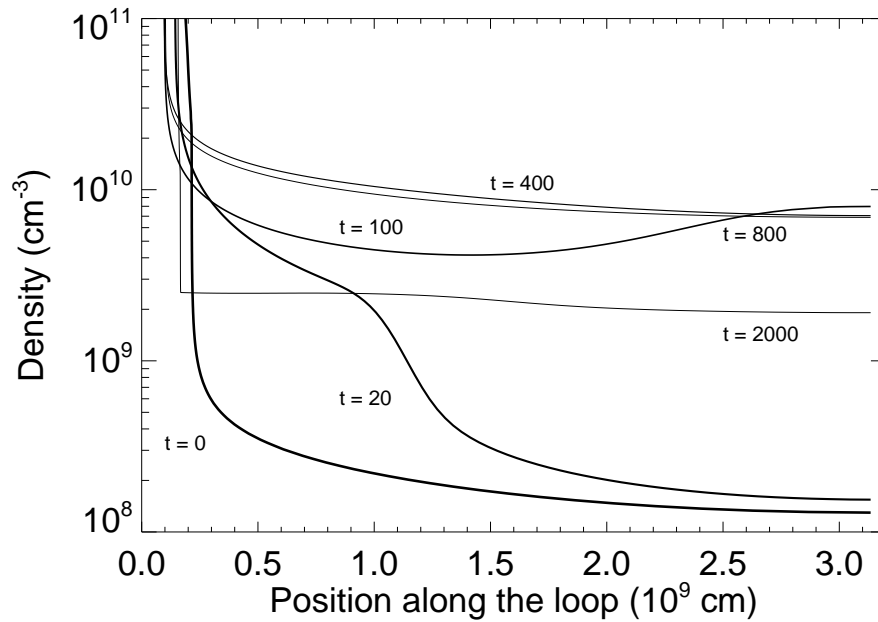


Figure 2.3 Flowchart showing how an loop bundle image is obtained from the emission of each individual loop in a given spectral line. We first compute the spatial distribution of the emission along each strand, we then put the emission in the form of an image made of a pixel strip, we put all pixel strips side by side; we then reconstruct the aspect of the whole loop system, then we group the strands into loops. Finally we bend the image to obtain a loop-like shape.



(a)



(b)

Figure 2.4 Temperature (a), and density (b) along half of a single strand at times  $t = 0, 20, 100, 400, 800, 2000$  s (thinner and thinner lines with progressing time). The heat pulse starts at time  $t = 0$  and lasts 60 s.



that the time taken to re-energise the magnetic field (e.g. by twisting, braiding) is about 2000 s.

Fig. 2.6 shows the distribution of the emission measure of the entire collection of strands, i.e. of the whole loop system, versus temperature (e.g. Cargill 1994b) at this time. We show the distribution of the coronal part only, i.e. upper 90% of the loop bundle, excluding the lower layers. The peak of the distribution is around 3 MK, as planned. We also see that the distribution is quite broad; the flatter tail is toward the cool part, but there are also significant hot components up to 10 MK, as expected, due to the presence of the strong heat pulses. These hot components are of course minor, due to the small duty cycle of the heating phase with respect to the whole evolution of the strand.

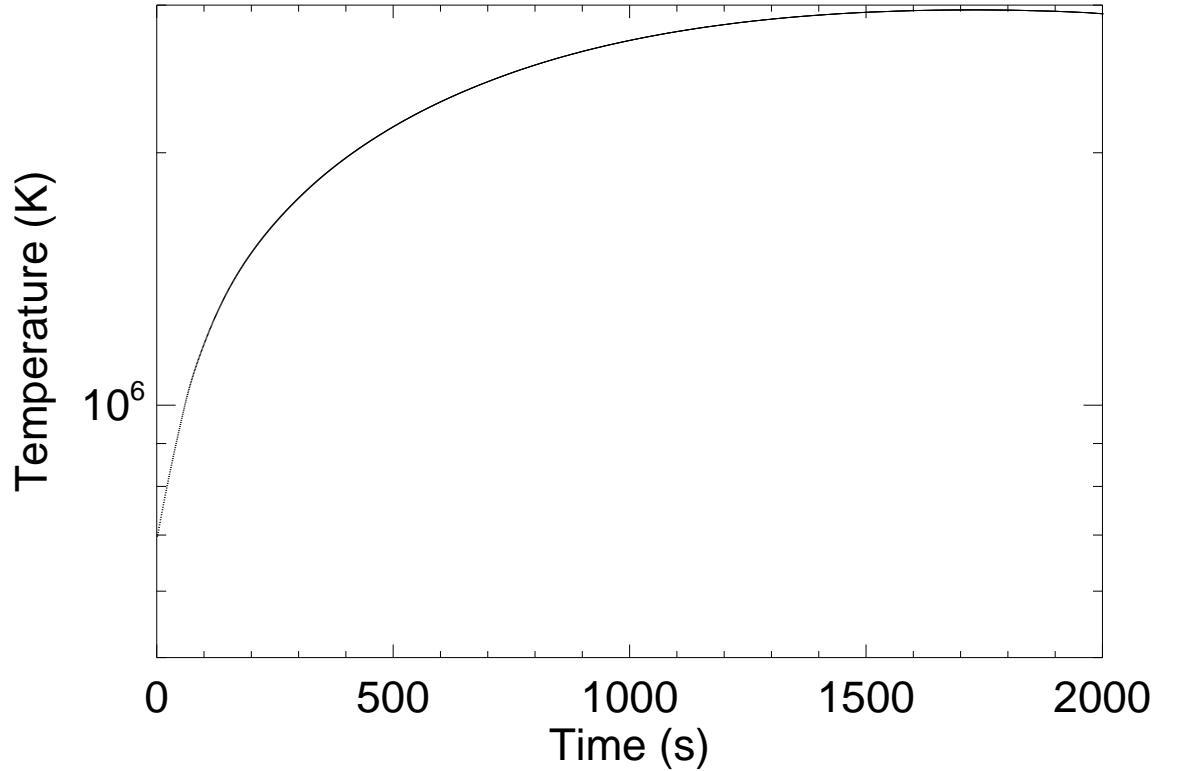


Figure 2.5 Evolution of the loop average temperature from off-state to steady-state.

Using the method described in the Sec 2.1, we synthesize maps of emission for all the lines considered. Fig. 2.7 (left column) shows a subset of them, namely the map in cool EIS lines, i.e. Mg VII ( $\lambda$  278,  $\log T[K] = 5.8$ ), medium temperature EIS line Fe X ( $\lambda$  186,  $\log T[K] = 6.0$ ), warm EIS line Fe XV ( $\lambda$  284,  $\log T[K] = 6.4$ ), and hot X-ray line Fe XXIII ( $\lambda$  133,  $\log T[K] = 7.1$ ). The images on the left column are analogous, and can be compared, to observed ones (e.g. Tripathi et al. 2009). The grey scale is logarithmic and spans a factor 10 in all maps and plots. This is a customary

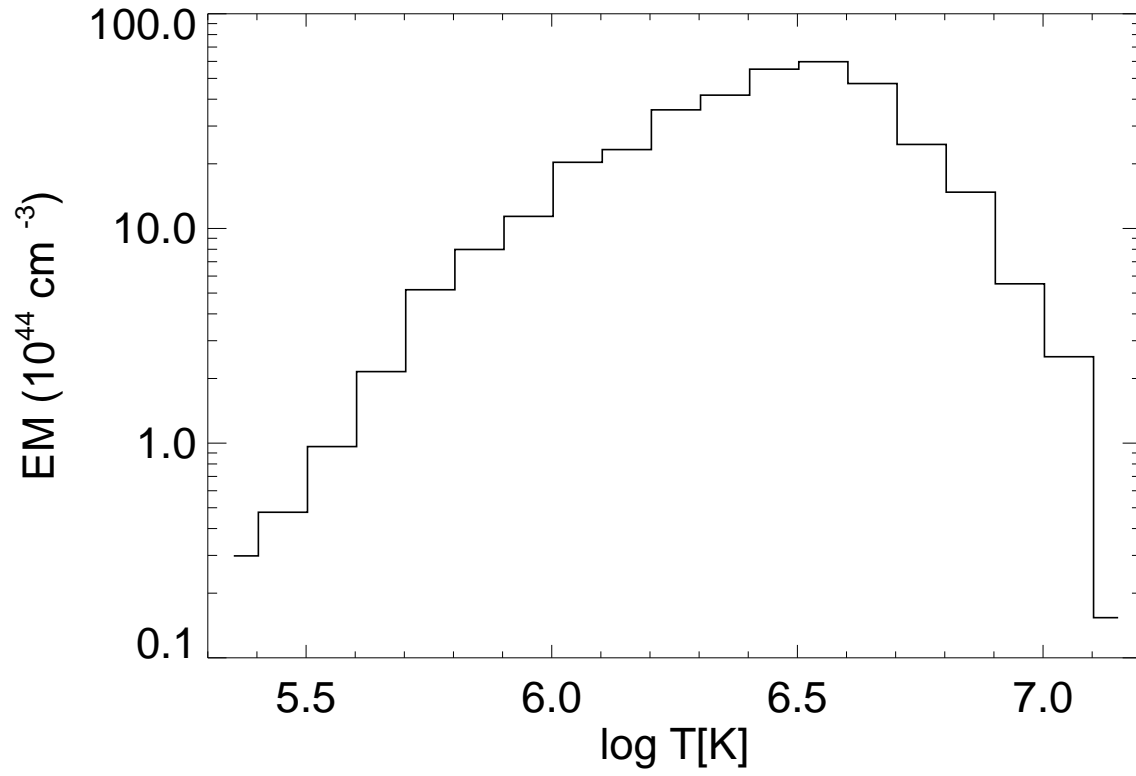


Figure 2.6 Distribution of emission measure vs Temperature at  $t = 2000$  s. We show the distribution of the coronal part only, i.e. the upper 90% of the loops.

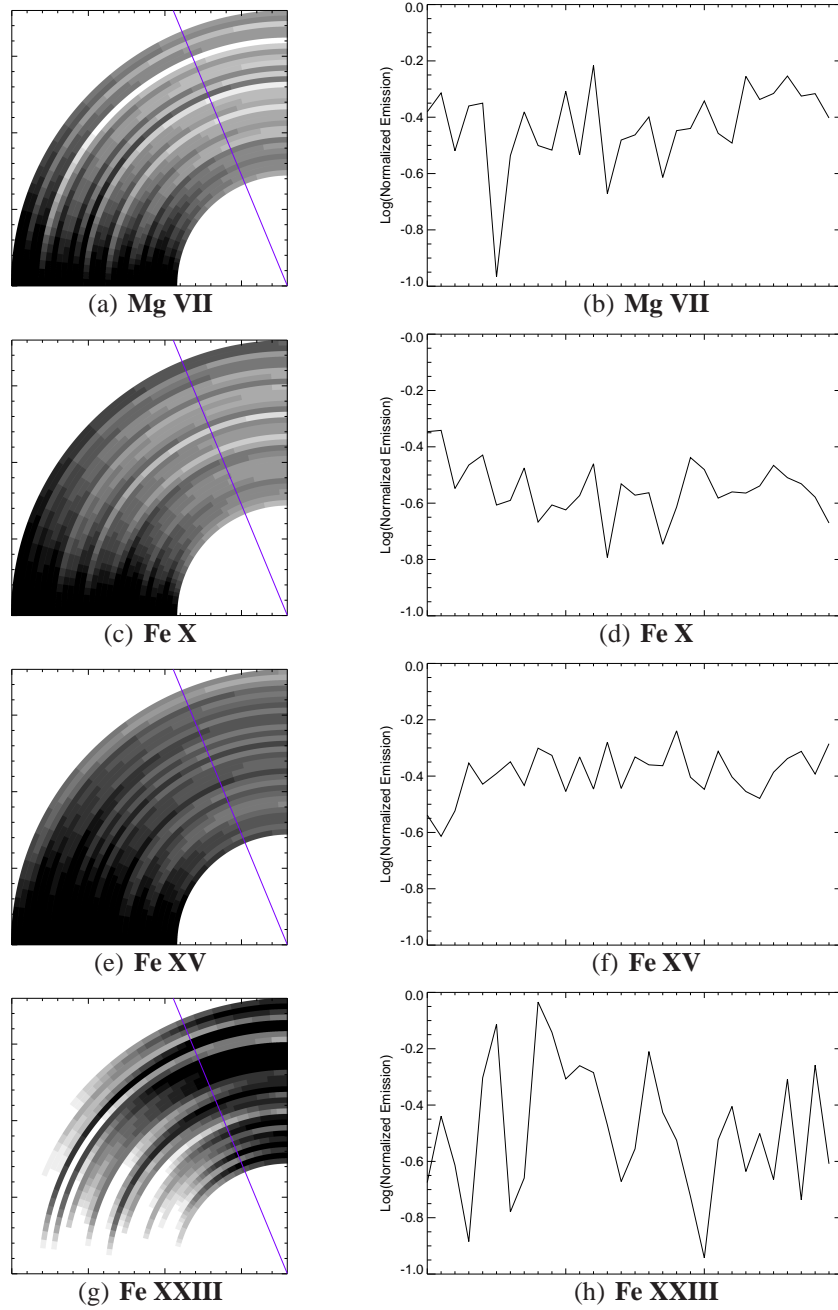


Figure 2.7 Loop bundle emission in different (labeled) spectral lines. In the images (left column) we show the upper 90% of the loop. The grey scale is logarithmic, and covers a factor 10 of intensity; black corresponds to the maximum of emission and white to the minimum. The plots in the right column are the emission profiles along the lines marked in the images of the left column, in the same logarithmic scale.

choice for showing observed data (e.g. Tripathi et al. 2009). In the first three lines, the emission decreases from the base to the top of the loop, due to the density decreasing as well. We show the intensity of the upper 90% of the loop system, i.e. the coronal part only. In this way we exclude the *moss* emission from cromosphere and transition region, which, nevertheless, would appear saturated in this color scale. This may indicate that the related emission measure predicted by the model is too high, which is a well known effect of 1-D hydrodynamic loop modeling (e.g. Warren & Winebarger 2006, 2007), and may point to the need for a more accurate description of the low loop atmosphere. This is however not required in this context. In the hot Fe XXIII line the opposite occurs, i.e. the brightness increases from the base to the top of the loop system, because the line is sensitive to plasma with  $\log T \geq 6.9$ , which is practically never found in the low part of the loop system. For our specific question, from the comparison of the first three lines we can immediately see that we can easily resolve the single loops in the cool line image, that this is more difficult in the second image, and that the Fe XV image is much more uniform and does not practically allow us to resolve substructures. Interestingly, the fourth image in the hot UV line shows again very well contrasted structures. This occurs also for the other hot lines, although with different levels of contrast. We will see that this predictions is confirmed in recent SDO/AIA observations. The plots in the right columns of Fig. 2.7 quantify better this effect: the profile along the cut in the cool line shows large fluctuations, with large amplitude and high spatial frequency, in the warm line profile the fluctuations are of smaller amplitude. According to the operative definition reported in Tripathi et al. (2009), the loop system in the Fe XV image is fuzzy, the loop system in the Mg VII image is not.

We have also devised a metric for fuzziness to be computed in the cross-section line:

$$\frac{\sigma_I}{\bar{I}} = \frac{1}{\bar{I}} \cdot \sqrt{\frac{1}{n} \sum_{i=1}^n (I_i - \bar{I})^2} \quad (2.11)$$

where  $I_i$  is the emission in the spectral line in the  $i$ -th pixel along the cross-section,  $\bar{I}$  is the average value for  $I_i$ , and  $n$  is the number of pixel in the region marked by the line (left panels in Fig. 2.7). This is a measure of the fractional root mean square fluctuaction of the emission along the cut. Clearly, the larger this quantity, the more contrasted and well resolved are the loops, and the smaller is the fuzziness. Table 2.1 includes the values of this metric for all the spectral lines analyzed. All these value are calculated along the same cut shown in Fig. 2.7.

The values are quite high for the lines at low temperatures ( $\log T \leq 6$ ; Mg VII, Si VII, Fe X), very high for the lines at very high temperature ( $\log T \geq 6.9$ ; e.g. S XV, Ca XIX, Fe XXIII, Fe XXV), lower for the warm lines (around 3 MK; especially FeXV, FeXVI, Ne IX). We have applied the same analysis changing numbers of strands in each pixel, and still find similar results.

The reason why the loop system appears more uniform at warm temperatures is clear

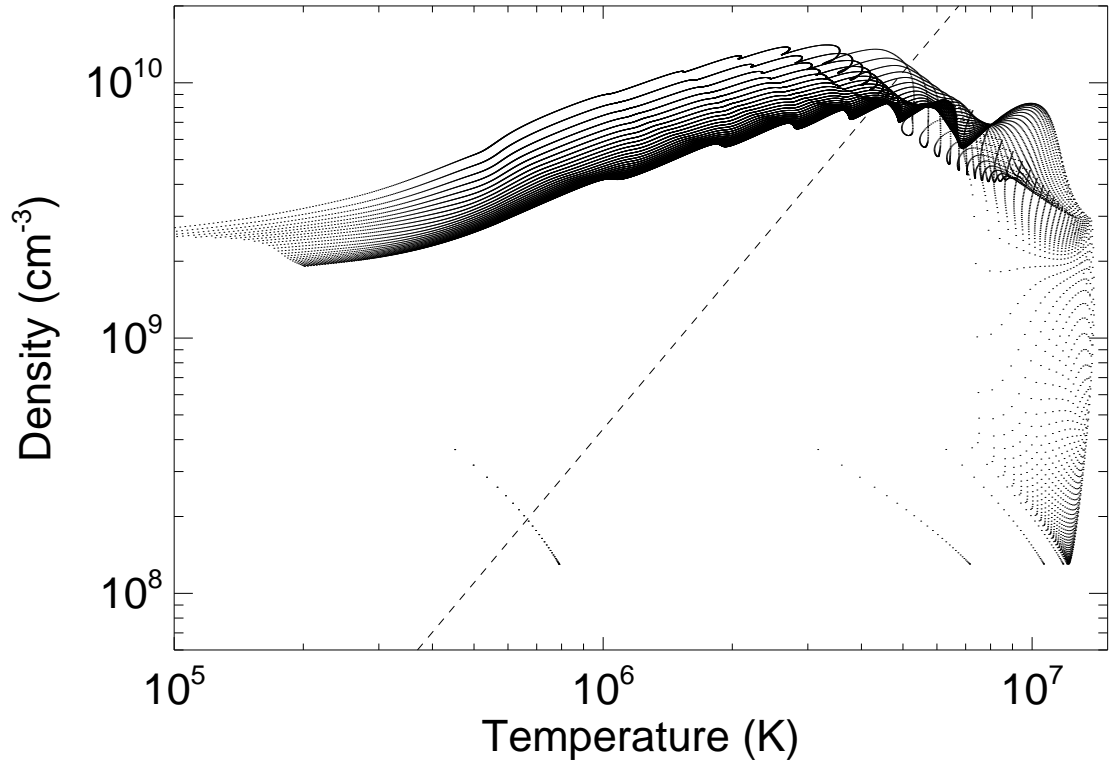


Figure 2.8 Scatter plot of the values of density and temperature, obtained from averaging on bins of 32 grid points in the whole model strand evolution (upper 90% part of the loops). The dashed line is the locus of density and temperature at the apex of hydrostatic loops, with half-length  $L = 3.0 \times 10^9$  cm, according to the scaling laws of Rosner et al. (1978).

Table 2.1 Variation of emission in the lines analyzed.

Line	Wavelength ( $\text{\AA}$ )	Emission temperature ( $\log T[K]$ )	$\sigma_I/\bar{I}$
Mg VII	278	5.8	0.28
Si VII	275	5.8	0.26
Fe X	186	6.0	0.23
Fe XII	195	6.1	0.22
Fe XIII	196	6.2	0.21
Fe XIV	264	6.3	0.20
Fe XV	284	6.4	0.18
Fe XVI	361	6.5	0.15
Ne IX	13.4	6.6	0.12
Mg XI	9.31	6.8	0.14
Fe XIX	133	6.9	0.26
Fe XX	133	7.0	0.39
Si XIII	6.69	7.0	0.21
Fe XXIII	133	7.1	0.55
S XV	5.10	7.2	0.30
Ca XIX	3.21	7.4	0.46
Fe XXV	1.87	7.6	1.0

from inspection of Fig. 2.8. In the figure each data point marks a value of density and temperature obtained from averaging over sections of 32 grid points along a strand (upper 90%) in each output. The figure clearly shows that around 3 MK the density of data points is higher, and at higher values of density. The implication is that each strand spends a long time, and with a high emission measure, at an average temperature of about 3 MK, and therefore at this temperature more strands appear on the average brighter, i.e. the loop system is more uniformly bright. The plasma does not stay long at a higher temperature, i.e. around the heat pulse, and moreover, during this phase, the emission measure is not high because the evaporation is still in an early phase. The plasma does instead stay for a long time at lower temperature, but the emission measure becomes very low, not contributing much to the overall emission. Fig. 2.8 also shows that this model fits well the observational constraint of alternating cool/overdense - hot/underdense status of coronal loops (e.g. Klimchuk 2006).

It is easy to imagine extrapolating this result to whole active regions, threaded with many thousands upon thousands of magnetic field lines. There are fewer field lines populated with low and high temperature plasma and so distinct loop structures appear. There are many more field lines populated with plasma in the 2 - 3 MK range and so fuzzy emission appearing to be composed of unresolved structures would arise as observed.

#### 2.2.4 SDO/AIA emission

We also synthesize the emission along each strand in some SDO/AIA filters: 335 Å, 171 Å, and 94 Å. The Solar Dynamic Observatory (SDO) mission provide us spectra and image of the sun since 2010. The Atmospheric Imaging Assembly (AIA) on board of SDO is an imaging instrument whose narrow passband filters contain several spectral lines emitted by plasma at different temperatures (see sec. 2.3.2). Particularly, the 335 Å filter has a peak at 3MK, 171 Å filter has a peak at 1MK, and 94 Å filter has a peak at 8MK (see Fig. 2.9 to have the dependence of emissivity from temperature in this three lines).

Figure 2.10 shows the loop emission synthesized from the hydrodynamic strand model in the 94 Å and 335 Å channels. Only the coronal part of the loop (upper 75% of the loop length) is shown. The loop is symmetric with respect the loop apex. Each strip is the average of a bundle of 60 strands. To emphasize the effect we are addressing, we normalize the emission in each pixel strip *across* the loop. From the comparison of the two images, we can immediately see many more white and black thin strips in the 94 Å image, while the other is more uniformly red.

The plots in panel (c) of Figure 2.10 are profiles along the cut in the upper figure (Figure 2.10 (a) and (b)). The 94 Å channel profile shows larger fluctuations than the 335 Å channel. (Figure 2.10 (a) and (b)). Again, we can use the root mean square of the intensity fluctuations (eq. 2.11) to quantify. We obtain  $\sigma_I/\bar{I} = 0.17$  for 94 Å channel, and

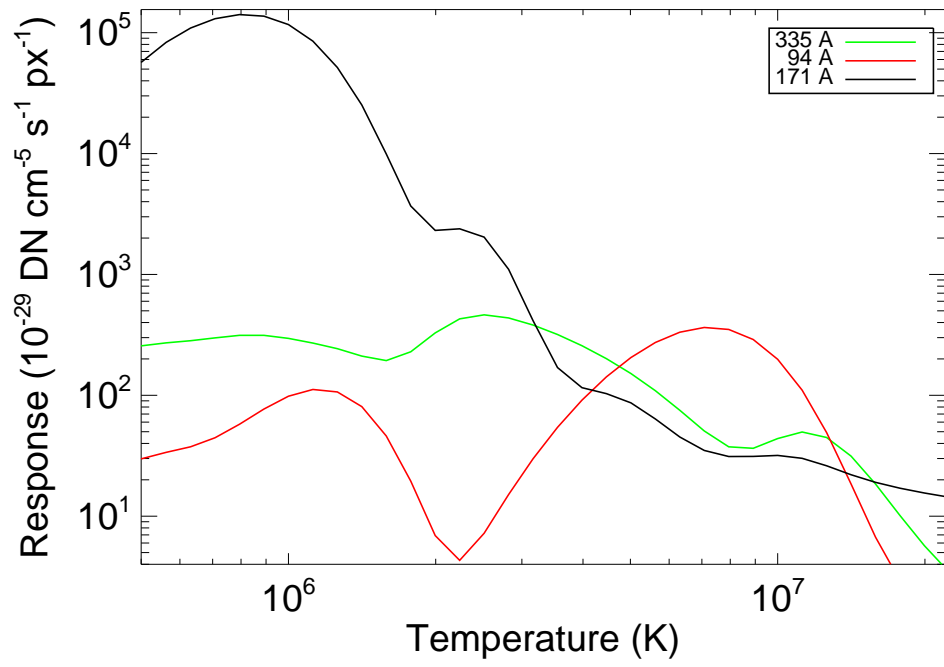


Figure 2.9 Emissivity per unit emission measure for 94 Å, 335 Å and 171 Å SDO/AIA channels vs  $T$ .



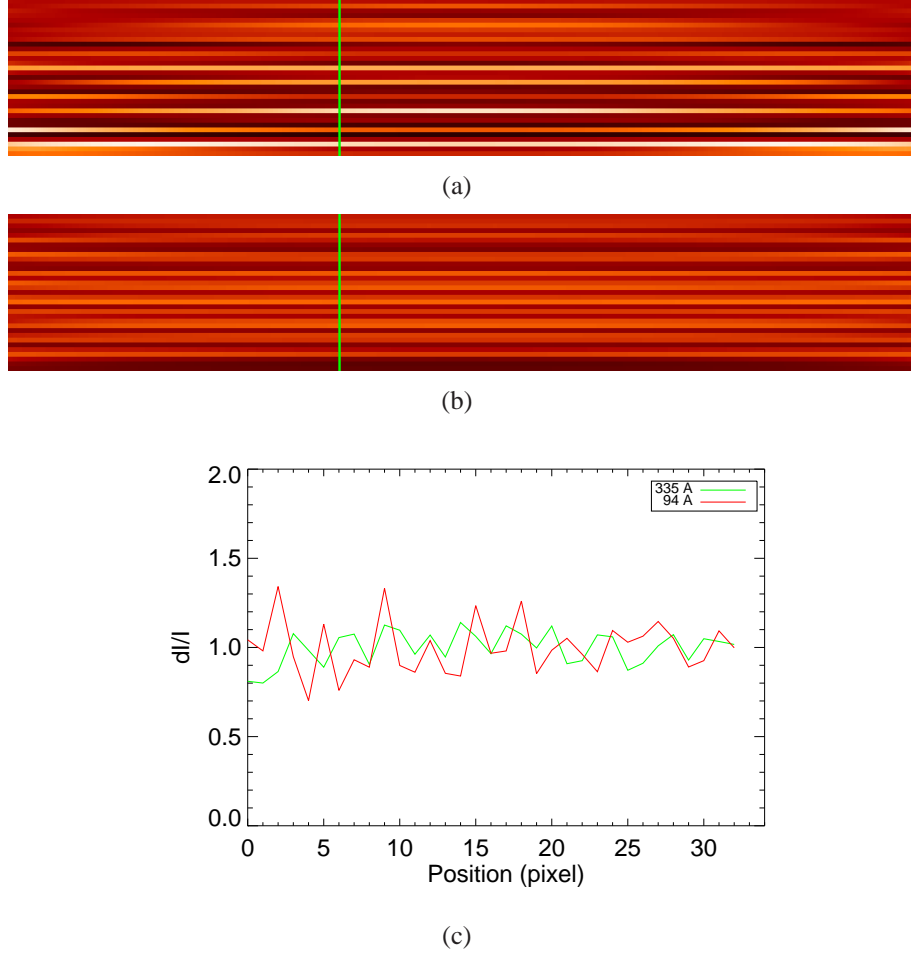


Figure 2.10 Emission of a straightened multi-stranded loop obtained from hydrodynamic modeling of a strand pulse-heated to 10 MK in the 94Å (a), and 335Å (b) SDO channels. Each strip is the average of a bundle of 60 strands. To emphasize the effect we are addressing, we normalize the emission in each pixel strip *across* the loop. In this color scale, white is the maximum of emission, and black the minimum (linear scale) spanning between 0.6 and 1.4 (average 1). Images (a) and (b) show the coronal part of the loop (upper 75% of the loop length). The loop is symmetric with respect the loop apex. (c) Cuts across the images (green lines). Red and green lines are related to the SDO 94Å and the 335Å channel, respectively.

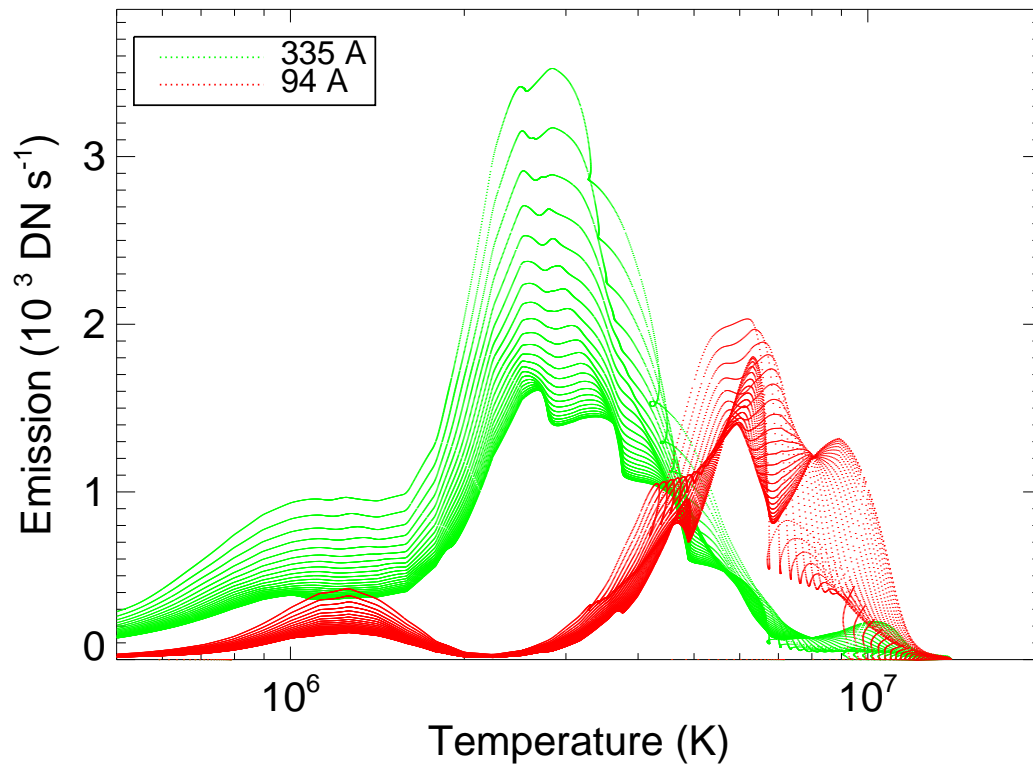


Figure 2.11 Scatter plot of the values of emission vs temperature obtained from hydrodynamic modeling of a strand pulse-heated to 10 MK. The values are averages over bins of 24 grid points at any time of the model strand evolution (upper 75% of the loops). Red and green points are related to the SDO 94 Å and the 335 Å channel, respectively. Bright 335 Å pixels contain mostly  $\sim 3$  MK plasma. The bright 94 Å pixels contain hotter plasma ( $\sim 6 - 8$  MK).

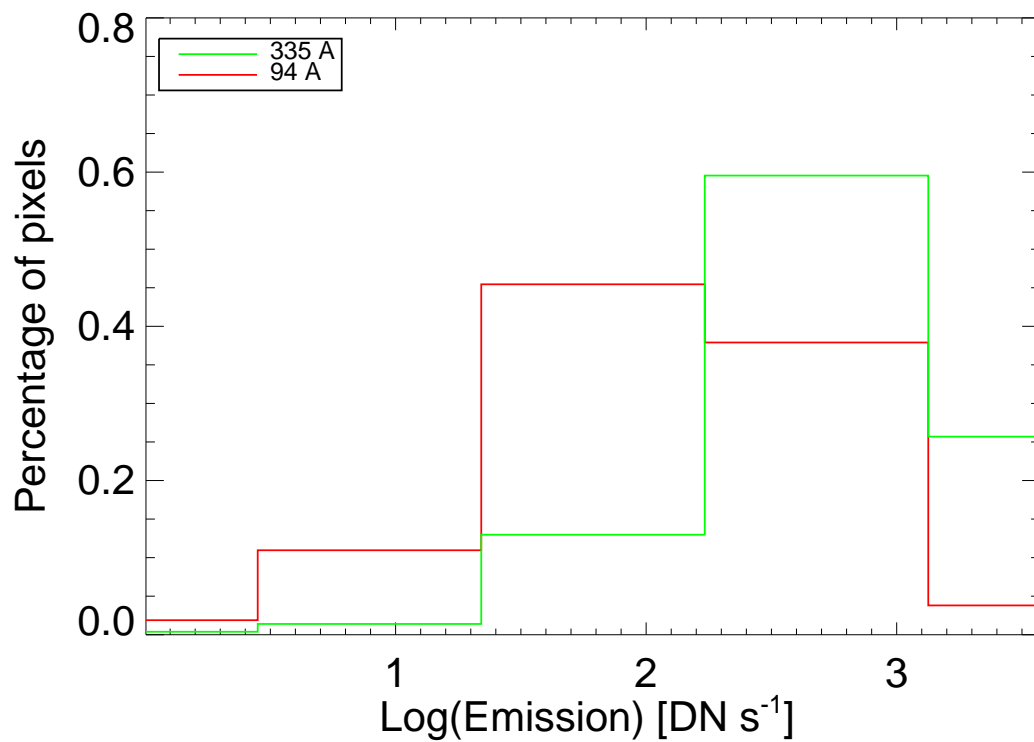


Figure 2.12 Distribution histogram of the values shown in Fig.2.11. Red lines refer to the 94 Å channel and green points to the 335 Å channel. Bright pixels are more numerous in the 335 Å channel.

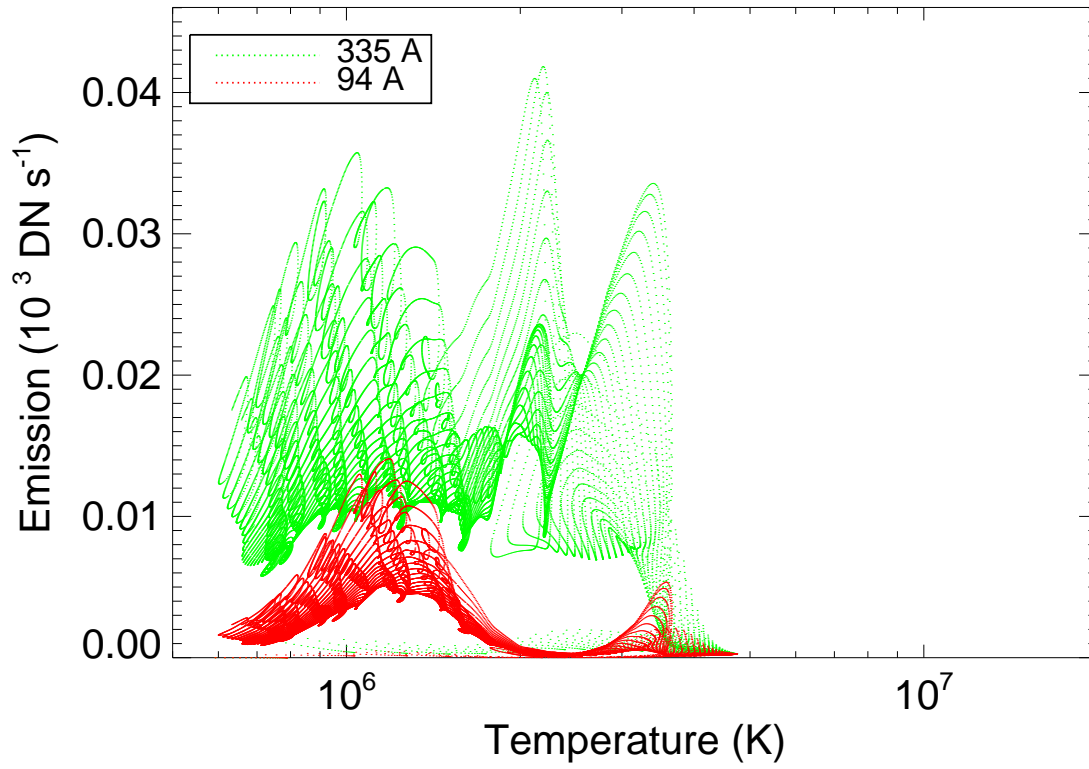


Figure 2.13 As Fig.2.11 for a strand model with less intense heat pulses which lead to a strand maximum temperature of about 4 MK.

$\sigma_I/\bar{I} = 0.09$  for 335 Å channel.

The reason why the loop system appears more uniform at 335 Å is clear from inspection of Figure 2.11 and 2.12. Figure 2.11 is a scatter plot of emission vs temperature values at each point along the strand and at each time of the simulation for both channels. To make the plot more readable each data point is an average over 24 grid points. The figure clearly shows that the brightest cells are around 3 MK and 6 - 8 MK in 335 Å and 94 Å channels respectively. Figure 2.12 is a histogram of Figure 2.11 showing that the fraction of bright cells is higher in the 335 Å channel than in the other channel. In other words, the emission is more uniformly bright in the 335 Å channel than in the 94 Å channel, which will show instead show more filamented bright structures, as observed. As explained before, the ultimate reason for this behavior is that overall each strand spends proportionally a long time, and with a high emission measure, at temperatures around 3 MK, i.e. just the temperature of maximum sensitivity of the 335 Å channel. Extrapolating this result to whole active regions, threaded with thousands of magnetic field lines, the loops will therefore be more populated by bright strands and appear more uniformly bright in this channel. On the contrary, they will appear less "filled" both in hotter and cooler channels.

This result is intimately connected to the pulsed nature of the assumed heating function. Some question are: is the pulsed nature the only required feature? Would we observe the same effect with heat pulses of any intensity? More specifically, would we observe the same effect also with less intense pulses and without heating plasma to about 10 MK? To answer these questions, we have repeated the same simulation with a energy input rate of  $H_0 = 0.01 \text{ erg cm}^{-3} \text{ s}^{-1}$  that heats the plasma up to only  $\sim 4$  MK.

In the steady-state the loop heating per unit of volume is therefore  $\bar{H} = H_0 \times 60/2000 \approx 0.0004 \text{ erg cm}^{-3} \text{ s}^{-1}$ . According to the scaling law (Rosner et al., 1978), this steady heating sustains a loop with an apex temperature of  $\approx 1.5 \text{ MK}$  corresponding to an average temperature of about 1 MK.

Figure 2.13 is the same scatter plot as Figure 2.11 for this cooler simulation. We see that, while the emission is spread at all temperatures in the 335Å channel, in the 94Å most of the bright emission comes from cells at about 1 MK. These would be very bright also in the 171Å channel but, as we will see in section 2.3, this is not the case.

Finally, we have synthesized steady-state pixel light curves from the model at 10 MK, shown in Fig. 2.14. The pixels are located in the central part of the loop. These will be compared directly to the observed ones in Fig. 2.16 and 2.20. The average root mean square variations in the 94Å and 335Å channel are around 16% and 8%, respectively. So this model predicts that the emission detected in 94Å channel varies with larger amplitude than in the 335Å channel. It is interesting to note that the grouping of the strands inside each pixel cancels out any signature of the heating and cooling of the single strands, i.e. we do not see clearly sequences of fast rises and slow decays. The only signature of cooling is that the average trend in the 335Å channel is similar to that in the 94Å channel

in some pixels, with a delay which might be associated with the progressive cooling of the plasma that makes it emit in different channels at different times. The 4 MK model shows average variations are 4% and 7% on average in the 335Å and 94Å channels respectively.

## 2.3 Experimental Evidence

The plasma inside coronal loops emits radiation mainly in the EUV and X energy band, with spectra depending on temperature. Hence, multiband and/or multiline observations are fundamental for the investigation of the thermal structure of the corona.

### 2.3.1 Comparison with Hinode/EIS Data

The Extreme-ultraviolet Imaging Spectrometer (EIS; Culhane 2007), on board of Hinode spacecraft (Kosugi et al., 2007), puts this evidence under a more quantitative and objective framework (Tripathi et al., 2009), discovering that the same active region structures are clearly discernible in cooler lines ( $\sim 1$  MK), and are fuzzy at a higher temperature ( $\sim 2 - 3$  MK), as it is shown in figure 2.1 (from Tripathi et al. 2009). As is evident from the figure, substructuring are more discernible in low-temperature lines than warm ones. This is perfectly in agreement with our model. From a simple visual inspection we see the same effect, in the same spectral lines of Tripathi et al. (2009).

### 2.3.2 Comparison with Solar Dynamic Observatory Data

Taking as a starting point the results obtained from section 2.2 we focus our attention on high temperature emission. Here we make a comparison of the emission predicted by our model with the emission observed with the Solar Dynamics Observatory (SDO). Here we show that the predictions are indeed widely confirmed in an active region with the SDO, and that therefore fine-structured energy pulses play a major role in heating the active corona.

#### The SDO/Atmospheric Imaging Assembly telescope

The Solar Dynamics Observatory (SDO) was launched in February 2010 and was designed to provide continuously spectra and images of the Sun in several wavebands and at very high cadence. The Atmospheric Imaging Assembly (AIA), with its 7 EUV narrow-band filters, images the solar corona with high spatial resolution ( $\sim 0.6$  arcsec/pixel), and high cadence in several spectral bands at the same time. SDO/AIA is able to image the corona in different filters whose narrow passbands contain different bright spectral lines emitted by plasma at different temperatures. In particular, the filters centered at 94Å and

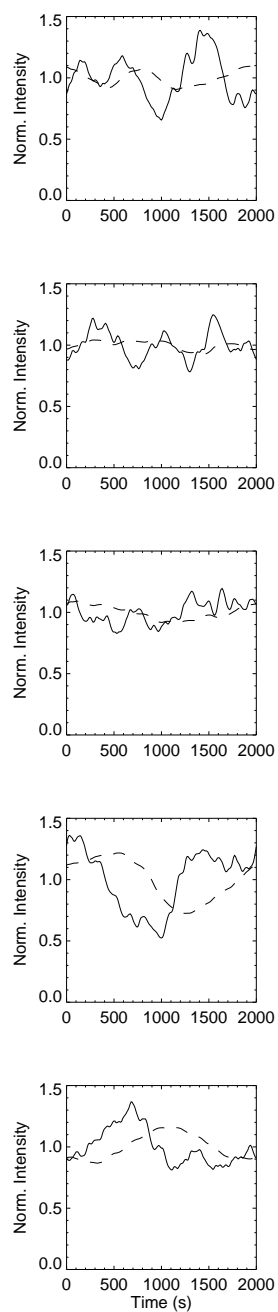


Figure 2.14 Light curves (*solid lines* 94 Å, *dashed lines* 335 Å) in five sample pixels obtained from the hydrodynamic simulation of multi-stranded pulse-heated loop. The intensities are normalized to the average emission in the pixel. The model light curves can be compared to the observed ones (Fig. 2.16 and 2.20).

335Å contain strong lines of FeXVIII and a Fe XVI line, respectively, which are emitted more efficiently by plasma around 8 MK and 3 MK, respectively (O'Dwyer et al. 2010).

Therefore, these two filters are appropriate to study the comparative presence of hot and structured plasma in coronal loops.

### Data Analysis

SDO/AIA observations of AR 11117 on October 28 2010, from 2:00 UT have been analyzed. Originally we consider an  $800 \times 600$  pixels region centered on the active region. An AIA pixel is 0.6 arcsec wide. We focused on observations obtained in three AIA EUV channels: 171 Å, 335 Å, 94 Å. Level 1.0 data have been used, obtained by standard processing of level 0 data which includes bad-pixel removal, despiking, and flat-fielding.

These data are obtained from a standard observing series with cadence of 12 s in all channels, and exposure times of 2 s in the 171 Å channel and 2.9 s in the 335 Å and 94 Å channels. The three chosen channels have very different sensitivity to the solar coronal emission (see Fig. 2.9), resulting in a very different typical signal-to-noise ratio in the channels. Therefore, for a more meaningful comparison of the morphology of active region loops in the different channels, and avoid possible spurious effects due to the different noise level, few images in the lower intensity channels (335 Å, and, especially, 94 Å) has been summed.

First the series of images in each channel have been coaligned by using a standard routine (`tr_get_disp.pro`) available in SolarSoftware analysis package of IDL which uses cross-correlation of the images. Then we added 30 consecutive images in the 94 Å channel, and 3 consecutive images for the 335 Å channel. Resulting images in 94Å and 335Å channels are co-aligned with a cross-correlation technique.

For the moment, let's focus the attention to the top two images of figure 2.15, and, in particular, to the core of the active region (Fig 2.17).

We note that during the corresponding time interval ( $\leq 3$  min) the variability is of a few percent at most (Fig. 2.16).

In the 335Å channel, the core is surrounded by a halo of fainter and larger arches (marked with LL), which concentrically depart from two poles located at the east and west of the core of the active region. In the 94Å channel, the large arches around the core are fainter and hardly visible, making the appearance of the region less diffuse. In the 171 Å channel, giant arches (marked with OL) depart from the two magnetic poles, but mostly in the outbound east-west direction. The bright moss extends from the core also to the north-east.

In the 335Å channel, overall the region has quite a diffuse appearance and individual loops cannot be clearly resolved.

In the 94Å channel, overall we see a very similar morphology and many bright structures are clearly cospatial with those observed in the 335Å filter. The most striking difference from the image in the other filter is in the core itself: in the southern part, whereas



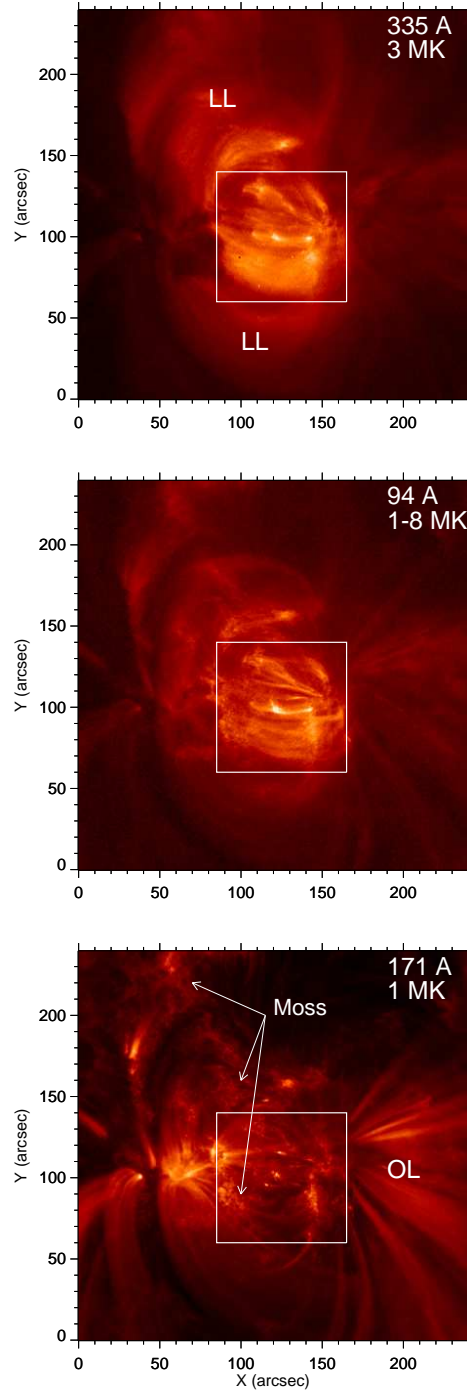


Figure 2.15 Active region AR 11117 observed in 3 different filters (94 Å, 335 Å, 171 Å) of the SDO/AIA on 27 October 2010 around 01 UT. The filters are most sensitive to plasma emitting at the labeled temperatures. The subregion shown in Fig.1 in the main text is marked (box). Large-scale loops (LL) are marked outside of the boxes in the 335Å image. In the 171 Å we indicate moss regions and outbound loops (OL).

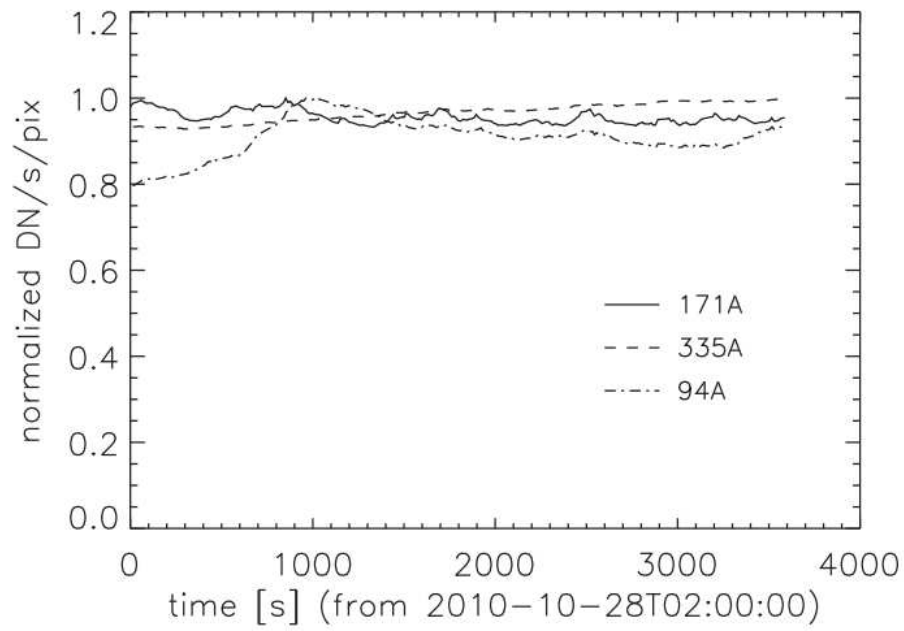


Figure 2.16 Normalized lightcurves derived in the three channels over a period of 1 hr (from 02 : 00 : 00 to 03 : 00 : 00), and integrating the signal in the active region core (in a region of 100 pix X 110 pix).

in the 335Å channel the arches are densely packed and uniform, here they are much more contrasted, i.e. we see an alternation of bright and fainter structures whereas the arches were so many that they formed a single bright strip in the 335Å band (between  $Y \approx 10$  and  $Y \approx 45$  arcsec), here they are much more contrasted, i.e. we see an alternation of bright and less bright structures.

In the northern part, we are even able to resolve very thin bright east-to-west bridges, in the same location where thicker arches are present in the softer filter. Overall, in the 94Å channel, the loop systems appear sharper, the observed emission largely less “fuzzy”, and we can resolve thinner bright structures than in the 335Å channel. We show the inner part of the active region in Fig. 2.17. This is exactly the effect that we expected, and that was predicted (section 2.2.4 and Guarrasi et al. 2010).

We have however to be cautious in one important point. Although the filter passbands are narrow, they include several spectral lines. In particular, the 94Å channel includes another strong line (Fe X) which peaks at around 1 MK. In general, we cannot, therefore, be sure that the emission imaged by this channel is emitted only by hot plasma ( $\gtrsim 6$  MK). The 171Å image helps us in this respect, because it allows us to localize the bright cooler plasma ( $T \sim 1$  MK), and to indicate whether the 94Å emission is due to hot or warm plasma. In the 171Å channel the active region shows quite a different morphology. Many structures are complementary to those observed in the other channels (Reale et al., 2007). The core appears depleted of arch-like structures. Only a very few of them are visible, and they look very different from those in the other two filters, which instead look overall very similar to each other. The arch-like structures are instead replaced by bright “moss”. This moss is a very well-known feature of this soft channel, already studied in NIXT and TRACE observations and commonly explained as the bright warm footpoints of hot high-pressure loops (Peres et al., 1994; Fletcher & de Pontieu, 1999; Martens et al., 2000). The 171Å image clearly indicates that the plasma confined in the filamented arches that we see in the 94Å filter is not warm at 1 MK, and therefore it must be hot around 6 - 8 MK.

However we also made the conservative assumptions that the cool plasma temperature is the one of the peak of the cool 94Å response component (Fig. 2.9), i.e.  $\log T = 6.05$ , and that the cool 94Å response component is underestimated by a factor 5 (Aschwanden & Boerner, 2011). This estimated cool 94Å map have been subtracted from the 94Å map shown in Fig. 2.17. The resulting image is also shown in Fig. 2.17(bottom). We note that the moss emission visible in the 94Å channel is considerably reduced, and that the loop footpoints regions and the outbound loops are mostly removed. On the other hand, the emission of the loop bundle in the central region does not change significantly, except for a reduction in the moss region, and the fine structures in the upper half of the image are also almost unchanged. This confirms that the emission of the loop bundle and of the fine structures mostly comes from hot plasma.

Figure 2.18 plots the emission, divided by the values derived with a moving average, along the vertical and horizontal lines marked in Figure 2.17, which provides a quantita-

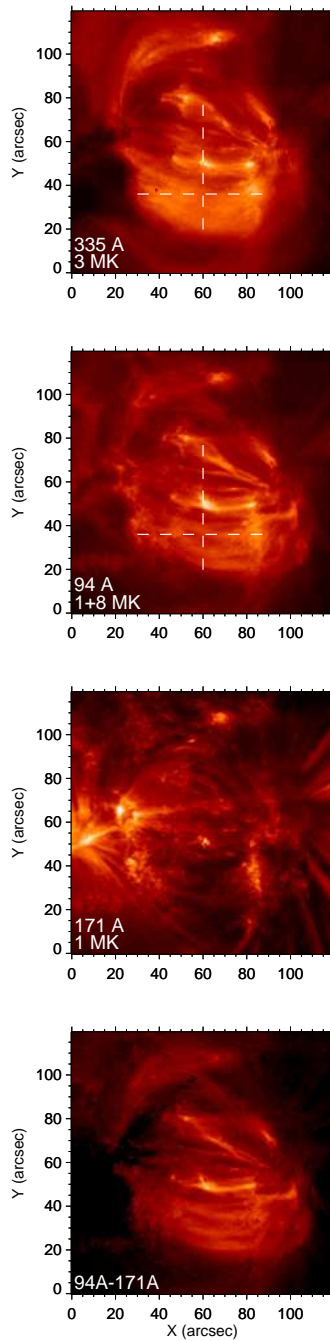


Figure 2.17 Inner part of the active region AR11117 observed in 3 different channels (335Å, 94Å, 171Å) of the SDO/AIA on 27 October 2010 around 02 UT. The color scales as the square root of the pixel counts. The ranges are 59–1567, 55–3157, 155–4681 DN for the three channels, respectively. The channels are most sensitive to plasma emitting at the labeled temperatures. The bottom panel shows the image obtained by subtracting the cool component scaled from the 171Å channel to the 94Å image (same color scale as second panel, real range 0–2741 DN). Fig. 2.18 shows brightness profiles along the marked vertical and horizontal lines.

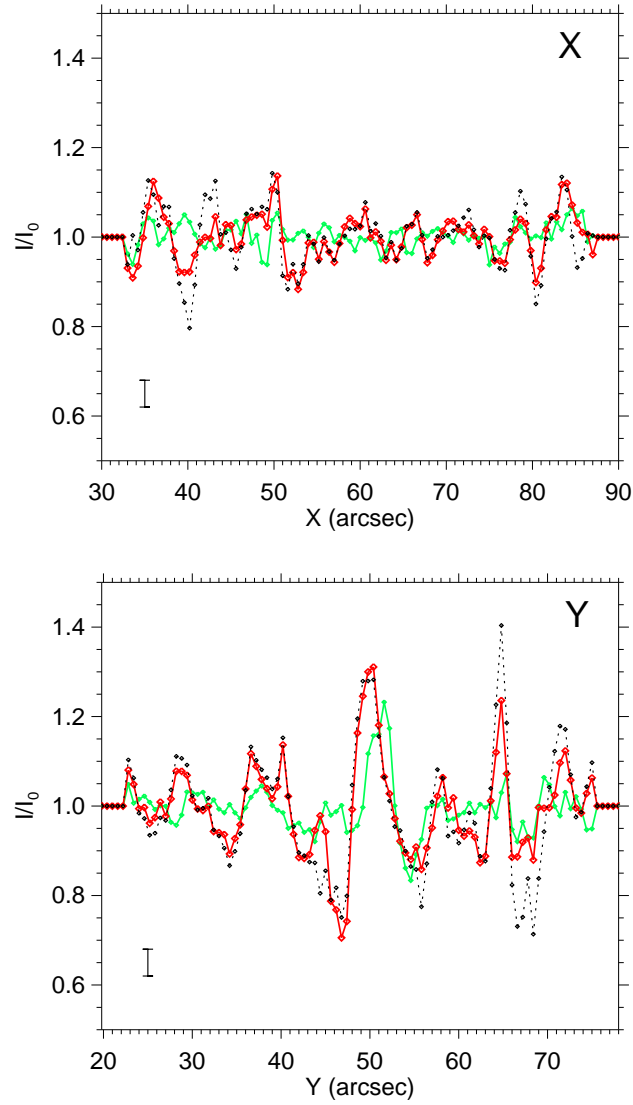


Figure 2.18 Brightness profiles in the 94Å before (red) and after (black dotted) subtracting the cool 1 MK component, and in the 335Å (green) channels along the horizontal (a) and vertical (b) lines in Fig. 2.17. The profiles are normalized to a moving average with a 10 pixels boxcar. A typical error bar is also shown.

Table 2.2. Fractional RMS amplitude excursions

Region	335Å X	$\sigma$	94Å X	$\sigma$	335Å Y	$\sigma$	94Å Y	$\sigma$
Single row/column	0.03	...	0.05	...	0.06	...	0.10	...
Region little moss (size: $60 \times 60$ pixels, center: $[X = 58'', Y = 38'']$ )	0.032	0.017	0.046	0.021	0.052	0.011	0.082	0.017
Central core region ( $70 \times 70$ , $[68'', 49'']$ )	0.044	0.018	0.059	0.021	0.072	0.016	0.111	0.036
Central core region (94Å–171Å)	0.044	0.018	0.068	0.025	0.072	0.016	0.130	0.037
Whole core region ( $100 \times 100$ , $[72'', 48'']$ )	0.053	0.021	0.065	0.021	0.063	0.011	0.099	0.020

Note. — The first row is computed along the lines marked in Fig. 2.17.  $\sigma$  is the standard deviation of the rms excursions.

tive estimate of the different fuzziness of the hot ( $\gtrsim 6$  MK) and cooler ( $\sim 3$  MK) plasma.

Along the horizontal line – which runs approximately along the magnetic tubes – the pixel brightness changes in a similar way and with a similar amplitude in the 335Å and 94Å channels. The root mean square average of the amplitude excursion is  $\approx 6\%$  and  $\approx 7\%$ , respectively. These might be taken also as upper limits of the photon noise.

Along the vertical line - which runs *across* the field line direction – the brightness in the 94Å channel shows significantly more pronounced spatial variability than the corresponding emission in the 335Å channel, and the root mean square average of the amplitude excursion becomes 12% vs 7%.

To check on larger baselines, we derived the analogous values over all the rows (X) and columns (Y) of selected regions. For each region, Table 2.2 shows the RMS average values, and their standard deviations, in both channels. Three regions have been selected: one with as little moss as possible, the very center, and a larger core region. For the second region, we also report the values obtained in the 94Å channel after subtracting the cool component. We find that the Y-values in the 94Å channel are invariably much higher than all the others, thus confirming that the decrease of fuzziness in the 94Å channel is highly significant.

### Fourier Analysis

In the previous section we have shown that in the inner active region we see a finer structuring in the 94Å than in the 335Å channel. To add support to this evidence, the 2-D Fast Fourier Transforms (FFT) of the images of Fig. 2.17 in the 94Å channel before and after subtracting the cool component and in the 335Å channel has been taken. Then we sum along circles of constant wavenumber, as it was done in the past for NIXT observations (Gomez et al., 1993a,b). The power at zero wavenumber reflects the mean intensity of the image, so we normalize the images by the average intensity to make cross comparison of the power distributions more straightforward. In Figure 2.19 the resulting Fourier

transforms are power-laws. We see that both 94Å FFTs are systematically higher than the 335Å FFT in the wavenumber range  $\sim 10 - 70$ , that corresponds to a spatial range  $\sim 14 - 2$  pixels. This range is in agreement with the cross-section size of the observed structures. All the lines converge at the highest wavenumbers, which are related to the presence of noise. This indicates a similar signal-to-noise ratio for both channels. In the end, the figure confirms more power at relatively high wavenumbers in the 94Å channel both with and without subtracting the 1 MK component.

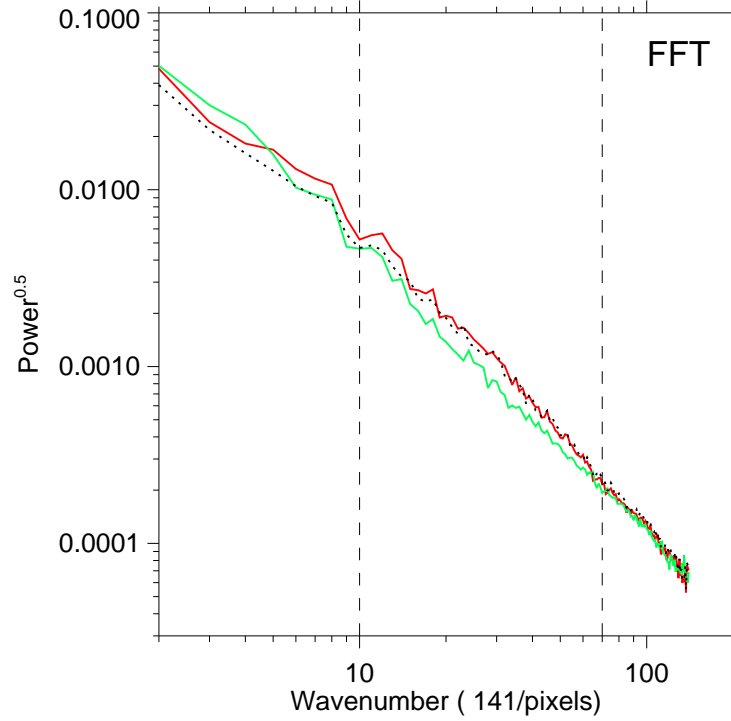


Figure 2.19 Normalized 2-D Fourier Transforms of 335Å and both 94Å images in Fig. 2.17. 94Å transforms are both systematically higher than the 335Å transform in the wavenumber range between the dashed lines.

### Light Curves

Normalized light curves derived in the three channels over a period of 1 hr (from 02:00:00 to 03:00:00), and integrating the signal in the active region core (in a region of  $100 \text{ pix} \times 110 \text{ pix}$ ) are shown in Fig. 2.16. The curves indicate an overall low level of variability of the EUV emission in the core of this active region, to a level of  $\leq 20\%$ , over the wide temperature range observed in the three AIA channels. In the case of loops consisting of unresolved pulse-heated strands, we would expect that in the 94 Å channel the emission

were more variable, i.e. subject to larger fluctuations, than in the 335 Å channel, basically for the same reason why we see finer structuring in the former than in the latter channel. Figure 2.20 shows the light curves in five sample pixels in the region of the bright thin structures in the 94 Å channel (X 60, Y 60 in Fig. 2.17). To minimize the effect of different photon statistics, we have applied a boxcar of 10 frames and normalized to the average DN rate. The light curves clearly show that, the 94Å channel emission is more variable than the 335 Å channel emission, as expected. To be more quantitative, the average root mean square variations in the 94Å and 335Å channel are around 14% and 7%, respectively. This can be compared with the results obtained in section 2.2.4. The simulated data are very similar to the observed ones.

## 2.4 Discussion

We investigate a model of substructured lonely coronal loop, consisting of a multitude of thin strands each heated by a short and intense energy pulse. Here, our testing ground of this model is the evidence of increasing fuzziness of the emission of the loop system with temperature of emitting plasma, and therefore of maximum instrument sensitivity.

Our basic scenario is that coronal loops consist of bundles of thin strands, each of thickness below the instrumental spatial resolution, and that each strand is heated up to about 10 MK by a strong and fast heat pulse, i.e. the loops are heated by a storm of nanoflares. The plasma is confined in each strand, so that it evolves as an independent atmosphere, and can be modeled with loop hydrodynamics (see also Patsourakos & Klimchuk (2007) for a conceptually similar approach). Our choice has been to assume that the strands are all heated once and by the same heat pulse, lasting 60 s, occurring at a different random time for each strand, with a cadence and an intensity adequate to maintain the loop at  $\sim 3$  MK on average, and to reach local strand temperature  $\sim 10$  MK<sup>1</sup>. This model fits well the observational constraint of hot/underdense-cool/overdense cycles. We have then collected 2000 different strands to form a loop system, and derived synthetic images of the loop system when it reaches steady state in several relevant spectral lines. In our opinion, the images synthesized from our model unequivocally show the same “fuzziness” in the same warm lines as observed with EIS, and the same better definition in the cool lines as observed with EIS. In other words, our model is able to explain the evidence. Of course, it explains also the effect as observed in narrow-band XUV instruments such as the normal-incidence imaging telescopes, TRACE and SoHO/EIT. We have also provided quantitative figures to this effect. The basic reason why this model works is that, in spite of the short heat pulse, the strands spend a long time with a high emission measure at a temperature around 3 MK, much less time when plasma is hotter and long time, but with

---

<sup>1</sup>Small variations in duration and amplitude of the heat pulses don’t affect significantly the results of the simulations. The only important constraints are that the loop system has an average temperature  $\sim 3$  MK and that the maximum temperature of each strand is  $\sim 10$  MK.



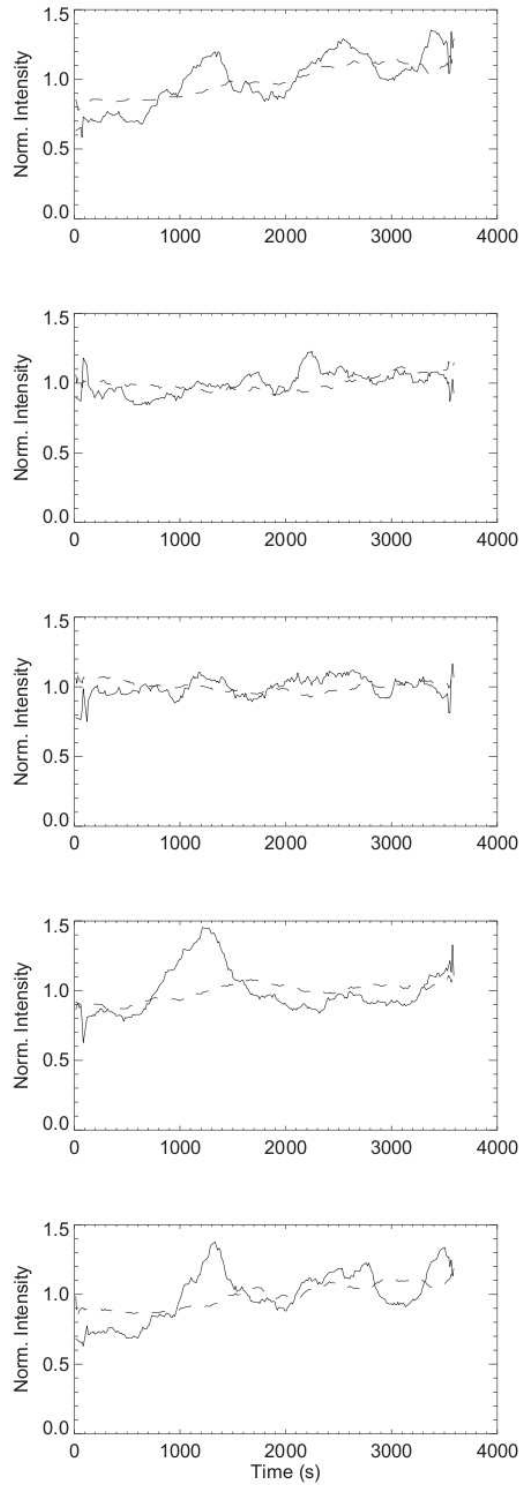


Figure 2.20 Light curves (solid lines 94 Å, dashed lines 335 Å) in five sample pixels in the region of the bright thin structures in the 94 Å channel (X 60, Y 60 in new Fig. 2.17). The intensities are normalized to the average DN rate.

much less emission measure when the plasma is cooler.

So the loop systems appear more uniform around 3 MK, and this higher filling factor gives the impression of “fuzziness”, as described in Tripathi et al. (2009). In cooler lines we are able to resolve better the loops, which appear more contrasted and with better defined boundaries.

This “fuzziness” is different from the one intended in Sakamoto et al. (2009): we address the question why the same loops appear different in different lines, which is exactly the evidence reported in Tripathi et al. (2009), whereas Sakamoto et al. (2009) address the evidence that hot loops appear fuzzier than cooler, not co-spatial, and therefore different, loops.

Our analysis provides also an interesting prediction: we expect high contrast to show in very hot lines, such as the Fe XXIII line and the Ca XIX line (typical flare lines), even stronger than in the cool lines.

We have been able to verify this prediction on a recent observation with the Solar Dynamics Observatory. In particular we have ascertained that the active region core appears more fuzzy in the 335 Å channel ( $\sim 3$  MK) than in the 94 Å channel ( $\sim 6 - 8$  MK). This largely confirm the prediction of our model, i.e. that there is widespread extensive hot plasma in active regions and that hot active region plasma is very finely structured, as expected in our scenario where storms of intense and rapid energy pulses are heating the coronal loops, one for each strand. Such strands are temporarily superhot up to flare temperatures. We remark that in the 94Å channel we are not resolving the individual strands. We instead still see bundles of strands and the brightest ones are those where the fraction of very hot strands is relatively larger. The reason why these superhot components are so difficult to detect is their small emission measure, and their small duty cycle with respect to most of their evolution time, spent mostly for the subsequent long cooling phase. This result confirms previous debated analyses (Reale et al., 2009b,a; Schmelz et al., 2009; McTiernan, 2009; Sylwester et al., 2010), is consistent with many other pieces of evidence pointing to dynamically heated loops, e.g. overdensity of  $\sim 1$  MK loops (Klimchuk, 2006; Reale, 2010), and indicates that localized heat pulses, e.g., nanoflares, play a major role in powering coronal active regions.

Desirable future X-ray spectral observations of the quiet Sun, and in particular of active regions, at high sensitivity and enough spatial resolution, may provide an important confirmation of our scenario.

There are several limitations in our approach. Small duration heat pulses are a necessary ingredient to have a multi-temperature loop system. Here we assume that the heat pulses are the same in all strands, only their timing is different, and that, at regime, they occur with a constant time average. We expect some broadness in the distribution of the heat pulses, in duration, intensity and average cadence. Other simplifications concern other assumptions on the heat pulses. We are assuming a very simple time-shape of the heat pulse, with abrupt on and off. This should not affect the results, because we analyze

the strands evolution on a much longer time scale. The heat pulse is long enough not to have significative effects due to delay to reach equilibrium of ionization (Reale & Orlando, 2008). We also assume that each strand is heated only once, i.e. there is no reheating of the same strand. This is a realistic assumption in the framework of progressive magnetic reconnection occurring in gradually twisting loops, due to footpoint photospheric motions. Presumably there can only be one heating event per strand since it is destroyed after magnetic reconnection. Nevertheless, note that the reconnecting strands form two new (relaxed) strands which are then presumably subject to the same twisting/braiding motions which originally energised them, leading to eventual reconnection and another heating event. In principle, this process could be repeated many times for a single pair of strands. The magnetic flux in this case is not destroyed, simply reconfigured.

The hydrodynamic description of the confined plasma should hold quite firmly in the individual loop strands, as in monolithic loops. Maybe the description of the low loop section should, for instance, include the possible tapering in the transition region (e.g. Gabriel 1976), but differences are expected only in the very low part of the loops and, therefore, should not affect the results presented here.

## **Chapter 3**

# **MagnetoHydroDynamics Modeling of Coronal Loops**

Indeed, 1D models can include the description of loops expanding in the transition region, through a height-dependent area factor in the terms containing the divergence operator. However, this factor defines a fixed geometry of the system and therefore cannot account for variations of the loop cross-section due to the evolution of the confined plasma. In particular we expect the thin transition region to move up and down along the loop due to the plasma dynamics and heating. This shift drives also variations of the loop cross-section because of the local time-dependent deformation of the confining magnetic field. To treat this interaction conveniently, a proper and fully MHD description is required.

In this chapter I'll present a 2D-MHD loop model that naturally accounts for loop expansion through the transition region. We have used this model to study the plasma response to the heating into and around the moss regions.

In this chapter I'll first describe our model, the equations that the model itself solves, and the code in which the model is implemented.

Then I'll illustrate its first application to study how the heating and dynamics of the plasma influences the loop expansion. I'll show the boundary condition used in our model, and how we obtain the initial magnetic field configuration. Then we show the parameter used in our simulation, and in particular the heating function used to slowly heat our loop to typical coronal temperatures.

Finally I'll show the first results obtained from our model, and discuss about it.

### 3.1 The Model

We address a coronal loop as a magnetic flux tube which confined coronal plasma. In a schematic view, a loop can be seen as a plasma confined in a magnetic tube anchored to two dense and cool chromospheres. So our approach is to describe the loop with a one-direction magnetic field linking two dense plane-parallel chromospheres. In this description, the loop is straightened in a vertical flux tube, but we put in it a gravity proper of a curved flux tube. We consider a two-dimensional description, and the total geometric domain is almost square. The proper loop forms as soon as we put a heating excess in the central region and not elsewhere. This is due to the fact that the heating is transported along the magnetic field lines and makes plasma expand from the chromospheres upwards, filling the space between the footpoints in the central region.

Our model considers the time-dependent MHD equations in a 2D Cartesian coordinate system including the gravitational force (for a curved loop), the thermal conduction (including the effects of heat flux saturation), the coronal heating (via a phenomenological term), and radiative losses from optically thin plasma. In Sec. 3.1.1 we will show the equations of our model, and in Sec 3.1.2 we will describe the code used to solve them numerically.

#### 3.1.1 The Equations

In our model the equations that we solve numerically are the time-dependent ideal MHD equations written in non-dimensional conservative form:

$$\frac{\partial \rho}{\partial t} + \nabla \cdot (\rho \mathbf{u}) = 0 \quad (3.1)$$

$$\frac{\partial \rho \mathbf{u}}{\partial t} + \nabla \cdot (\rho \mathbf{u} \mathbf{u} - \mathbf{B} \mathbf{B} + \mathbf{I} P_t) = \rho \mathbf{g} \quad (3.2)$$

$$\frac{\partial \rho E}{\partial t} + \nabla \cdot [\mathbf{u} (\rho E + P_t) - \mathbf{B} (\mathbf{v} \cdot \mathbf{B})] = \rho \mathbf{u} \cdot \mathbf{g} - \nabla \cdot \mathbf{F}_e - n_e n_H \Lambda(T) + Q(x, y, z, t) \quad (3.3)$$

$$\frac{\partial \rho \mathbf{B}}{\partial t} + \nabla \cdot (\mathbf{u} \mathbf{B} - \mathbf{B} \mathbf{u}) = \rho \mathbf{g} \quad (3.4)$$

$$\nabla \cdot \mathbf{B} = 0 \quad (3.5)$$

where:

$$P_t = p + \frac{\mathbf{B} \cdot \mathbf{B}}{2} \quad (3.6)$$

$$E = \epsilon + \frac{\mathbf{u} \cdot \mathbf{u}}{2} + \frac{\mathbf{B} \cdot \mathbf{B}}{2\rho} \quad (3.7)$$

$$\mathbf{F}_c = \frac{F_{sat}}{F_{sat} + |\mathbf{F}_{class}|} \mathbf{F}_{class} \quad (3.8)$$

$$\mathbf{F}_{class} = k_{\parallel} \hat{\mathbf{b}} (\hat{\mathbf{b}} \cdot \nabla T) + k_{\perp} [\nabla T - \hat{\mathbf{b}} (\hat{\mathbf{b}} \cdot \nabla T)] \quad (3.9)$$

$$|\mathbf{F}_{class}| = \sqrt{(\hat{\mathbf{b}} \cdot \nabla T)^2 (k_{\parallel}^2 - k_{\perp}^2) + k_{\perp}^2 \nabla T^2} \quad (3.10)$$

$$F_{sat} = \phi K_{sat} n_e c_{iso}^3 \quad (3.11)$$

are the total pressure, and total energy per unit of mass (internal energy  $\epsilon$ , kinetic energy, and magnetic energy) respectively,  $t$  is the time,  $\rho = \mu m_H n_H$  is the mass density,  $\mu = 1.265$  is the mean atomic mass (assuming metal abundance of solar values; Anders & Grevesse 1989),  $m_H$  is the mass of hydrogen atom,  $n_H$  is the hydrogen number density,  $\mathbf{u}$  is the plasma velocity,  $\mathbf{g}$  is the gravity acceleration vector for a curved loop,  $\mathbf{I}$  is the identity versor,  $T$  is the temperature,  $\mathbf{F}_c$  is the thermal conductive flux (see eq. 3.8, 3.9, 3.10, 3.11),  $\Lambda(T)$  represents the optically thin radiative losses per unit emission measure derived from CHIANTI v. 7.0 database (E. Landi private communication, Dere et al. 1997; Young et al. 2003; see Fig. 3.1) assuming coronal metal abundances (Feldman 1992), and  $Q(x, y, z, t)$  is a function of space and time describing the phenomenological heating rate (see Sect.3.2.2). We use the ideal gas law,  $P = (\gamma - 1)\rho\epsilon$ . The viscosity and the resistivity are assumed to be negligible.

### 3.1.2 The Code

The calculation are performed using the PLUTO code (Mignone et al., 2007, 2011), a modular, Godunov-type code for astrophysical plasmas.

The code provides a multiphysics, algorithmic modular environment particularly oriented toward the treatment of astrophysical flows in the presence of discontinuities as in the case treated here. The code was designed to make efficient use of massive parallel computers using the message-passing interface (MPI) library for interprocessor communications. The MHD equations are solved using the MHD module available in PLUTO, configured to compute intercell fluxes with the Harten-Lax-Van Leer approximate Riemann solver, while second order in time is achieved using a Runge-Kutta scheme. A Van Leer limiter for the primitive variables is used. The evolution of the magnetic field is carried out adopting the constrained transport approach (Balsara & Spicer, 1999) that maintains the solenoidal condition ( $\nabla \cdot \mathbf{B} = 0$ ) at machine accuracy.

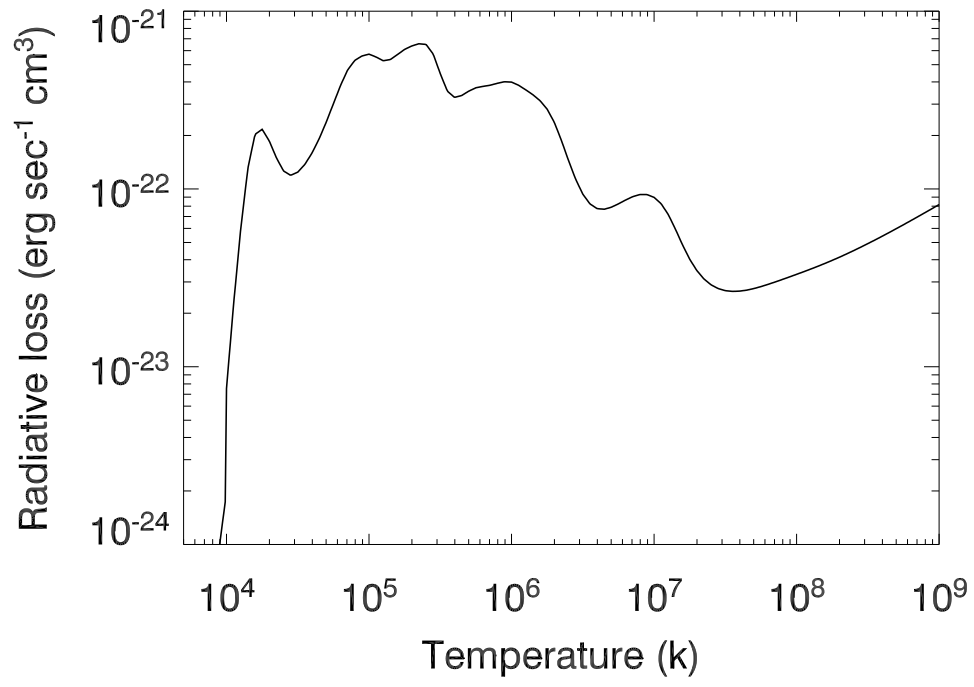


Figure 3.1 The radiative loss  $\Lambda(T)$  from E. Landi private communication.



PLUTO includes optically thin radiative losses in a fractional step formalism (Mignone et al., 2007), which preserves the 2nd time accuracy, as the advection and source steps are at least of the 2<sup>nd</sup> order accurate; the radiative losses  $\Lambda$  values are computed at the temperature of interest using a table lookup/interpolation method. The thermal conduction is treated separately from advection terms through operator splitting. In particular we adopted the super-time-stepping technique (Balsara & Spicer, 1999) which has been proved to be very effective to speed up explicit time-stepping schemes for parabolic problems. This approach is crucial when high values of plasma temperature are reached (as during flares), explicit scheme being subject to a rather restrictive stability condition (i.e.  $\Delta t \leq (\Delta x)^2 / 2\eta$  where  $\eta$  is the maximum diffusion coefficient), as the thermal conduction timescale  $\tau_{cond}$  is shorter than the dynamical one  $\tau_{dyn}$  (e.g. Orlando et al. 2005, 2008).

## 3.2 Heating in Variable Section-Coronal Loops

We focus our attention on the detailed modeling of the effect of the loop plasma evolution on the confining magnetic field. We focus on the region including and around a single loop, and therefore our approach is complementary to large scale modeling (e.g. Carlsson et al. 2010; Bingert & Peter 2011; Martínez-Sykora et al. 2011a,b).

Our model describes a loop using a plane-parallel geometry. As we can see from Fig. 3.2 we took a longitudinal cross section of straightened loop, however using the typical gravity for a curved loop.

We address a typical active region loop. So, our loop has a half length about  $3 \times 10^9$  cm and a maximum temperature about  $3 \times 10^6$  K. To include this loop we consider a computational domain (see Fig. 3.3a) from  $-3.5 \times 10^9$  cm to  $3.5 \times 10^9$  cm on y direction (i.e along the loop direction), and from  $-4 \times 10^9$  cm to  $4 \times 10^9$  cm on x direction (i.e across the loop).

We need a resolution high enough (about  $(2 - 4) \times 10^6$  cm) appropriately to resolve the transition region. However higher resolution requires smaller timestep in numerical integration, because the timestep decreases with the square of the minimum space step, and therefore the total computational time can become unaffordable. Our choice has been to use a non-uniform grid with a uniform grid size tuned to the available computational resources. Fig. 3.3b shows the pixel size as a function of the position. We have the maximum resolution near the transition region ( $|y| \approx 3 \times 10^9$  cm) and in the central part of the loop ( $x \approx 0$  cm).

### 3.2.1 Initial and Boundary Conditions

As a first task, we have to build the proper loop topology ready for the injection of heating. Particularly, we are interested in having a strong expansion of the magnetic field lines near the transition region. On the other hand, our magnetic field configuration must satisfy the

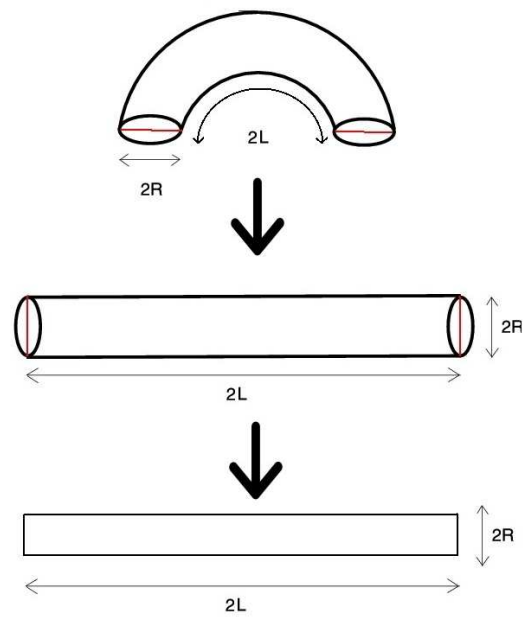


Figure 3.2 Flowchart showing how we obtain our computational domain.

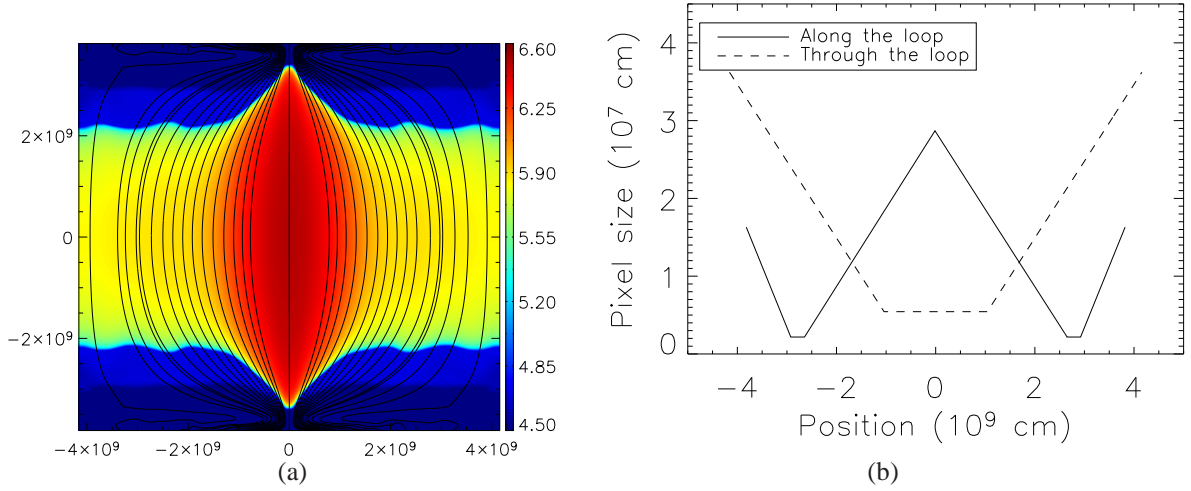


Figure 3.3 Figure (a): Plot of Temperature in logarithmic scale of our loop model. The Blue domain is the chromospheric part of the domain at the basis of the loop. The black lines are the magnetic field lines. Temperature spans from  $2 \times 10^4$  K to  $3 \times 10^6$  K. Figure (b): Pixels size on computational domain. Solid line is the pixels size (dy) along the loop direction (y coordinate). Dashed line is the pixels size (dx) across the loop (x coordinate). The resolution spans from  $2 \times 10^6$  cm to  $4 \times 10^7$  cm.

Eq. 1.9, and we are also interested in having a magnetic field intensity of at least 10 G in corona (sufficient to confine coronal loop plasma).

We create such a configuration with a preliminary simulation. We start from a simple configuration with a totally parallel magnetic field. The magnetic field is more intense in the center of the domain. Then we let this configuration relax to the equilibrium configuration. Since the corona is much more tenuous than the chromosphere (and pressure lower), the magnetic field will expand much more in the corona. We will end up with a relatively uniform magnetic field across the domain, but strongly expanding from the chromosphere to the corona.

In Fig. 3.4 and 3.5 I show the starting loop configuration. Fig. 3.4a shows a map of temperature in logarithmic scale for our loop initial condition, and Fig. 3.5a shows the corresponding temperature profile along the loop (along y direction, for all x position). Temperature spans from  $2 \times 10^4$  K in chromosphere to  $8 \times 10^5$  K in corona.

Fig. 3.4b shows a map of electron density in logarithmic scale for the same system, and Fig. 3.5b shows the corresponding electron density profile along the loop (along y direction, for all x position). Electron density spans from  $10^8$  cm<sup>3</sup> in corona to  $1 \times 10^{14}$  K in chromosphere.

To build our initial condition we use the temperature and density profile of a static loop with an apex temperature about  $8 \times 10^5$  K. For the chromospheric part of the loop we use a hydrostatic atmosphere with a uniform temperature (i.e  $2 \times 10^4$  K).

Fig. 3.4c shows a map of the module of magnetic field in our spatial domain. The magnetic field intensity varies from 1 G to 61 G along  $x$ , and it is given by the equation:

$$\begin{cases} B_x = 0 \\ B_y = \frac{B_0}{\left(\frac{x-x_0}{\sigma_l}\right)^2 + 1} + B_1 \end{cases} \quad (3.12)$$

where we set  $B_0 = 60$  G,  $B_1 = 1$  G,  $x_0 = 0$  cm, and  $\sigma_l = 4 \times 10^8$  cm, as we can see from Fig. 3.5c.

We set periodic boundary condition for both the axes.

Fig. 3.4d is the map of plasma  $\beta$  factor. We can easily see that  $\beta$  is  $\ll 1$  in the chromosphere and  $\gg 1$  in the corona. This means that in corona plasma motions are driven by the magnetic field, whereas in chromosphere the magnetic field lines are drawn by plasma motions.

We let the system evolve for  $10^4$  s, obtaining a relative stable loop atmosphere, with a strong expansion of the magnetic field lines near the transition region. This stable initial condition is shown in Fig 3.6

This simulation is performed using the CINECA/SP6 High Performance Computing facility and it has been used about  $4 \times 10^4$  hours of cpu time<sup>1</sup> to complete it. Furthermore, it has been used about  $8 \times 10^4$  hours of cpu time to prepare develop and debug the code. Many different initial conditions have been tested, finding that the resolution on transition region is a fundamental parameter of simulation. We also find that a too low resolution on transition region can explain some instability observed in some MHD simulation of coronal loops (e.g. Carlsson et al. 2010; Bingert & Peter 2011; Martínez-Sykora et al. 2011a,b).

### 3.2.2 The simulation

We use the results of the previous simulation as the starting point of a new simulation to test the response of plasma to the heating.

Our scope is to study what is the level of variability expected in the moss according to different heating models. The models are expected to compare with the evidence of moss steady on long time scales. Our starting point is to consider a large-scale slowly-changing (quasi-steady) heating (e.g.: Winebarger et al. 2011; Warren et al. 2010a,b). We might expect that a very gradual heating should drive very slow loop variations and therefore keep the cross-section in the transition region constant in time. For a sound check of this hypothesis, we consider the situation in which the loop is heated as smoothly as possible. So in our first simulation we consider a transient heating released with increasing intensity in the central region of the domain, until the apex temperature reaches 3 MK. The heating

---

<sup>1</sup>On a parallel computer, CPU time is the time necessary to run the program multiplied by the number of core used for the run itself.

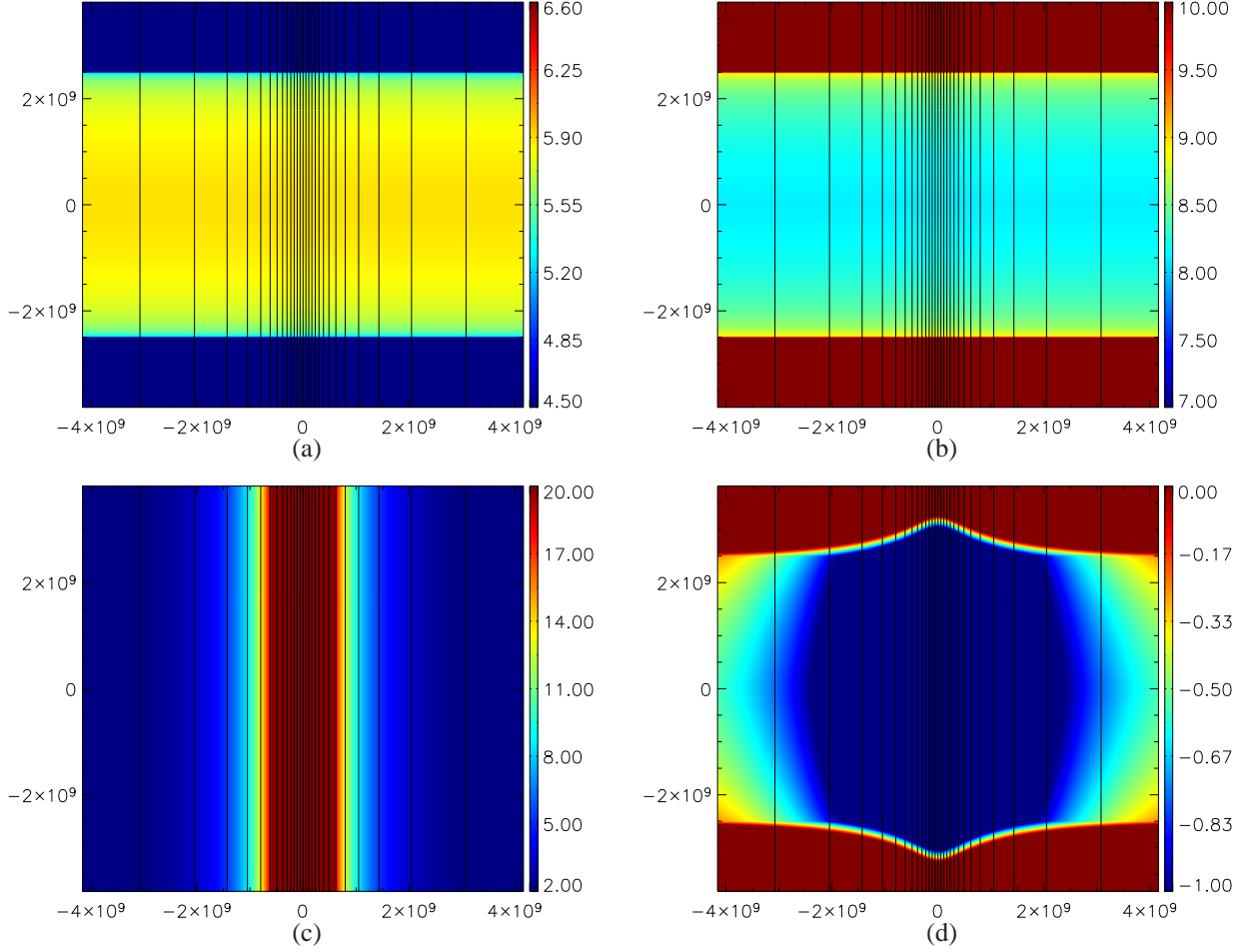


Figure 3.4 Figure (a): Plot of Temperature in logarithmic scale for our initial loop atmosphere. The Blue domain is the chromospherical part of the domain at the basis of the loop. Figure (b): Plot of electron density in logarithmic scale for the same atmosphere. Figure (c): Plot of the module of magnetic field for our initial loop atmosphere. . Figure (d): Plot of plasma  $\beta$  factor in logarithmic scale for our initial loop atmosphere. In all figures, the black lines are the magnetic field lines.

increases exponentially for a time much longer than the plasma reaction times, then it stays constant for an even longer time, and finally it decreases slowly to let the loop cool down smoothly.

We simulate 5000 s of loop evolution. We heat slowly all the central part of the loop until it reach an apex temperature about  $3 \times 10^6$  K. The heating function that we use is divided in two terms: the first is the static term  $H_s$  that cover uniformly the entire corona, whereas the second is a transient term  $H_t$  that change with time and cover only a part of the loop:

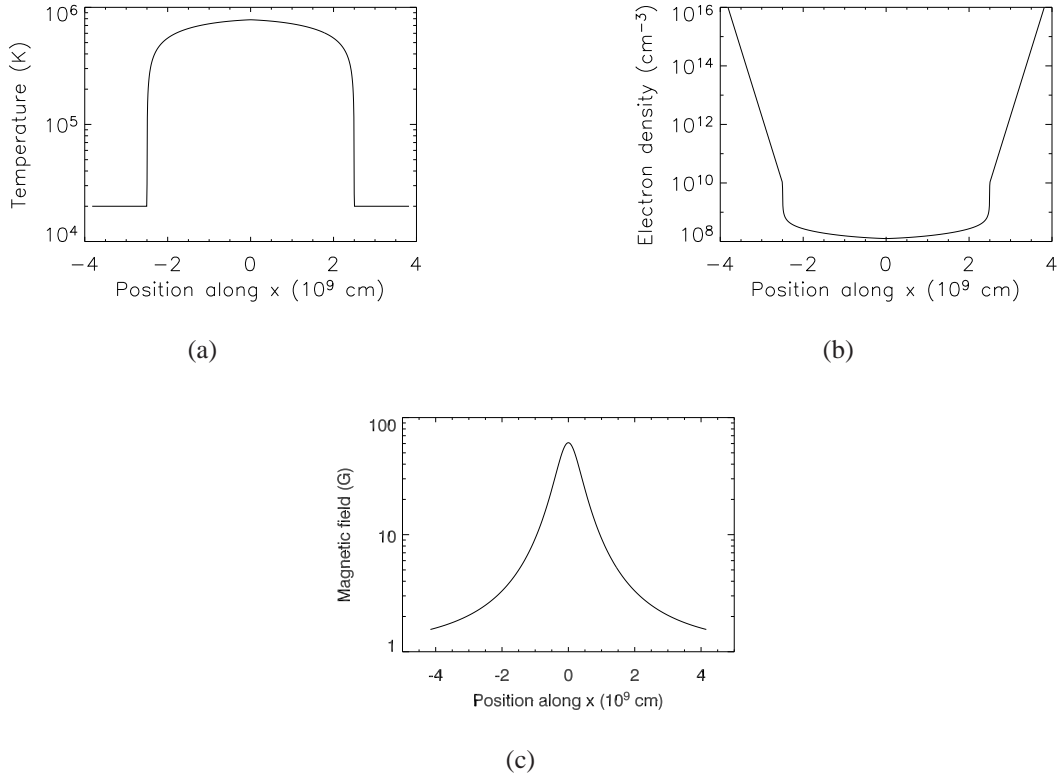


Figure 3.5 Temperature (Fig. (a)), electron density (Figure (b)), and magnetic field (Figure (c)) profile for our initial loop atmosphere. The density and temperature profiles are drawn along the loop, whereas the magnetic field profile is drawn across the loop.

$$\Lambda_T(x, t) = H_s + H_t(x, t) \quad (3.13)$$

According with the scale law (Rosner et al., 1978) the static term is set to  $H_s = 4.2 \times 10^{-5} \text{ erg cm}^{-3} \text{ s}^{-1}$ , sufficient to sustain a static loop with an apex temperature about  $8 \times 10^5 \text{ K}$ .

The second term varies with time and space as described by:

$$H_t(x, t) = H_s H(x) f(t) \quad (3.14)$$

where:

$$H(x) = e^{-x^2/2\sigma_H^2} \quad (3.15)$$

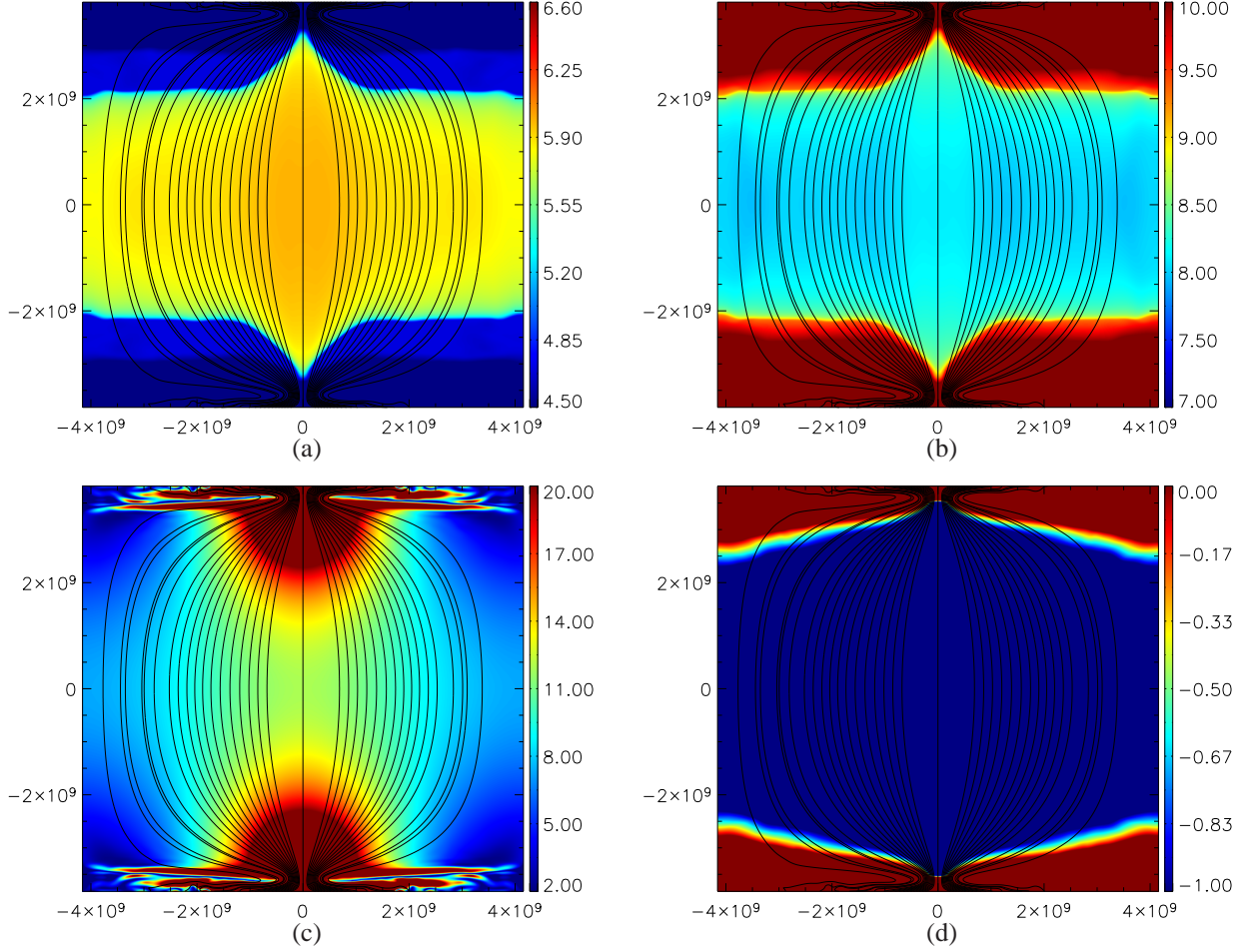


Figure 3.6 The same of Fig. 3.4 for the stable final atmosphere, obtained after  $10^4$  s of evolution from the initial condition reported in Fig. 3.4

$$f(t) = \begin{cases} 0 & t < t_0 \\ 10^{(t-t_0)/\tau} & t_0 \leq t < t_1 \\ H_0/H_s & t_1 \leq t < t_2 \\ 0 & t \geq t_2 \end{cases} \quad (3.16)$$

$t_0 = 0$  s,  $t_1 = 1000$  s,  $t_2 = 3000$  s, and  $\tau = (t_2 - t_1) / \text{Log}(H_0/H_s)$ . We chose to set  $H_0 = 2 \times 10^{-3} \text{ erg cm}^{-3} \text{ s}^{-1}$ , that according with the scale laws (Rosner et al., 1978) can sustain a loop with an apex temperature about  $3 \times 10^6$  K.

The time profile of the heating is reported in Fig. 3.7

This simulation is performed using the CINECA/SP6 High Performance Computing facility and it has been used about  $4 \times 10^4$  hours of cpu time to complete it.

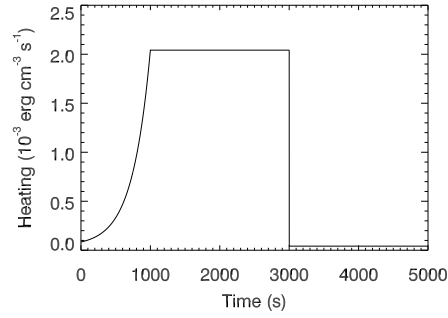


Figure 3.7 Time profile for the heating function calculated on  $x = 0$ .

### 3.2.3 Results

In this section I report the first results obtained from this simulation. We show results for the first part of the simulation (from  $t = 0 \text{ s}$  to  $t = 2.5 \times 10^3 \text{ s}$ ), where the heating rises up until the apex temperature reaches  $3 \times 10^6 \text{ K}$ .

Fig. 3.8 shows i.e. maps of temperature, density and  $\beta$  factor at progressive times. We see that the temperature gradually increases in the central region of the loop. Only the region along the magnetic field lines is heated. The density increases gradually as well as we expected from the very slow growth rate of the heating. The plasma dynamics is minor at any time. No local features are visible and also the  $\beta$  evolves slowly, as expected. Overall, we have a very smooth and “steady” evolution as we expected.

Our attention now turns more specifically to the transition region, and in particular to the loop cross-section in the expansion region. For quantitative analysis, we consider two magnetic field lines on the sides of the heated part of the loop. These lines are symmetric and are far from the central axis of the loop  $8 \times 10^8 \text{ cm}$  at the loop apex, as shown in Fig. 3.9a and b.

To study the evolution of the loop layers that compose the moss, I analyze the height and width of the layer between the selected field lines at a temperature of  $2 \times 10^5 \text{ K}$ . Fig. 3.9c,d shows the width and height of the layer vs time. As our preliminary simulation shows, this layer becomes progressively narrower as the heating increases, essentially because, due to the progressive evaporation, the transition region drifts deeper inside the chromosphere, in regions where  $\beta$  gets smaller. This variation is stronger when the heating increases (from  $t = 0$  to  $1000 \text{ s}$ ), but continues also when the heating is constant. We expect that the variation of the area is a tracer of a variation of the brightness. Therefore, this result could indicate that slow variations of heating lead to considerable variations of the moss appearance. The preliminary conclusion is that a quasi-static heating does not seem in good agreement with the steady appearance of the moss. However, more investigations are needed to constrain this result better.



### 3.3 Discussion

We investigate an MHD model of coronal loop, taking into account the presence of a strong variation of the loop cross-section of the moss region.

Our model considers the time-dependent MHD equations in a 2D Cartesian coordinate system including the gravitational force (for a curved loop), the thermal conduction (including the effects of heat flux saturation), the coronal heating (via a phenomenological term), and radiative losses from optically thin plasma.

We first create the proper loop topology ready for the injection of heating. Then, as first test of our model, we heat our loop with a large-scale slowly-changing (quasi-steady) heating (e.g.: Winebarger et al. 2011; Warren et al. 2010a,b), and we search for the position and size of the moss region.

From Fig. 3.9c and d we have seen that position and size of moss region change with time. Consequently also the emission from moss vary.

The next step of our research activity will be to derive the emission measure distribution from moss, and then derive the corresponding emission in some important spectral bands and lines, then we will compare these curve of light with the observation from HINODE and SDO filters. We will also consider different heating mechanism, such as for example nanoflare heating. Finally, we plan to obtain some constrain on the real heating mechanism through the comparison of the synthesized curve of light with the observed ones.

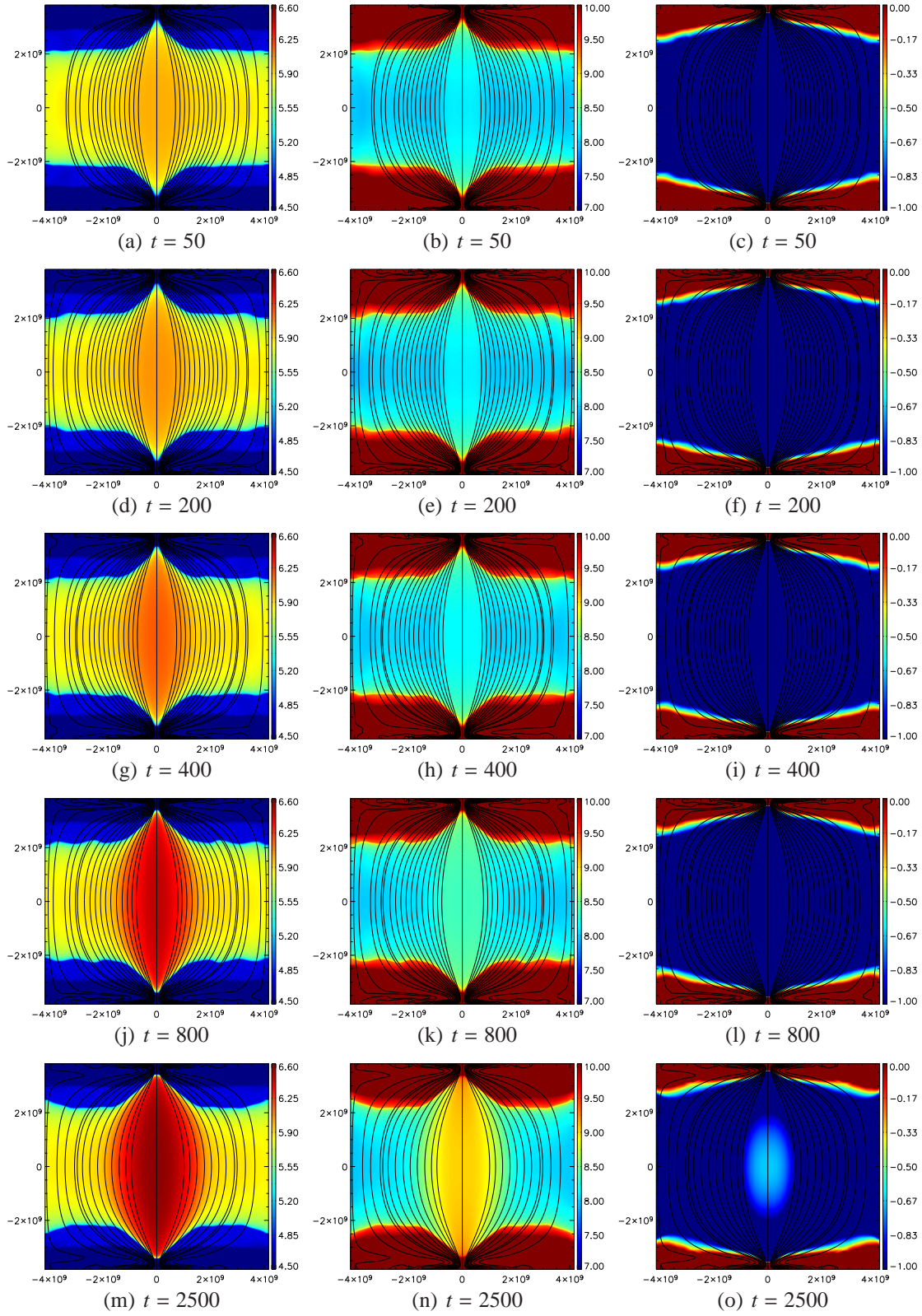


Figure 3.8 Temperature (left column), electron density (central column), and plasma  $\beta$  factor (right column) profile for our loop at  $t = 50$  s (panel a, b and c),  $t = 200$  s (panel d, e and f),  $t = 400$  s (panel g, h and i),  $t = 800$  s (panel j, k and l),  $t = 2500$  s (panel m, n and o).

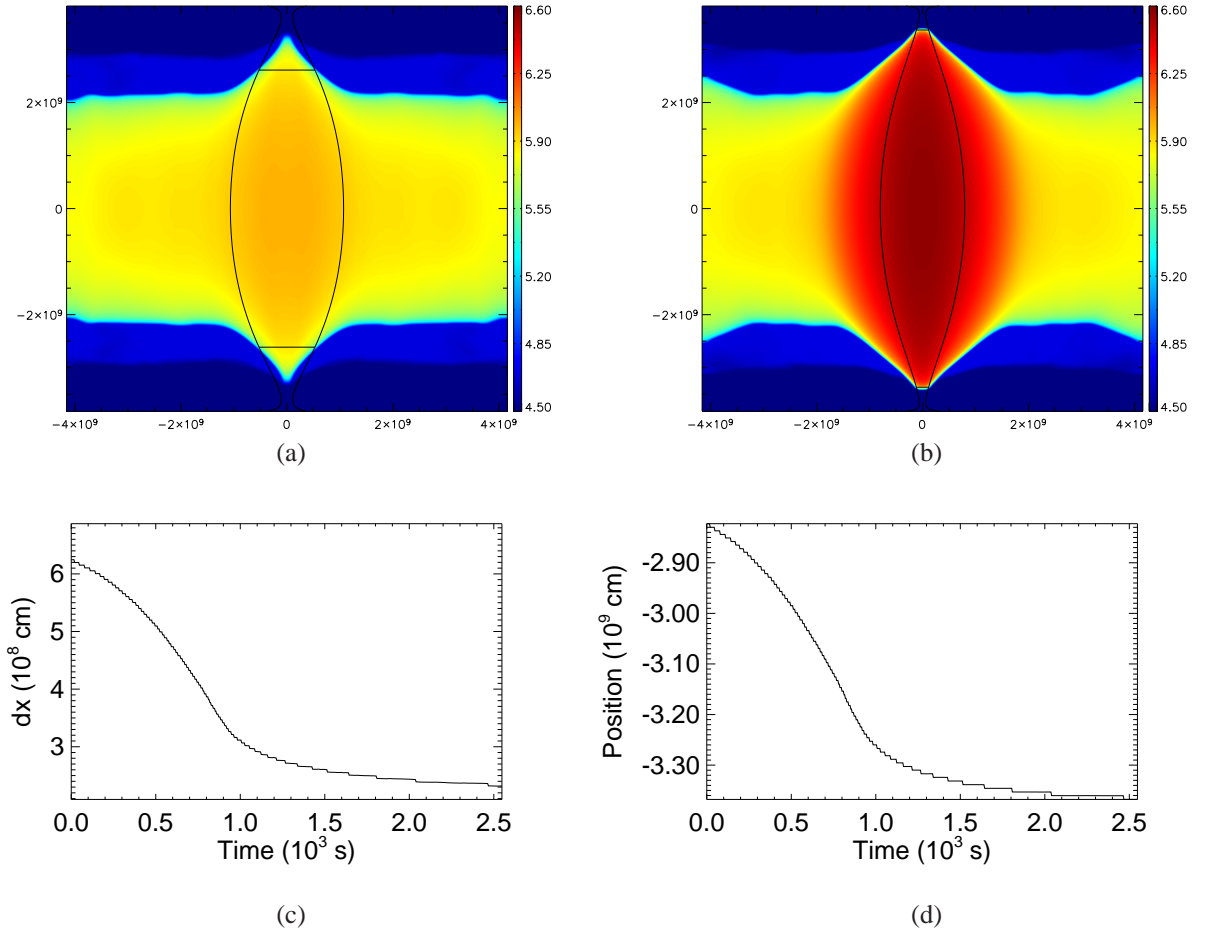


Figure 3.9 Evolution of the moss region. In panel (a) and (b) we see the map of temperature in logarithmic scale at  $t = 0$  s and  $t = 2500$  s. The vertical lines are the field lines that we use to identify the loop. The horizontal lines identify the moss position. Panel (c) is the evolution of the moss size with time. Panel (d) is the position of the moss with time.

## **Chapter 4**

# **Conclusions and Future Developments**

This thesis is devoted to modeling the fine and dynamic structure of coronal magnetic loops.

The first part investigates loops as multi-strand systems, each strand being heated once by a short and intense pulse. To this purpose we describe the loop as a collection of independent thin tubes and use for each tube a standard 1-D loop model. In Chap. 2 we investigated whether multi-strand loops can explain the evidence of increasing fuzziness of coronal regions at increasing temperatures. Our basic scenario is that coronal loops consist of bundles of thin strands, each of thickness below the instrumental spatial resolution, and that each strand is heated up to about 10 MK by a strong and fast heat pulse. We treat each strand as strictly independent of the others and we describe the loops as collections of identical strands. We also use standard loop hydrodynamic modeling to model a single pulse-heated strand. We replicate and shuffle the model strand until a proper loop system is built, and we compare the emission predicted after this procedure with observations.

The images synthesized from our model show the same “fuzziness” in the same warm lines as observed with EIS, and the same better definition in the cooler lines as observed with EIS. In other words, our model is able to explain the evidence.

The reason is that the strands spend a long time with a high emission measure at a temperature around 3 MK, much less time when plasma is hotter, and long time, but with much less emission measure, when the plasma is cooler. So the loop systems appear more uniform around 3 MK, and this higher filling factor gives the impression of “fuzziness”, as described in Tripathi et al. (2009).

Our analysis provides also an interesting prediction: we expect high contrast to show up in very hot lines, such as the Fe XXIII line and the Ca XIX line (typical flare lines), even stronger than in the cool lines.

We have been able to verify this prediction on a recent observation with the Solar Dynamics Observatory. In particular we have ascertained that the active region core appears more fuzzy in the 335 Å channel ( $T \sim 3$  MK) than in the 94 Å channel ( $T \sim 6 - 8$  MK). This largely confirms the prediction of our model, i.e. that there is widespread extensive hot plasma in active regions, and that hot active region plasma is very finely structured, as expected in our scenario where storms of nanoflares are heating the coronal loops, one for each strand. The reason why these superhot components are so difficult to detect is their small emission measure, and their small duty cycle with respect to most of their evolution time, spent mostly for the subsequent long cooling phase. Desirable future X-ray spectral observations of the quiet Sun, and in particular of active regions, at high sensitivity and enough spatial resolution, may provide further confirmation of our scenario.

In the second part (Chap. 3) I deal with a new more general loop model, including the interaction of the plasma with the ambient magnetic field. So this is a full MHD multi-D loop model. We need this model to address very detailed questions on the structure of loops that cannot be treated with 1-D models.

In particular, we focus on the structure of the so-called moss in active regions detected at temperatures about 1 MK, that are generally interpreted as the footpoints of hotter loops. To study the low-lying parts of the loops in high detail, the assumption of constant cross-section all along the loop cannot hold, because it is known that the loop greatly expands going up from the transition region to the corona (e.g. (Gabriel, 1976)). We cannot help including this effect in the modeling, and how it changes in time and with the plasma  $\beta$ , and this requires a proper time-dependent magnetohydrodynamic description. Therefore, we use 2D-MHD model considering also gravity, the thermal conduction (including the effects of heat flux saturation), the coronal heating (via a phenomenological term), and radiative losses from optically thin plasma, to study the response of plasma to a quasi-steady heating.

Our first simulations show that the position and the size of the moss region vary with time, as the emission of moss itself. As next step we will analyze the light curve from moss region and we compare it with observational evidences from HINODE and SDO mission.

We also plan to repeat the same simulation changing first only the total energy release, and then changing the heating mechanism, using a nanoflare-like phenomenological heating function. We will use these new simulations to analyze the temporal variability obtained from the models with the instrumental curves of light, to obtain some constraints on the heating mechanism of coronal loops, such as for example the cadence, and the spatial and energy distribution.



# Acknowledgements

I acknowledge support from Italian *Ministero dell'Università e Ricerca* and *Agenzia Spaziale Italiana (ASI)*, contract I/023/09/0 and I/015/07/0. PLUTO is developed at the Turin Astronomical Observatory in collaboration with the Department of General Physics of the Turin University. All computations were performed on the IBM/Sp6 supercomputer at CINECA (Bologna, Italy; CINECA Class B project: “Modeling of Heating of Coronal Loops”; CINECA Class C project: “Nanoflare heating of Multi-Stranded Coronal Loops”; INAF-CINECA project: “MHD Modeling of Multi-stranded Coronal Loops Heated by Nanoflares”), and at the HPC facility (SCAN) of the INAF - Osservatorio Astronomico di Palermo.

*CHIANTI* is a collaborative project involving the *NRL (USA)*, the *Universities of Florence (Italy)* and *Cambridge (UK)*, and *George Mason University (USA)*.

I am heartily thankful to my supervisor, Fabio Reale, whose encouragement, guidance and support enabled me to complete my PhD.

This thesis would not have been possible without the help of Salvatore Orlando, and I am very grateful to him for this.

I owe my gratitude to Andrea Mignone and Petros Tzeferacos, for their suggestion about PLUTO code.

I would like to show my gratitude to Giovanni Peres and James Klimchuk for their useful suggestions in my research activity, and Giuseppe Compagno for his careful reading of this thesis and his suggestions.

I am indebted to my colleagues and friends that supported me, and in particular it's a pleasure for me to thank , Marilena Caramazza, Mario Guarcello, Marco Miceli, Rosaria Bonito, Costanza Argiroffi, Chiara Gelardi, Emanuele Di Gloria, and specially my friend Sergio Terzo.

I would like to show my gratitude to my parents, to my brother and to my girlfriend Sonia, because they have made available their support in a large number of ways.

Lastly, I offer my regards and blessings to all of those who supported me in any respect during the completion of my PhD.



**NOTE:** Part of the work here presented has been published in refereed journals and presented at international conferences. Chapter 2 has been published as Guarrasi et al. (2010) on *The Astrophysical Journal* and Reale et al. (2011) on *The Astrophysical Journal Letters*. The analysis of Chapter 3 is the subject of an article in preparation.

# Bibliography

- Anders, E. & Grevesse, N. 1989, *Geochim. Cosmochim. Acta*, 53, 197
- Antiochos, S. K., MacNeice, P. J., Spicer, D. S., & Klimchuk, J. A. 1999, *ApJ*, 512, 985
- Aschwanden, M. J. & Boerner, P. 2011, *ApJ*
- Aschwanden, M. J., Nightingale, R. W., & Alexander, D. 2000, *ApJ*, 541, 1059
- Balbus, S. A. 1986, *ApJ*, 304, 787
- Balsara, D. S. & Spicer, D. S. 1999, *Journal of Computational Physics*, 149, 270
- Betta, R., Peres, G., Reale, F., & Serio, S. 1997, *A&A*, 122, 585
- Betta, R. M., Peres, G., Reale, F., & Serio, S. 2001, *A&A*, 380, 341
- Bingert, S. & Peter, H. 2011, *A&A*, 530, A112
- Bradshaw, S. J. & Cargill, P. J. 2006, *A&A*, 458, 987
- Bradshaw, S. J. & Mason, H. E. 2003, *A&A*, 407, 1127
- Brickhouse, N. S. & Schmelz, J. T. 2006, *ApJ*, 636, L53
- Cargill, P. J. 1994a, *The Astrophysical Journal*, 422, 381
- . 1994b, *ApJ*, 422, 381
- Cargill, P. J. & Klimchuk, J. A. 1997, *ApJ*, 478, 799
- . 2004, *The Astrophysical Journal*, 605, 911
- Carlsson, M., Hansteen, V. H., & Gudiksen, B. V. 2010, *Mem. Soc. Astron. Italiana*, 81, 582
- Culhane, J. L. 2007, in *Astronomical Society of the Pacific Conference Series*, Vol. 369, *New Solar Physics with Solar-B Mission*, ed. K. Shibata, S. Nagata, & T. Sakurai, 3–+

- De Pontieu, B., McIntosh, S. W., Carlsson, M., Hansteen, V. H., Tarbell, T. D., Boerner, P., Martinez-Sykora, J., Schrijver, C. J., & Title, A. M. 2011, *Science*, 331, 55
- Dere, K. P., Landi, E., Mason, H. E., Monsignori Fossi, B. C., & Young, P. R. 1997, *A&AS*, 125, 149
- Di Matteo, V., Reale, F., Peres, G., & Golub, L. 1999, *A&A*, 342, 563
- Doschek, G. A., Boris, J. P., Cheng, C. C., Mariska, J. T., & Oran, E. S. 1982, *ApJ*, 258, 373
- Feldman, U. 1992, *Phys. Scr*, 46, 202
- Fisher, G. H., Canfield, R. C., & McClymont, A. N. 1985, *ApJ*, 289, 414
- Fletcher, L. & de Pontieu, B. 1999, *The Astrophysical Journal Letters*, 520, L135
- Gabriel, A. H. 1976, *Royal Society of London Philosophical Transactions Series A*, 281, 339
- Gan, W. Q., Zhang, H. Q., & Fang, C. 1991, *A&A*, 241, 618
- Golub, L. & Pasachoff, J. M. 1997, *The Solar Corona* (The Solar Corona, by Leon Golub and Jay M. Pasachoff, pp. 388. ISBN 0521480825. Cambridge, UK: Cambridge University Press, September 1997.)
- Gomez, D. O., Martens, P. C. H., & Golub, L. 1993a, *ApJ*, 405, 767
- . 1993b, *ApJ*, 405, 773
- Guarrasi, M., Reale, F., & Peres, G. 2010, *ApJ*, 719, 576
- Handy, B. N., Acton, L. W., Kankelborg, C. C., Wolfson, C. J., Akin, D. J., Bruner, M. E., Carvalho, R., Catura, R. C., Chevalier, R., Duncan, D. W., Edwards, C. G., Feinstein, C. N., Freeland, S. L., Friedlaender, F. M., Hoffmann, C. H., Hurlburt, N. E., Jurcevich, B. K., Katz, N. L., Kelly, G. A., Lemen, J. R., Levay, M., Lindgren, R. W., Mathur, D. P., Meyer, S. B., Morrison, S. J., Morrison, M. D., Nightingale, R. W., Pope, T. P., Rehse, R. A., Schrijver, C. J., Shine, R. A., Shing, L., Strong, K. T., Tarbell, T. D., Title, A. M., Torgerson, D. D., Golub, L., Bookbinder, J. A., Caldwell, D., Cheimets, P. N., Davis, W. N., Deluca, E. E., McMullen, R. A., Warren, H. P., Amato, D., Fisher, R., Maldonado, H., & Parkinson, C. 1999, *Sol. Phys.*, 187, 229
- Hansteen, V. 1993, *ApJ*, 402, 741
- Hollweg, J. V. 1984, *ApJ*, 277, 392

- Klimchuk, J. A. 2006, *Sol. Phys.*, 234, 41
- Kosugi, T., Matsuzaki, K., Sakao, T., Shimizu, T., Sone, Y., Tachikawa, S., Hashimoto, T., Minesugi, K., Ohnishi, A., Yamada, T., Tsuneta, S., Hara, H., Ichimoto, K., Suematsu, Y., Shimojo, M., Watanabe, T., Shimada, S., Davis, J. M., Hill, L. D., Owens, J. K., Title, A. M., Culhane, J. L., Harra, L. K., Doschek, G. A., & Golub, L. 2007, *Sol. Phys.*, 243, 3
- Lenz, D. D., Deluca, E. E., Golub, L., Rosner, R., Bookbinder, J. A., Litwin, C., Reale, F., & Peres, G. 1999, *Sol. Phys.*, 190, 131
- MacNeice, P. 1986, *Sol. Phys.*, 103, 47
- Martens, P. C. H., Kankelborg, C. C., & Berger, T. E. 2000, *The Astrophysical Journal*, 537, 471
- Martens, P. C. H., van den Oord, G. H. J., & Hoyng, P. 1985, *Sol. Phys.*, 96, 253
- Martínez-Sykora, J., De Pontieu, B., Testa, P., & Hansteen, V. 2011a, *ApJ*, 743, 23
- Martínez-Sykora, J., Hansteen, V., & Moreno-Insertis, F. 2011b, *ApJ*, 736, 9
- Mazzotta, P., Mazzitelli, G., Colafrancesco, S., & Vittorio, N. 1998, *A&AS*, 133, 403
- McTiernan, J. M. 2009, *The Astrophysical Journal*, 697, 94
- Mignone, A., Bodo, G., Massaglia, S., Matsakos, T., Tesileanu, O., Zanni, C., & Ferrari, A. 2007, *ApJS*, 170, 228
- Mignone, A., Zanni, C., Tzeferacos, P., van Straalen, B., Colella, P., & Bodo, G. 2011, *ArXiv e-prints*
- Müller, D. A. N., Hansteen, V. H., & Peter, H. 2003, *A&A*, 411, 605
- Nagai, F. 1980, *Sol. Phys.*, 68, 351
- Nagai, F. & Emslie, A. G. 1984, *ApJ*, 279, 896
- Nakariakov, V. M., Ofman, L., Deluca, E. E., Roberts, B., & Davila, J. M. 1999, *Science*, 285, 862
- O'Dwyer, B., Del Zanna, G., Mason, H. E., Weber, M. A., & Tripathi, D. 2010, *A&A*, 521, A21+
- Ofman, L. & Wang, T. J. 2008, *A&A*, 482, L9
- Orlando, S., Bocchino, F., Reale, F., Peres, G., & Pagano, P. 2008, *ApJ*, 678, 274

- Orlando, S., Peres, G., Reale, F., Bocchino, F., Rosner, R., Plewa, T., & Siegel, A. 2005, *A&A*, 444, 505
- Parker, E. N. 1983, *ApJ*, 264, 635
- . 1988, *ApJ*, 330, 474
- Patsourakos, S. & Klimchuk, J. A. 2005, *ApJ*, 628, 1023
- Patsourakos, S. & Klimchuk, J. A. 2007, in *Second Solar Orbiter Workshop*, ed. E. Marsch, K. Tsinganos, R. Marsden, L. Conroy (Noordwijk: ESA), ESA Special Publication
- . 2008, *ApJ*, 689, 1406
- Peres, G., Orlando, S., Reale, F., Rosner, R., & Hudson, H. 2000, *ApJ*, 528, 537
- Peres, G., Reale, F., & Golub, L. 1994, *The Astrophysical Journal*, 422, 412
- Peres, G., Reale, F., & Serio, S. 1993, in *Physics of Solar and Stellar Coronae: G. S. Vaiana Memorial Symposium*, held 22-26 June, 1992, in Palermo, Italy. Edited by Jeffrey L. Linsky and Salvatore Serio. *Astrophysics and Space Science Library*, Vol. 183. Published by Kluwer Academic Publishers, P. O. Box 17, 3300 AA Dordrecht, The Netherlands, 1993., p.151, ed. J. L. Linsky & S. Serio, 151—
- Peres, G., Reale, F., Serio, S., & Pallavicini, R. 1987, *ApJ*, 312, 895
- Peres, G., Serio, S., Vaiana, G. S., & Rosner, R. 1982, *ApJ*, 252, 791
- Priest, E. R. 1978, *Sol. Phys.*, 58, 57
- . 1987, *Solar magneto-hydrodynamics*. (*Solar magneto-hydrodynamics* by E.R. Priest. Dordrecht: D. Reidel, 1987.)
- Raymond, J. C., Cox, D. P., & Smith, B. W. 1976, *ApJ*, 204, 290
- Raymond, J. C. & Smith, B. W. 1977, *ApJS*, 35, 419
- Reale. 2007, *A&A*, 471, 271
- Reale, F. 2010, *Living Reviews in Solar Physics*, 7, 5
- Reale, F., Guarrasi, M., Testa, P., DeLuca, E. E., Peres, G., & Golub, L. 2011, *ApJ*, 736, L16+
- Reale, F., McTiernan, J. M., & Testa, P. 2009a, *The Astrophysical Journal Letters*, 704, L58

- Reale, F. & Orlando, S. 2008, *ApJ*, 684, 715
- Reale, F., Parenti, S., Reeves, K. K., Weber, M., Bobra, M. G., Barbera, M., Kano, R., Narukage, N., Shimojo, M., Sakao, T., Peres, G., & Golub, L. 2007, *Science*, 318, 1582
- Reale, F. & Peres, G. 1995, *A&A*, 299, 225
- . 2000, *ApJ*, 528, L45
- Reale, F., Peres, G., Serio, S., Betta, R. M., DeLuca, E. E., & Golub, L. 2000, *ApJ*, 535, 423
- Reale, F., Testa, P., Klimchuk, J. A., & Parenti, S. 2009b, *The Astrophysical Journal*, 698, 756
- Rosner, R., Tucker, W. H., & Vaiana, G. S. 1978, *ApJ*, 220, 643
- Sakamoto, Y., Tsuneta, S., & Vekstein, G. 2009, *ApJ*, 703, 2118
- Schmelz, J. T., Kashyap, V. L., Saar, S. H., Dennis, B. R., Grigis, P. C., Lin, L., De Luca, E. E., Holman, G. D., Golub, L., & Weber, M. A. 2009, *The Astrophysical Journal*, 704, 863
- Spitzer, L. 1965, *Physics of fully ionized gases* (Interscience Tracts on Physics and Astronomy, New York: Interscience Publication, 1965, 2nd rev. ed.)
- Sylwester, B., Sylwester, J., & Phillips, K. J. H. 2010, *Astronomy & Astrophysics*, 514, A82+
- Testa, P., Peres, G., & Reale, F. 2005, *ApJ*, 622, 695
- Tripathi, D., Mason, H. E., Dwivedi, B. N., del Zanna, G., & Young, P. R. 2009, *ApJ*, 694, 1256
- Vekstein, G. 2009, *A&A*, 499, L5
- Vernazza, J. E., Avrett, E. H., & Loeser, R. 1981, *ApJS*, 45, 635
- Warren, H. P., Kim, D. M., DeGiorgi, A. M., & Ugarte-Urra, I. 2010a, *ApJ*, 713, 1095
- Warren, H. P. & Winebarger, A. R. 2006, *ApJ*, 645, 711
- . 2007, *ApJ*, 666, 1245
- Warren, H. P., Winebarger, A. R., & Brooks, D. H. 2010b, *ApJ*, 711, 228
- Warren, H. P., Winebarger, A. R., & Hamilton, P. S. 2002, *ApJ*, 579, L41

Warren, H. P., Winebarger, A. R., & Mariska, J. T. 2003, ApJ, 593, 1174

Winebarger, A. R., Schmelz, J. T., Warren, H. P., Saar, S. H., & Kashyap, V. L. 2011, ApJ, 740, 2

Winebarger, A. R., Warren, H. P., & Mariska, J. T. 2003a, ApJ, 587, 439

Winebarger, A. R., Warren, H. P., & Seaton, D. B. 2003b, ApJ, 593, 1164

Young, P. R., Del Zanna, G., Landi, E., Dere, K. P., Mason, H. E., & Landini, M. 2003, ApJS, 144, 135